



Scuola Internazionale Superiore di Studi Avanzati - Trieste

SISSA, INTERNATIONAL SCHOOL FOR ADVANCED STUDIES

PHD COURSE IN STATISTICAL PHYSICS

ACADEMIC YEAR 2012/2013

**Numerical methods for quantum
systems with
 ∞ -dimensional space of states:
two examples, two approaches.**

THESIS SUBMITTED FOR THE DEGREE OF

Doctor Philosophiae

October 30th, 2013

Advisors:

G. Mussardo

R. Konik

M. Müller

Candidate:

Marco Beria

SISSA - Via Bonomea 265 - 34136 TRIESTE - ITALY



SISSA, INTERNATIONAL SCHOOL FOR ADVANCED STUDIES

PHD COURSE IN STATISTICAL PHYSICS

ACADEMIC YEAR 2012/2013

**Numerical methods for quantum
systems with
 ∞ -dimensional space of states:
two examples, two approaches.**

THESIS SUBMITTED FOR THE DEGREE OF

Doctor Philosophiae

October 30th, 2013

Advisors:

G. Mussardo

R. Konik

M. Müller

Candidate:

Marco Beria

To my grandfather.

Abstract. *In this thesis two rather different topics are addressed:*

- *the application of the Truncated Conformal Spectrum Approach (TCSA) to perturbations of $SU(2)_k$ Wess-Zumino-Witten (WZW) models, and to Landau-Ginzburg (LG) theories;*
- *the analysis of the role of quantum statistics in the steady flow patterns of 2d driven ideal Fermi gases in a non-integrable geometry.*

A common methodological question unifies the two topics: how to simulate numerically quantum systems with infinite spaces of states. This problem is typically faced either introducing a lattice in the real space or directly in the continuum, and the two addressed topics can be seen as examples of these two cases. The TCSA is aimed to tackle perturbed conformal field theories directly in the continuum. Instead, to study the ideal Fermi gas we introduce a lattice which naturally captures the features of the chosen non-integrable geometry.

Chapter 1: This part of the thesis is mainly methodological and it is focused on the application of the TCSA to $c = 1$ conformal field theories. In particular, our interest is concerned with perturbations of WZW models with $SU(2)_k$ symmetry, which capture low energy properties of $k/2$ -Heisenberg spin-chains. The new problem faced is how to apply the method in the presence of marginal perturbations, where UV divergences result in non-universal contributions in the simulations. A generic framework to cure this pathology is proposed, and tested in the case of the current-current deformation of $SU(2)_1$. Among $c = 1$ theories, Landau-Ginzburg theories are of great interest, since their classical structure of the vacua captures the massive phases of deformation of minimal models. The most important methodological problem we faced here is that LG theories have an uncountable space of states. We show that the TCSA applies also in this case, once the target space of the LG field is properly compactified. The TCSA is thus used to verify an existing conjecture on the number of stable neutral bound states.

Chapter 2: Interacting quantum gases, such as the electron liquid, are known to admit a hydrodynamic description and, as for classical interacting fluids, they develop turbulence at sufficiently strong driving. On the other hand, ideal classical fluids cannot develop any turbulent flow. We ask whether this property extends to ideal quantum gases. Indeed, Fermi gases satisfy the exclusion principle that could play the role of an effective interaction, resulting in non-trivial flows. We are going to describe an ideal Fermi gas which flows from a narrow channel into a wider region. A lattice which approximates the geometry is introduced, and the system is tackled within two approaches: the micro-canonical formalism and the Lindblad equation. In the first case the system is closed, while in the second one it is coupled to external baths. Despite this difference, the observed physics

turns out to be the same far from the boundaries. We show that, in specific regimes, quantum statistics induces non-trivial patterns in the vorticity, which generates local magnetic moments of a measurable intensity.

Contents

1	Truncated Conformal Spectrum Approach and $c = 1$ Conformal Field Theories.	9
1.1	An introduction to Wess-Zumino-Witten models.	13
1.2	TCSA for $SU(2)_k$ WZW models	17
1.3	$SU(2)_1$ perturbed by the spin-1/2 field	22
1.4	$SU(2)_1$ perturbed by current-current interactions	26
1.4.1	Universal Term in Ground State Energy from the TCSA	27
1.4.2	NRG and Marginal Perturbations	41
1.5	$SU(2)_2$ perturbed by the spin-1 field	42
1.6	Discussions on TCSA and perturbed $SU(2)_k$	44
1.7	Landau-Ginzburg Theories and stable bound states.	46
1.8	TCSA for Landau-Ginzburg theories.	51
1.8.1	The (conformal) computational basis.	52
1.8.2	The perturbation: the Fourier method	53
1.8.3	Numerical Renormalization Group	57
1.9	Double well potential and stable neutral bound states.	58
1.9.1	LG theories and minimal models.	62
1.10	The Derivative-method.	65
1.11	Discussion on TCSA and Landau-Ginzburg theories.	67
2	Quantum-statistics induced flow patterns in driven ideal Fermi Gas.	69
2.1	The closed system: micro-canonical formalism.	73
2.2	Physical results.	77
2.3	The open system: Lindblad equation.	86
2.3.1	The physics of the open system.	90
2.3.2	The two-site system and the large Γ -behavior.	92
2.3.3	Flow patterns in the open system.	95
2.4	Conclusion and Discussion.	98
3	Conclusive Remarks	101

Appendices

A	Basics of TBA.	107
B	Compactified boson and sine-Gordon model.	111
C	The Derivative-method.	113
D	The commutator $[a_p, e^{i\gamma\phi}]$.	115
E	Influence of boundary conditions.	117
F	Magnetic and electric fields generated by charged polarized particles.	119
G	The Liouville-Fock Space.	121
H	Normal Master Modes and Shape Matrix.	123
I	The large- Γ expansion of the density matrix.	125

Guideline for the reader. This thesis is organized in two Chapters concerning rather different topics such that they could be considered almost unrelated, and the reader can choose to select one of the two main Chapters independently. The first Chapter is dedicated to the Truncated Conformal Spectrum Approach, a numerical method to study perturbed conformal field theories in the continuum. We applied the method to perturbed $SU(2)_k$ Wess-Zumino-Witten models, continuum limits of specific Heisenberg spin chains, and to Landau-Ginzburg theories. The second Chapter is dedicated to non-equilibrium ideal Fermi gases flowing in a non-integrable geometry. The main focus of this part is on the role of quantum statistics in the flow patterns detected in this kind of systems.

Despite the apparent differences, the two parts of the thesis are unified by the same methodological question: how to simulate numerically quantum systems with an infinite number of states. We are going to discuss in the Introduction this fundamental problem since many important physical systems are described by theories for which analytic approaches are difficult or hopeless, and numerical simulations are needed.

Introduction: numerical methods for large spaces of states.

Despite computer performance has exponentially improved in recent years, solving quantum systems numerically is still prohibitive without specific approximations. The principal reason is that their numerical solution typically requires to sample the space of states, which generally is very large or infinite. The problem concerns the huge demand of memory to store the space of states, as well as the long computational time needed to explore it.

Already for the simplest quantum mechanical systems, such as the free particle, the particle in a box, or the hydrogen atom, Hilbert spaces are infinite dimensional, and cannot be studied numerically unless some specific technique (or analytical insight) is used to reduce the set of states.

The problem becomes more intriguing in many-body systems, where analytic approaches are typically much more complicated, and numerical analyses are often required. As a trivial example, consider one of the simplest many-body system, built with spins in a given representation. Albeit each single spin is characterized by a finite – and usually small – Hilbert space, when joined together, they form a many-body system with a space of states which is exponentially large in the number of spins. These systems are known as spin-chains [1], and in the thermodynamic limit they capture the magnetic properties of some organic and inorganic crystals, KCuF_3 being an example [9]. For this reason, they are actively studied both analytically and numerically. However the huge number of states makes it problematic to study these models on traditional computers, where simulations are done on finite chains of rather small size¹.

Furthermore, a large variety of many-body quantum systems is modeled by *quantum field theories*. The (Fock-)space of states of these theories is naturally infinite, and, in some cases, even uncountable².

¹Consider that, on a standard laptop, a chain with ~ 15 spins is hardly processed, unless specific approximations or techniques are used.

²In the second part of the Chapter 1 we are going to address a specific example where the space of states is uncountable: the Landau-Ginzburg theories in $1 + 1$ dimensions.

Among these theories there are many important ones which describe fundamental aspects of nature such as phases of matter [2], fundamental interactions [3] and gravity [4]. All these examples can be very hard to tackle analytically, for instance when perturbation theory breaks down. Herein, numerical simulations are crucial, but not at all trivial, since the space of states must be reduced to a finite subspace, which should be large enough to capture the physical properties of interest, and, at the same time, sufficiently small to be tractable by a computer.

The difficulty of simulating quantum systems has been known for some times. Already in the 80s, Richard Feynman introduced the concept of *universal quantum simulator* [5] as a possible candidate to handle the huge number of quantum states³. In the same years, *quantum computers*⁴ were introduced, although not realized [6]. Hence, at the present time, the numerical investigation of quantum systems is still constrained to classical machines, and a finite, meaningful, and possibly small set of *computational states* must be identified to perform numerics efficiently.

Various successful (although still partial) solutions have been proposed in different fields. The common idea is to identify the relevant states that capture physical properties of interest, typically the low energy physics.

A successful method to study numerically many-body problems is the so called *Numerical Renormalization Group* (NRG) [12]. It was introduced by Kenneth Wilson in the 70s [13] to solve certain many-body systems with impurities, the first being the Kondo model. Although there have been several implementations of the NRG [12] – specific examples will be discussed in this thesis on Sections 1.4.2 and 1.8.3 – the common strategy is to realize numerically a renormalization transformation that iteratively reshapes the Hamiltonian into a new effective one where irrelevant degrees of freedom are described by effective terms. In this way, it is possible to reduce substantially the complexity of the problem, focusing just on the relevant features of the system.

With this idea in mind, along the years many improvements have been proposed. In

³The underlying idea is that a quantum system could be efficiently simulated only by a device which shares the same complexity, i.e. another quantum system. At the present time, a limited number of systems can be studied by the mean of quantum simulators [7], and, as an example, we cite ultra-cold trapped ions, which can be used to simulate certain metals very difficult to study even in laboratory [8].

⁴A quantum computer is a device which uses quantum properties to perform computations on data, in a more efficient way than in a classical computer. Using the fact that a quantum system can be in a superposition of states, the fundamental computational unit, the *q-bit*, can access much more configurations than the typical 0/1 of a classical bit. In light of this, more sophisticated information can be handled and eventually quantum systems can be simulated more efficiently. In this sense, quantum computers move in a similar conceptual direction than quantum simulators.

the context of spin chains, for instance, one of the most famous examples is the DMRG (*density matrix renormalization group*) [14]. This technique, proposed by Steven R. White in 1992 [15] as an improvement of Wilson's NRG, is aimed to describe a target state of a many-body system, typically the ground state, in an iterative variational way. The problem of the exponentially large space of states is (partially) overcome by identifying, iteration by iteration, the most relevant states to describe the target, selecting them by the (reduced) density matrix⁵. In this sense the DMRG implements an analogue of a renormalization group strategy⁶.

The DMRG procedure can be sped-up by the choice of a smart ansatz for the target state. One of the most successful variational ansatz in 1-dimensional many-body systems is to express the coefficients of the target state on a reference basis⁷ as a product of matrices⁸ (MPS) whose entries can be determined by energy optimization.

Beside these examples, all formulated in the discrete space, many systems are modeled by quantum field theories in the continuum. As anticipated, in this case the Fock-space is generally infinite and even uncountable in some cases. However, several tricks can reduce its cardinality.

For instance, it is well known that, if the available momenta for the particles are uncountable, it is enough to force constraints such as finite volume or periodic boundary conditions to select a discrete subset of allowed momenta. The physics of the original theory is then recovered by a finite-size scaling procedure [18], where the volume is increased to extrapolate the behavior at infinity. Typically the volume is also discretized on a lattice which implies a further reduction of the space of states⁹.

A famous example where some of these techniques have been used is that of *lattice gauge theories* [3], and – in particular – of quantum chromodynamics [19]. The space-time is discretized on a lattice and operators and fields are defined on nodes and links. In principle, the theory can be solved numerically by direct diagonalization. However, the numerical effort to accomplish this task is still remarkable and further techniques are used to speed-up the computation, the most significative being the quantum Monte Carlo [20].

Quantum Monte Carlo is a specific application of the Monte Carlo method to quantum systems [20]. The main idea underlying the Monte Carlo application to quantum field

⁵The procedure of selecting relevant states with the density matrix gives the name Density Matrix Renormalization Group to the method.

⁶However, it is important to underline that there are not ultraviolet nor infrared cut-offs, and no change in scale is performed.

⁷The computational basis is typically the spin-basis.

⁸It can be proven that the DMRG indeed produces MPSs [16].

⁹Notice that in the simple case of single particle problems the Hilbert space becomes finite dimensional.

theories is to compute observables by sampling the path-integral. Roughly, the observables are computed on sample field-configurations extracted with the probability measure defined by the action¹⁰. The average over the sampled realizations is then returned as the best approximation of the exact value of the observable. The method can reach, in principle, a high accuracy, since it can be improved by enlarging the sample over which the average is computed. However, the computational time is typically long, if high accuracies are needed.

Another interesting area where Monte Carlo like methods are used is lattice quantum gravity [4]. This numerical implementation of gravity is based on the simulation of the covariant path integral in a quantized (gravitational) background. The geometry is discretized on a simplicial structure which is indeed a multidimensional lattice approximation of the continuum curved space-time. This lattice fluctuates and its single realizations are generated with a probability fixed by the action.

As a matter of fact, all previous examples, sooner or later, require the introduction of some lattice structure. However, other methods that work directly on the continuum exist. The most representative and important for this thesis is the so called *Truncated Spectrum Approach* (TSA), which applies to quantum field theories with a countable number of states.

The method consists in the introduction of a proper truncation which selects just relevant states for the properties of interest, directly on the continuum, without introducing any lattice structure.

One of the branches where this method performed rather successfully is that of perturbed conformal field theories¹¹ in $1 + 1$ -dimensions [2]. Indeed, within these theories, the conformal basis is a natural candidate to be used as computational basis, once properly truncated to be finite dimensional, in a way that will be fully explained in the first Chapter. The specialization of the TSA to deformation of conformal field theories is called *Truncated Conformal Spectrum Approach* (TCSA).

Proposed for the first time in 1990 by Yurov and Zamolodchikov [21] the TCSA is a numerical method widely and successfully applied to both integrable and non-integrable perturbations of conformal field theories in $1 + 1$ dimensions [22, 2], whose low energy spectrum is determined with high accuracy.

If the number of states is uncountable, much more effort is needed to tackle the theory in the continuum, and the simplest strategy seems to introduce boundary conditions that

¹⁰For instance a sample of realizations can be generated by starting from an initial seed and proposing a random deformation. The new configuration is accepted with a probability which depends on the value of the action. Repeating the procedure produces samples which contain mainly configurations favored by the action. In principle, several further questions about ergodicity and convergence of the method can be posed, but addressing these issues is not the scope of this thesis. Further details can be found for instance in [20]

¹¹Defined on a cylinder.

limit the cardinality of the spectrum.

In alternative, other formulations, in which effective descriptions of the many-body system are considered can be attempted. An example, related to the second part of the thesis, is the *hydrodynamic approximation* [23]. Within this approach, the many-body system is described by effective quantities as spatial density and velocity (or eventually the current density), which obey equations of motion [25, 26, 27, 28, 29, 23] that assume a hydrodynamical form, such as the Navier-Stokes equations [24]. This global treatment of microscopic degrees of freedom into few effective fields exchanges the complexity of working with an infinite Fock-space into that of solving non-linear partial differential equations. Although, this task is not at all trivial¹², there are specific cases in which these can be solved with a reasonable numerical cost. The most interesting example for our purpose is the case of the electron liquid – the effective description of a many-electron system – flowing in non-integrable geometries [30, 108]. The physics emerging in the electron liquid will be strongly motivating for our investigations in Chapter 2.

All previous examples show that the problem of treating numerically the huge dimension of the space of states of a quantum system is an open and hard issue. We decided to tackle this problem within two examples of great interest for their wide applicability. The first one concerns numerical methods to study quantum field theories in the continuum, while the second one applies lattice approximations to study non-equilibrium Fermi gases flowing in non-integrable geometries.

In the Chapter 1 we are going to discuss and solve some technical issues about the application of the Truncated Conformal Spectrum Approach [21] to two classes of 1 + 1-dimensional models widely used in statistical physics: the *perturbed Wess-Zumino-Witten models* [33, 34] (WZW) and the *Landau-Ginzburg theories* [2].

The former models are of great interest since they capture the low energy properties of certain spin-chains [50]. These field theories can be decomposed in a conformal field theory – the WZW part – plus some perturbations, expressed in terms of operators of the conformal field theory itself. Hence, the Hamiltonian can be represented on the conformal basis, which is naturally infinite, but discrete, and states are organized into finite sets of given energy.

The introduction of an ultraviolet (UV) cutoff is in principle enough to obtain a finite dimensional space of states. We will discuss in detail the consequences of the introduction of this cutoff. In particular, we will focus on WZW models perturbed by marginal operators. In this case the cutoff results in non-universal contributions which must be properly treated to obtain universal results.

¹²The complicated dynamics of non-linear systems was originally observed by Enrico Fermi, Stanislaw Ulam, John Pasta, and Mary Tsingou already in the 1953 [31].

On the other hand, Landau-Ginzburg (LG) theories are bosonic field theories of fundamental interest in statistical physics since their classical structure of the vacua coincides with that of massive phases of several important models [35]. It is thus useful to study LG theories numerically in their natural continuum formulation.

The space of states in LG theories is uncountable, since the momentum of particles can take every (real) value. Hence, some further approximations beside the UV cutoff are needed in order to reduce to a finite dimensional space of states.

As anticipated, a typical technique is to impose periodic boundary conditions on the space. For what concerns the kinetic term of the Hamiltonian, this compactification leads to the theory of the *compactified boson*, which is conformal and has a discrete spectrum to which a UV cutoff can be applied. The original theory is obtained in the limit of a large compactification radius.

We will show which significant information about the low energy physics can be obtained within Landau-Ginzburg theories, with a reasonable computational cost.

After a detailed introduction on the topic, perturbed WZW models are treated from Sections 1.1 to 1.6, while Landau-Ginzburg theories are addressed from Section 1.7 to 1.11.

Chapter 2 is dedicated to ideal Fermi gases out of equilibrium. Interacting quantum gases, such as the electron liquid, are known to admit a hydrodynamic description and, similarly to classical interacting fluids, they develop an analogue of turbulence at sufficiently strong driving [29, 123, 30]. Ideal classical fluids instead cannot develop any turbulent flow [24], and we ask whether this property extends to ideal quantum gases. Indeed, Fermi gases satisfy the exclusion principle that could play the role of an effective interaction, resulting in non-trivial flows.

We are going to describe an ideal Fermi gas which flows from a narrow channel into a wider region. If the geometry is infinite in the longitudinal direction (both the narrow channel and the large very are infinitely long in the longitudinal direction but finite in the transverse one), the number of states is infinite, the available longitudinal momenta being even uncountable. Therefore the space of states has to be reduced to a finite sub-set for a numerical study.

The system is naturally described in the coordinate space and the most natural and established procedure is to define the system in a finite volume and discretize it on a lattice which captures the features of the geometry. Obviously the density of sites must be tuned properly in order to capture the physics at a given length-scale. For instance, we will look for specific features of Fermi statistics which naturally manifests itself at the scale of the Fermi wavelength. Although this condition constrains the density of sites to be much larger than the density of particles, the computational cost remains still affordable. Within the *micro-canonical* formalism, we will describe transport properties of a closed system where a local quench establishes a flow of particles and we will follow its dynamics. Beside the closed system, an open system, driven out of equilibrium by coupling to ex-

ternal baths, is studied. In this case, the transport properties can be captured by the Lindblad equation [36] which controls the time evolution of the density matrix and gives access to the non-equilibrium steady state (NESS).

To reduce the space of states to a finite set we will introduce again a lattice which captures the geometry. However, the solution of the Lindblad equation for the NESS-density matrix is, at this stage, exponentially complex in the number of sites.

A further improvement in performance will be achieved within the so called *third quantization formalism* [37, 38], which amounts to represent the Lindblad equation in a smart fermionic space, where symmetries of the ideal Fermi gas¹³ reduce the complexity to be linear in the number of sites. This is a significant optimization further reinforced by constructive prescriptions to determine easily existence and uniqueness of the NESS, and the values of observables in this state, if it is unique.

We introduce and contextualize the addressed problem in the beginning of the Chapter 2. The micro-canonical description of the closed system is discussed in Section 2.1, and the main physical result, obtained with the micro-canonical formalism, is presented in Section 2.2. The third quantization formulation of the Lindblad description is studied in Section 2.3, as well as the possible equivalence between the two descriptions of transport.

¹³The linearity of the coupling with external baths is also a fundamental ingredient within the third quantization formalism.

Chapter 1

Truncated Conformal Spectrum Approach and $c = 1$ Conformal Field Theories.

Based on arXiv:1301.0084.

Correlations in one dimensional systems typically require non-perturbative, non-mean field techniques to access the underlying physics. These techniques often trade on low energy, field theoretical reductions of the system. Examples include bosonization [39], conformal field theory [22], integrable field theory [2], the Bethe ansatz [40], and the truncated conformal spectrum approach (TCSA) [21]. The last approach, unlike the aforementioned techniques, is able to deal in principle with any one dimensional field theory, in an exact numerical manner. In that sense the TCSA is similar to the density matrix renormalization group (DMRG) [15], but the framework where it is formulated is field theoretical and not discrete quantum lattice systems.

TCSA deals with models whose Hamiltonians can be represented in the form,

$$H = H_{CFT} + \Psi, \tag{1.1}$$

where H_{CFT} is the Hamiltonian of some conformal field theory and Ψ is an arbitrary perturbation. The approach employs the Hilbert space of the conformal field theory as a computational basis and exploits the ability to compute matrix elements of the perturbing field in this same basis using the constraints afforded by the conformal symmetry. It was first employed by Yurov and Zamolodchikov in studies of massive perturbations of the critical Ising model [41] and the scaling Yang-Lee model [21].

Since its introduction it has been used in a large number of instances and to some degree has become a standard tool. It has been used to study perturbations of the tricritical Ising [47, 48], the 3-states Potts model [49], bosonic ($c = 1$) compactified theories

[51], the sine-Gordon model [52, 53], and perturbations of boundary conformal field theories [54]. Spectral flows between different conformal field theories were addressed in Ref. [55], while the correctness of the thermodynamic Bethe ansatz equations was checked in Refs. [56, 57]. Finite-size corrections to the mass spectra have also been analyzed in Refs. [58, 59]. By replacing the conformal field theory with an integrable field theory, the approach can also study models of perturbed integrable field theories. Matrix elements of the perturbing field are then computed in the form factor bootstrap approach [60].

While the TCSA approach is extremely flexible in the models it can attack, it is in practice limited to perturbations of conformal field theories with small central charge ($c < 1$). For theories with large central charge, the underlying conformal Hilbert space is large and becomes numerically burdensome to manipulate. The difficulty has recently been partially overcome with the development of a numerical renormalization group (NRG) for the TCSA [61, 62, 63, 64, 65]. This renormalization group permits large Hilbert spaces to be dealt with piecewise making the numerics manageable. Using this renormalization group, the excitation spectrum of semi-conducting carbon nanotubes was studied [64] (here the underlying conformal field theory had $c = 4$) as were large arrays of coupled quantum Ising chains [62] (here the underlying conformal field theory had $c \sim 30 - 50$).

The TCSA approach, as designed, focuses on accurately computing the properties of the low energy states. However when combined with an NRG together with a sweeping algorithm not dissimilar to the finite volume algorithm of the DMRG [15], the TCSA can compute the properties of states over a wide range of energies. This was demonstrated in [63] where the level spacing statistics were studied in crossing over from an integrable to a non-integrable model.

In the first part of this Chapter, we apply the TCSA to perturbations of Wess-Zumino-Witten (WZW) models. WZW models are non-linear sigma models, i.e. field theories whose field¹, Φ , lives on a group manifold \mathcal{G} , of a *non-Abelian* Lie-group. In addition to non-linear sigma models they possess topological terms, the Wess-Zumino term, whose action is quantized with the consequence that its coupling constant k is constrained to be a positive integer. The consequence of the topological term is to make the sigma models conformal with the affine Lie algebra associated with \mathcal{G} , spectrum generating². Affine Lie algebras typically have richer structure than the Virasoro algebra and are consequently more difficult to treat with the TCSA. Specialized code needs to be developed in order to treat such models. Here we report the development of such code for the study of perturbations of $SU(2)_k$ WZW models.

Perturbed $SU(2)_k$ WZW models are interesting physically primarily because they are

¹assuming to have just one field.

²This is true just if the group is non-Abelian. For an Abelian group, for instance $U(1)$, the non linear sigma-model is already conformal without the need of the topological term.

able to represent the low energy structure of spin chains [66]³. The most important example here is the spin-1/2 Heisenberg chain, whose low energy behavior is governed by $SU(2)_1$ perturbed by a marginally irrelevant current-current interaction. Adding different perturbations to $SU(2)_1$ leads to different variants of the Heisenberg model. The Hamiltonian

$$H = H_{SU(2)_1} + g \int dx \bar{J}_R \cdot \bar{J}_L + h \int dx (\phi_{1/2,1/2} \bar{\phi}_{1/2,-1/2} - \phi_{1/2,-1/2} \bar{\phi}_{1/2,1/2}), \quad (1.2)$$

where $\phi_{1/2,\pm 1/2}$ are the spin-1/2 fields in $SU(2)_1$, is the low energy reduction of the dimerized $J_1 - J_2$ Heisenberg model

$$H = \sum_n J_1 (1 + \delta(-1)^n) \bar{S}_n \cdot \bar{S}_{n+1} + J_2 \bar{S}_n \cdot \bar{S}_{n+2}. \quad (1.3)$$

The couplings of the two models are related via $g \propto J_2 - J_{2c}$ and $h \propto \delta$. This model has been studied intensely both field theoretically with RG analyses [67] and with DMRG [68, 69]. These methodologies do not currently agree on how the spin gap depends upon the dimerization parameter δ . It is one of the aims of our work to set up the framework under which disputed questions surrounding this model can be addressed.

$SU(2)_k$ for $k > 1$ WZW theories are also of considerable interest as they are the low energy reductions of families of spin- $k/2$ spin chains with finely tuned, local interactions [66]. They have also been shown more recently to represent Haldane-Shastry type spin chains [50] with longer range interactions [70, 71, 72]. In both cases, it is of interest to understand how $SU(2)_k$ WZW behaves in the presence of relevant and marginal perturbations. And more generally, because $SU(2)_k$ WZW theories are multi-critical with many possible relevant perturbations. Actual spin chains are likely to be realized only in the vicinity of these critical points rather than precisely at them.

In the final part of this Chapter we also apply the TCSA to Landau-Ginzburg Theories (LG). These theories were introduced within the context of second-order phase transitions and later used to model type-I superconductors [73]. LG theories provide effective descriptions in terms of the order parameter.

Already at the mean field level, these theories give a first approximation of critical exponents, and help to understand the mechanism behind the phase transitions. A very important example is the Ising model in $1 + 1$ dimensions, which exhibits a transition between a paramagnetic phase at high temperature and a ferromagnetic phase at low temperature. The action of the corresponding LG theory for the order parameter ϕ (the magnetization) is

$$\mathcal{S} = \frac{1}{8\pi} \int d^2x \left[\frac{1}{2} \partial^\mu \phi \partial_\mu \phi + g_2 \phi^2 + g_4 \phi^4 \right], \quad g_4 > 0 \quad (1.4)$$

³There are others applications in high-energy physics which we are not concerned with.

where the coupling g_2 is proportional to $T - T_C$, T_C being the critical temperature. Hence, if the coupling is positive the potential has just one stable minimum at zero magnetization, corresponding to the paramagnetic phase, while if $g_2 < 0$ the shape changes and two minima with finite magnetization appear. A spontaneous symmetry breaking mechanism leads to the choice of one minimum, which gives the ferromagnetic phase.

Although very simple, the presented mean field considerations about the phase transition can be extended to a large variety of systems. Moreover, fluctuations of the order parameter can be included to enrich the information about the system by just promoting the LG theory to a quantum field theory. These quantum field theories are typically non-integrable and thus quite challenging for analytical studies.

A crucial task is to compute their spectrum of stable excitations, which is the basic information for building up their space of states and for proceeding further in the analysis of the dynamics, with the computation of scattering processes, matrix elements, correlation functions, etc.

The determination of such a spectrum is however a dynamical problem in itself: what usually happens, in fact, is that the elementary fields present in the Lagrangian of a model do not exhaust the spectrum of stable excitations, which may indeed contain additional bound states. Assuming one would be able to solve exactly the dynamics of the theory, the whole spectrum could be read from the poles placed in the physical strip of the various S -matrix amplitudes.

Such a procedure is known to work perfectly well with 2D Integrable Quantum Field Theories (IQFT) [80] and has lead to an exact solution of many models, among which the Sine-Gordon and the Gross-Neveu models, or the Ising model in a magnetic field⁴.

However, relatively few analytic methods are available to make progress in non-integrable models. Focusing the attention on two-dimensional quantum field theories, there are, beside the standard perturbation theory, essentially two techniques:

- Form Factor Perturbation Theory [42, 43], a method particularly suited to study those non-integrable field theories obtained as deformations of integrable models. A prototype example may be considered the multi-frequency Sine-Gordon model, whose Lagrangian contains two or more cosines of different frequencies [43].
- the Semiclassical Method [44, 45, 46], that can be used to analyze in relatively simple terms non-integrable field theories with topological (kink-like) excitations of very high mass.

⁴It is particularly important to have mentioned the Sine-Gordon and the Gross-Neveu models because, in both cases, it is well known that the spectrum of their stable excitations is much richer than what one can infer from their Lagrangians [80]. It must be also added that in Integrable Quantum Field Theories there could be stable excitations whose mass m is higher than the natural energy threshold $E = 2m_1$ dictated by the lowest mass excitation m_1 : their stability is ensured in this case by the infinite number of conservation laws which characterizes the integrable dynamics.

At the present time, many semi-classical predictions have been derived [44, 45, 46], but some of them are still at the level of conjecture [46].

It is thus important to set-up a numerical method to study these quantum field theories efficiently, as discussed in the final part of this Chapter. By applying an adapted version of the TCSA to LG theories, we will show that the conjecture proposed in Ref. [46] about the number of possible stable neutral bound states is verified in the LG theories addressed.

The outline of this Chapter is as follows. In Section 1.1 we give fundamental ingredients of $SU(2)_k$ WZW models, while in Section 1.2 we present the TCSA applied to perturbations of $SU(2)_k$ are studied. In the next three sections (Section 1.3 to Section 1.5) we present applications of the TCSA to perturbed $SU(2)_k$ models to confirm that how the method properly applies to these kind of theories. In particular in Section 1.3 we examine the $SU(2)_1 + Tr(g)$ model, which is equivalent to the sine-Gordon model. This allows us to compare our numerics with known analytic results. In Section 1.4 we study the $SU(2)_1 + \bar{J}_L \cdot \bar{J}_R$ model, which corresponds to a marginal current-current perturbation of $SU(2)_1$. We show here that one can isolate the UV divergent behavior, essential for extracting the universal behavior of spin chains described by $SU(2)_k$ with a marginal perturbation. Finally, in Section 5., we consider $SU(2)_2$ perturbed by $Tr(g)^2$. This provides a useful benchmark of our methodology as the theory is equivalent to three non-interacting massive Majorana fermions. In Section 1.6 we than comment about our results on $SU(2)_k$ and present possible future developments. In Section 1.7 the structure of the expected stable excitation spectrum in Landau-Ginzburg theories is presented, while in Section 1.8 we are going to adapt the TCSA to study Landau-Ginzburg theories. The method is used to verify the semi-classical predictions in [46] in Section 1.9. In Section 1.8.3 the NRG is also applied to LG theories. We conclude and discuss about the applicability of TCSA to LG theories in Section 1.10. Appendix A contains basics ingredients of thermodynamics Bethe ansatz used along the Chapter.

1.1 An introduction to Wess-Zumino-Witten models.

In this Section we introduce those fundamentals on WZW models which will be required in this thesis. WZW theories are non-linear sigma models – i.e. models where the field is valued on a manifold, in the following the $SU(2)$ -Lie group – modified by a topological term that makes the full theory a conformal field theory [33, 34]. The starting point of the construction is the non-linear sigma model

$$S_0 = \frac{1}{4a^2} \int d^2x Tr [\partial^\mu \Phi^{-1} \partial_\mu \Phi] \quad (1.5)$$

where Φ takes value on $SU(2)$ and a is a positive dimensionless constant. The equations of motion have the form⁵

$$\partial^\mu (\Phi^{-1} \partial_\mu \Phi) = 0 \quad (1.6)$$

that imply conservation laws for the currents $J_\mu = \Phi^{-1} \partial_\mu \Phi$. In complex coordinates, (z, \bar{z}) , they become

$$\partial_{\bar{z}} J_z + \partial_z \bar{J}_{\bar{z}} = 0, \quad (1.7)$$

where

$$J_z = \Phi^{-1} \partial_z \Phi \text{ and } \bar{J}_{\bar{z}} = \Phi^{-1} \partial_{\bar{z}} \Phi \quad (1.8)$$

If both the terms in Eq. (1.7) vanish separately, the identity is satisfied and we have the typical separation of the holomorphic and antiholomorphic sectors of conformal field theories. However it is easy to prove, that this occurs just if Φ is valued on an Abelian group⁶ which is interesting for the last part of the Chapter, when we are going to apply the TCSA to theories with $U(1)$ symmetry⁷.

Even though the non-linear sigma model S_0 with $SU(2)$ -symmetry is not conformal, it has been show in Ref. [33, 34] that the conformal symmetry can be restored by modifying the action with a topological term Γ ,

$$\mathcal{S} = S_0 + k\Gamma, \quad (1.10)$$

defiend as

$$\Gamma = -\frac{i}{24\pi} \int_{\mathcal{B}} d^3y \epsilon_{\alpha\beta,\gamma} Tr \left[\tilde{\Phi}^{-1} \partial^\alpha \tilde{\Phi} \tilde{\Phi}^{-1} \partial^\beta \tilde{\Phi} \tilde{\Phi}^{-1} \partial^\gamma \tilde{\Phi} \right]. \quad (1.11)$$

In (1.11) $\tilde{\Phi}$ are $SU(2)$ -valued extension of Φ , defined on a 3-dimensional manifold \mathcal{B} which boundary is the compactification of the domain of Φ . Albeit the extension is obviously not unique, the Γ term changes by just by multiples of $2\pi i$ if different $\tilde{\Phi}$ are considered; hence the action remains unchanged and it is perfectly well defined.

The coupling in front of the topological term is consequently quantized to be an integer, called *level* of the theory. We will thus refer to the model described by \mathcal{S} as $SU(2)_k$ WZW model.

⁵A fundamental ingredient in the computation is $\partial_\mu \Phi^{-1} = \Phi^{-1} \partial_\mu \Phi \Phi^{-1}$. This can be obtained just realizing that $\partial_\mu (\Phi \Phi^{-1}) = 0$. Similarly, since $\delta(\Phi \Phi^{-1}) = 0$, it follows that $\delta \Phi^{-1} = \Phi^{-1} \delta \Phi \Phi^{-1}$.

⁶By performing the derivative of the equation of motion in complex coordinates ($\partial_z (\Phi^{-1} \partial_{\bar{z}} \Phi) = 0$ and $\partial_{\bar{z}} (\Phi^{-1} \partial_z \Phi) = 0$) and using the identity $\partial_\mu \Phi^{-1} = -\Phi^{-1} \partial_\mu \Phi \Phi^{-1}$ we find

$$\partial_{\bar{z}} \Phi \Phi^{-1} \partial_z \Phi = \partial_z \Phi \Phi^{-1} \partial_{\bar{z}} \Phi \quad (1.9)$$

which, once defined $A = \partial_{\bar{z}} \Phi \neq 0$, $B = \Phi^{-1} \neq 0$, and $C = \partial_z \Phi \neq 0$, reads as $ABC = CBA$, and has non-trivial solution just in commutative groups.

⁷The $U(1)$ -group is commutative, hence the non-linear sigma model is going to be conformal, and additional terms in the action are not needed..

Although, the topological term is defined on a three-dimensional manifold its variation defines a total derivative

$$\delta\Gamma = \frac{i}{8\pi} \int d^2x \epsilon_{\alpha\beta} \text{Tr} [\Phi^{-1} \delta\Phi \partial^\alpha (\Phi^{-1} \partial^\beta \Phi)] \quad (1.12)$$

and it is equivalent to a two dimensional functional. The introduction of this term results in the modified equations of motion:

$$\left(1 + \frac{ka^2}{4\pi}\right) \partial_z (\Phi^{-1} \partial_{\bar{z}} \Phi) + \left(1 - \frac{ka^2}{4\pi}\right) \partial_{\bar{z}} (\Phi^{-1} \partial_z \Phi) = 0 \quad (1.13)$$

The choice $a^2 = \pm \frac{4\pi}{k}$ gives either $\partial_z (\Phi^{-1} \partial_{\bar{z}} \Phi) = 0$ or $\partial_{\bar{z}} (\Phi^{-1} \partial_z \Phi) = 0$.

In order to compute the conserved currents we consider infinitesimal transformations

$$\delta_\omega \Phi = \omega \Phi \text{ and } \delta_{\bar{\omega}} \Phi = -\bar{\omega} \Phi \quad (1.14)$$

with ω an element of the $su(2)$ algebra. If $a^2 = \frac{4\pi}{k}$, the variations (1.14) result in

$$\delta\mathcal{S} = \frac{k}{2\pi} \int d^2x \text{Tr} [\omega(z) \partial_{\bar{z}} (\partial_z \Phi \Phi^{-1}) - \bar{\omega}(\bar{z}) \partial_z (\Phi^{-1} \partial_{\bar{z}} \Phi)] \quad (1.15)$$

and we can extract the two currents

$$J = -k \partial_z \Phi \Phi^{-1} \text{ and } \bar{J} = k \Phi^{-1} \partial_{\bar{z}} \Phi \quad (1.16)$$

which are separately conserved:

$$\partial_{\bar{z}} J_z = 0 \text{ and } \partial_z \bar{J}_{\bar{z}} = 0. \quad (1.17)$$

This result evidences the underlying conformal symmetry. We now want to clarify the role of the $SU(2)$ symmetry in the construction of the states of the conformal field theory.

Infinitesimal transformations of the conserved currents, using (1.16) and (1.14), have the form

$$\begin{aligned} \delta_\omega J_z &= -k \partial_z (\delta_\omega \Phi) \Phi^{-1} - k \partial_z \Phi \delta_\omega \Phi^{-1} \\ &= [\omega, J] - k \partial_z \omega, \end{aligned} \quad (1.18)$$

and a similar expression for the antiholomorphic current, an equivalent expression being

$$\begin{aligned} \delta_\omega J^a &= i f_{abc} \omega^b J^c - k \partial_z \omega \\ \delta_{\bar{\omega}} \bar{J}^a &= i f_{abc} \bar{\omega}^b J^c - k \partial_{\bar{z}} \bar{\omega}, \end{aligned} \quad (1.19)$$

where f_{abc} are the $SU(2)$ structure constants.

If X is a generic operator, the Ward identities obtained from (1.15) by moving to complex integration variables⁸ have the form

$$\delta_{\omega, \bar{\omega}} \langle X \rangle = -\frac{1}{2\pi i} \oint dz \omega^b \langle J^b X \rangle + \frac{1}{2\pi i} \oint d\bar{z} \bar{\omega}^b \langle \bar{J}^b X \rangle, \quad (1.20)$$

⁸We have $d^2x = -\frac{i}{2} dz d\bar{z}$.

such that in the case where $X = J^a$, and using (1.19), the identity is consistent with the operator product expansion (OPE):

$$J^a(z) \cdot J^b(w) \sim \frac{k\delta_{ab}}{(z-w)^2} + \frac{if_{abc}}{z-w} J^c(w) + \dots \quad (1.21)$$

Modes of the currents are then defined as

$$J^a(z) = \sum_n \frac{J_n^a}{z^{n+1}} \quad (1.22)$$

and the OPE is consistent with the following algebra for the modes:

$$[J_n^a, J_m^b] = if_{abc} J_{n+m}^c + nk\delta_{ab}\delta_{n+m,0} \quad (1.23)$$

These commutation relations define what is typically called $SU(2)_k$ Kac-Moody algebra. It belongs to the class of Affine Lie Algebras, well studied in mathematics [22]. As we are going to show, this is the spectrum generating algebra of the $SU(2)_k$ WZW model.

The stress energy tensor of these theories is a bilinear operator in the currents, and it can be computed within the so called Sugawara construction [22]:

$$T(z) = \frac{1}{2(k+2)} : J^a(z) J^a(z) : \quad (1.24)$$

By just by comparing the mode expansion

$$T(z) = \sum_n \frac{L_n}{z^{n+2}} \quad (1.25)$$

with (1.22) one finds

$$L_n = \frac{1}{2(k+2)} \sum_m : J_m^a J_{n-m}^a : \quad (1.26)$$

which relates the conformal Virasoro modes with the $SU(2)_k$ modes, and explains why the $SU(2)_k$ algebra is the spectrum generating algebra of the $SU(2)_k$ WZW model. The central charge is computed by performing the OPE of the stress-energy tensor with itself and by using its decomposition into current modes. The fourth-order pole of the resulting expansion contains the central charge, whose expression is the $SU(2)$ -specification of the so called Sugawara-formula:

$$c = \frac{3k}{k+2}. \quad (1.27)$$

The operator content of the theory will be discussed in the construction of the computational basis for the TCSA in the next Section.

We remark that this construction holds for every Lie Group once the correct structure constants f_{abc} are considered. In the last part of the Chapter a different current algebra will be studied: the $U(1)_1$, the spectrum generating algebra of the compactified boson.

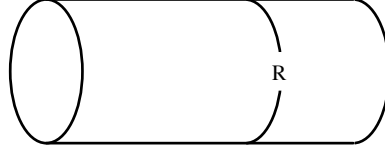


Figure 1.1: The WZW field Φ is defined on an infinite cylinder of radius R .

1.2 TCSA for $SU(2)_k$ WZW models

In this Section we describe the application of the TCSA [21] to deformations of the $SU(2)_k$ Wess-Zumino-Witten model [74, 75]. We thus start by considering Hamiltonians of the form

$$H = H_{SU(2)_k} + g \int_0^R dx \Psi(x). \quad (1.28)$$

Here Ψ is a spin singlet combination of (highest weight or current) fields of the WZW model. The Hamiltonian is defined on a circle of length R . Adding the time coordinate the underlying space-time is an infinite cylinder with circumference R (see Fig. 1.1).

The first step in the TCSA is to characterize the unperturbed theory, $H_{SU(2)_k}$. This theory provides the computational basis of the TCSA numerics. $H_{SU(2)_k}$ has central charge $c = 3k/(k+2)$ ($k = 1, 2, \dots$), and can be written à la Sugawara in terms of the $SU(2)_k$ currents:

$$\begin{aligned} H_{SU(2)_k} &= \frac{2\pi}{R} \left(L_0 + \bar{L}_0 - \frac{c}{12} \right) \\ &= \frac{2\pi}{R} \left(\sum_m : \left[(2J_m^0 J_{-m}^0 + J_m^+ J_{-m}^- + J_m^- J_{-m}^+) \right. \right. \\ &\quad \left. \left. + (2\bar{J}_m^0 \bar{J}_{-m}^0 + \bar{J}_m^+ \bar{J}_{-m}^- + \bar{J}_m^- \bar{J}_{-m}^+) \right] : - \frac{c}{12} \right). \end{aligned} \quad (1.29)$$

The left-moving currents $J_m^{0,\pm}$ obey the algebra,

$$\begin{aligned} [J_m^0, J_n^0] &= \frac{km}{2} \delta_{n+m,0}, \\ [J_m^0, J_n^\pm] &= \pm J_{m+n}^\pm, \\ [J_m^+, J_n^-] &= 2J_{m+n}^0 + km \delta_{m+n,0}, \end{aligned} \quad (1.30)$$

with the right moving currents $\bar{J}_m^{0,\pm}$ obeying the same algebra. These commutation relations are trivially equivalent to (1.23).

The field content of $H_{SU(2)_k}$ consists of $k+1$ primary fields, $\phi_{s,m=-s,\dots,s}$, forming spin $s = 0, \dots, k/2$ representations. The conformal weight of the spin s primary field is given by

$$\Delta_s = s(s+1)/(k+2). \quad (1.31)$$

The primary fields and the WZW currents are the basic tools to construct the Hilbert space of the unperturbed theory, providing the first ingredient of the TCSA. The Hilbert space can be written as a tensor product of its holomorphic (left) and anti-holomorphic (right) degrees of freedom. For $SU(2)_k$, the left and right sectors of the Hilbert space have $k+1$ modules each, one for every allowed spin. Each module is associated to one primary field, $\phi_{s,s}$ that defines the highest weight state (or primary state), $|s, s\rangle \equiv \phi_{s,s}(0)|0\rangle$. The module contains this primary state together with an infinite tower of descendant states:

$$J_{-n_M}^{a_M} \dots J_{-n_1}^{a_1} |\phi_{s,s}\rangle, \quad n_i = 0, 1, 2, \dots \quad a_i = 0, \pm. \quad (1.32)$$

These states (1.32) are eigenstates of the Virasoro operator L_0 , and the third component component of the current J_0^0 :

$$\begin{aligned} L_0 (J_{-n_M}^{a_M} \dots J_{-n_1}^{a_1}) |s, s\rangle &= \left[\Delta_s + \sum_i n_i \right] (J_{-n_M}^{a_M} \dots J_{-n_1}^{a_1}) |s, s\rangle; \\ J_0^0 (J_{-n_M}^{a_M} \dots J_{-n_1}^{a_1}) |s, s\rangle &= \left[s + \sum_i a_i \right] (J_{-n_M}^{a_M} \dots J_{-n_1}^{a_1}) |s, s\rangle. \end{aligned} \quad (1.33)$$

The quantity $\sum_i n_i$ is called the Kac-Moody level, or simply the level, of the descendant state.

We can give a simple argument that explains the truncated number of representation in the theory. Let us consider the matrix element $\langle s, s | J_1^- J_{-1}^+ | s, s \rangle$. This is a norm, and thus surely non-negative. Therefore, by using (1.31) we have

$$0 \leq \langle s, s | J_1^- J_{-1}^+ | s, s \rangle = \langle s, s | [J_1^-, J_{-1}^+] | s, s \rangle = -2s + k$$

which implies

$$s \leq \frac{k}{2} \quad (1.34)$$

and evidences the existence of an upper bound for the possible primary state of the theory.

The set of states (1.32) is not yet a basis of the Hilbert space since it is over complete and contains null states. In order to form a complete orthonormal basis, we tackle each Kac-Moody module separately.

We do so in an iterative fashion. At each step we have a set of non-zero norm states which are linearly independent (at the beginning this set will consist solely of the highest weight state). We next add a new descendant state to this set, compute the matrix of scalar products of states in the expanded set (the Gramm matrix), and find its determinant. If it is non-zero, the new state is added to the list; otherwise it is discarded. We then move to the next descendant in the tower of states in increasing order in the

	$SU(2)_1$		$SU(2)_2$		
level	I	1/2	I	1/2	1
0	1	2	1	2	3
1	4	4	4	8	7
2	8	10	13	20	19
3	15	18	28	46	40
4	28	32	58	94	83
5	47	52	112	178	152
6	76	86	206	324	275
7	119	132	359	564	468
8	181	202	611	948	786
9	271	298	1002	1552	1272
10	397	436	1611	2482	2026
11	571	622	2529	3886	3145

Table 1.1: The dimensions of the Verma modules of $SU(2)_1$ and $SU(2)_2$ at different levels.

level. The process ends when all the states up to a given truncation level have been considered.

This procedure yields a complete set of states that we can easily orthonormalize to obtain a basis. In order to optimize this procedure we take into account the following properties:

- states with different L_0 quantum number are independent;
- states having different spin (eigenvalue of J_0^0) are independent;
- we discard the states with null norm;
- we act only with level 0 currents, $J_0^{0,\pm}$, directly on the highest weight state $|s, s\rangle$ in the module.

To demonstrate that the above method amounts to a numerically intensive task, we present in Table I the number of states per level for the two modules of $SU(2)_1$ and the three modules of $SU(2)_2$.

Once the chiral sector of $SU(2)_k$ has been obtained, the total Hilbert space is constructed as a tensor product of the isomorphic holomorphic and antiholomorphic sectors. These tensor products are diagonal in the modules, i.e. left moving spin s states are only tensored with their right moving spin s counterparts. In forming these tensor products, we group the states by their value of Lorentz spin, $(L_0 - \bar{L}_0)$, and z -component of $SU(2)$ spin, $J_0^0 + \bar{J}_0^0$. Recall that the Lorentz spin is proportional to the momentum carried by

$SU(2)_1$ level	mom. 0	$SU(2)$ spin 0	$SU(2)_2$ level	mom. 0	$SU(2)$ spin 0
1	18	8	1	75	25
2	70	24	2	444	120
5	1309	381	4	6839	1595
11	133123	32021	7	185111	38665

Table 1.2: The cumulative dimensions for non chiral spaces at given level with total Lorentz spin (mom.) zero (first column) and both Lorentz spin and $SU(2)$ spin S_z zero (second column).

$SU(2)_1$			
$C_{0,0;1/2,-1/2;1/2,1/2}$	1	$C_{1/2,1/2;1/2,1/2;0,0}$	1
$SU(2)_2$			
$C_{0,0;1/2,-1/2;1/2,1/2}$	1	$C_{1,1;1,1;0,0}$	1
$C_{0,0;1,-1;1,1}$	1	$C_{1,1;1/2,1/2;1/2,1/2}$	1
$C_{1/2,1/2;1/2,1/2;0,0}$	1	$C_{1/2,1/2;1/2,-1/2;1,1}$	-1
$C_{1/2,1/2;1,0;1/2,1/2}$	$-\frac{1}{\sqrt{2}}$		

Table 1.3: Non zero structure constants of $SU(2)_1$ and $SU(2)_2$.

the corresponding state. In Table 1.2 we present the number of cumulative states up to a given level in $SU(2)_1$ and $SU(2)_2$ with vanishing Lorentz spin.

Once the computational basis has been constructed, the TCSCA requires the evaluation of matrix elements of the perturbing operator in that basis. For this purpose one uses the commutation relations of the fields, $\phi_{s,m}(0)$, with the current modes, $J_0^{0,\pm}$, which are given by

$$\begin{aligned} [J_0^0, \phi_{s,m}] &= m \phi_{s,m}; \\ [J_0^\pm, \phi_{s,m}] &= (s \pm m) \phi_{s,m \pm 1}. \end{aligned} \quad (1.35)$$

With these commutation relations and those of the current modes (1.30), matrix elements of the form

$$\langle \phi_{s,s} | J_{n_1}^{a_1} \cdots J_{n_m}^{a_m} \phi_{s',m}(0,0) J_{-l_1}^{b_1} \cdots J_{-l_k}^{b_k} | \phi_{s'',s''} \rangle, \quad (1.36)$$

can be reduced to the structure constants, $C_{s_1,m_1;s_2,m_2;s_3,m_3}$:

$$\langle \phi_{s,s} | \phi_{s',m}(0) | \phi_{s'',s''} \rangle = \left(\frac{2\pi}{R} \right)^{2\Delta_s} C_{s,s;s',m;s'',s''}. \quad (1.37)$$

We list all non-zero structure constants, $C_{s_1,m_1;s_2,m_2;s_3,m_3}$ in Table III for $SU(2)_1$ and $SU(2)_2$.

With the spectrum of the unperturbed $SU(2)_k$ model specified and the matrix elements of the perturbing field given, we are able to compute explicitly the matrix elements of the full Hamiltonian on the circle and represent it in matrix form. To be able to analyze this Hamiltonian, we truncate (the truncation in the acronym TCSA) the Hilbert space by discarding all states with a chiral component whose level is greater than N_{tr} . The resulting *finite* dimensional Hamiltonian matrix can then be diagonalized numerically, obtaining the spectrum of the perturbed theory. This procedure is particularly robust for relevant perturbations since the low energy eigenstates of the perturbed theory, $|r\rangle$, are localized on the low energy conformal states, $\{|c\rangle_\alpha\}$. Namely, expanding $|r\rangle$ into the conformal basis, $\{|c\rangle_\alpha\}$,

$$|r\rangle = \sum_{\alpha} b_{\alpha} |c\rangle_{\alpha}, \quad (1.38)$$

the coefficients b_{α} , are primarily concentrated on the low energy conformal states $|c\rangle_{\alpha}$ determined by $H_{SU(2)_k}$.

To extract physical quantities for the perturbed Hamiltonian (1.28), such as the mass gap, energy levels, correlation functions, etc., the choice of the system size, R , requires special consideration. For $mR \ll 1$ (here m is the putative mass scale of the perturbed theory), the system lies in the UV limit where the conformal term, $H_{SU(2)_k}$, of the full Hamiltonian dominates. In this regime the spectrum resembles that of the conformal $H_{SU(2)_k}$ where the energy levels scales as $1/R$. In the IR regime, $Rm \gg 1$, the perturbation, $\int dx \Phi(x)$, dominates and one expects a scaling of the form $\sim R^{1-2\Delta_s}$, where $2\Delta_s$ is the scaling dimension of the perturbing field. In general, the spectrum of the perturbed model must be extracted in a region of R where the conformal term and the perturbation are balanced in the sense that physical quantities remains stable under small variations of R . This region is usually denoted as the “scaling region”.

For theories where the dimension of the Hilbert space grows very fast, i.e. $SU(2)_k$ with k large, the truncation scheme proposed above may not yield accurate results.

In those cases one can take recourse to a numerical renormalization group (NRG) improvement of the TCSA [61, 62, 63, 64, 65]. This procedure allows the TCSA to reach much higher truncation levels than that possible in its unadorned form. Taken together with an analytic renormalization group, it is possible to remove the effects of truncation altogether [61]. While this NRG has been tested extensively on relevant perturbations of conformal field theories, it has not been tried on marginal perturbations of CFTs. We will show in Section IV that the NRG can accurately predict the low lying spectrum even in the marginal case.

1.3 $SU(2)_1$ perturbed by the spin-1/2 field

Our first test of the TCSEA is the perturbation of the $SU(2)_1$ WZW model by the singlet formed from the spin-1/2 operator of $SU(2)_1$,

$$\Psi = (\phi_{1/2,1/2} \bar{\phi}_{1/2,-1/2} - \phi_{1/2,-1/2} \bar{\phi}_{1/2,1/2}),$$

the Hamiltonian being

$$H_{rel} = H_{SU(2)_1} + h \int dx \Psi(x). \quad (1.39)$$

The scaling dimension of Ψ is $2\Delta_{1/2} = 1/2$, and so this is a relevant perturbation. Moreover the theory is invariant under $h \rightarrow -h$. This Hamiltonian is equivalent to the sine-Gordon model whose Lagrangian is given by [76]

$$L_{SG} = \int d^2x \left(\frac{1}{2} (\partial_\mu \varphi)^2 + 2\lambda \cos(\beta\varphi) \right), \quad (1.40)$$

with $\beta^2 = 2\pi$. The correspondence between (1.39) and (1.40) is based on the identifications

$$\phi_{1/2,1/2}(z) =: e^{\frac{1}{\sqrt{2}}\varphi(z)} : \quad \text{and} \quad \phi_{1/2,-1/2}(z) =: e^{-\frac{1}{\sqrt{2}}\varphi(z)} : \quad (1.41)$$

which, up to phase redefinitions, are the bosonization formulas of the $SU(2)_1$ model [22]. The vertex-operators representation of the current within our conventions are

$$\begin{aligned} J^0 &= \frac{i}{\sqrt{2}} \partial\varphi \\ J^\pm &= : e^{\pm i\sqrt{2}\varphi} : \end{aligned} \quad (1.42)$$

It is easy to show, by just using elementary properties of vertex operators such as

$$\begin{aligned} \partial\varphi(z) \cdot \mathcal{V}_\alpha(0) &\sim -\frac{i\alpha\mathcal{V}_\alpha(0)}{z}, \\ e^{i\alpha\varphi(z)} \cdot e^{i\beta\varphi(0)} &\sim |z|^{2\alpha\beta} e^{i(\alpha+\beta)\varphi(z)}, \text{ and} \\ e^{i\alpha\varphi(z)} \cdot e^{i\alpha\varphi(0)} &\sim |z|^{2\alpha^2} \left(1 + i\alpha \sum_{n>0} \frac{\partial^{(n)}\varphi}{n!} z^n \right), \end{aligned} \quad (1.43)$$

that our definitions provide a representation of the algebra (1.31):

$$\begin{aligned} [J^0, J^\pm] &\sim \frac{i}{\sqrt{2}} \partial\varphi \cdot e^{\pm i\sqrt{2}\varphi} \sim -\pm i\sqrt{2} \frac{i}{\sqrt{2}} e^{\pm i\sqrt{2}\varphi} / z \rightarrow \pm J^\pm \\ [J^+, J^-] &\sim e^{i\sqrt{2}\varphi} \cdot e^{-i\sqrt{2}\varphi} \sim \frac{1}{z^2} + \frac{i\sqrt{2}\partial\varphi}{z} \rightarrow 1 + 2J^0. \end{aligned} \quad (1.44)$$

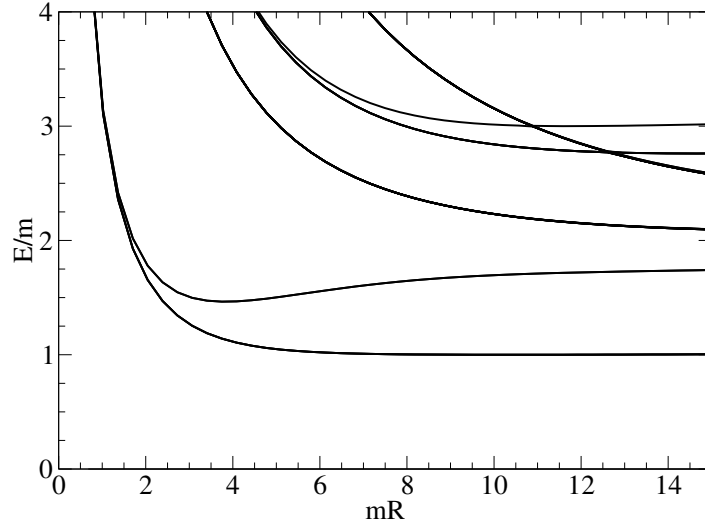


Figure 1.2: Plot of the TCSA data for the lowest six excited states in the $S_z = 0$ sector with the ground state energy subtracted. The lowest two excited states correspond to B_1 (the $S_z = 0$ state of the triplet) and B_2 . The next four excited states are two particle states. The data are computed with a truncation level $N_{\text{tr}} = 9$. The fundamental triplet of particles can be seen to have mass $M=1.0016$.

The commutators between primaries and the currents (1.35) are also derived from:

$$\begin{aligned}
 [J^0, \phi_{1/2, \pm 1/2}] &\sim \frac{i}{\sqrt{2}} \partial \varphi \cdot e^{\pm \frac{1}{\sqrt{2}} \varphi} \sim \pm \frac{1}{2} e^{\pm \frac{1}{\sqrt{2}} \varphi} / z \rightarrow \frac{1}{2} \phi_{1/2, \pm 1/2} \\
 [J^\mp, \phi_{1/2, \pm 1/2}] &\sim e^{\mp \sqrt{2} \varphi} \cdot e^{\pm \frac{1}{\sqrt{2}} \varphi} \sim |z|^{-2} e^{\mp \frac{1}{\sqrt{2}} \varphi} \rightarrow \phi_{1/2, \mp 1/2} \\
 [J^\pm, \phi_{1/2, \pm 1/2}] &\sim e^{\pm \sqrt{2} \varphi} \cdot e^{\pm \frac{1}{\sqrt{2}} \varphi} \sim |z|^{+2} e^{\mp \frac{1}{\sqrt{2}} \varphi} \rightarrow 0.
 \end{aligned}
 \tag{1.45}$$

We now show that the TCSA numerics reproduce the expected behavior of the sine-Gordon model. The spectrum of the sine-Gordon model at $\beta^2 = 2\pi$ is composed of a soliton S and antisoliton \bar{S} with mass M and two breathers B_1 and B_2 with masses $M_1 = M$ and $M_2 = \sqrt{3}M$ respectively. The soliton, anti-soliton, and the first breather form a triplet under $SU(2)$. The charges of the particles (S, B_1, \bar{S}) are given by $(1, 0, -1)$ and they coincide with their S_z quantum number. The second breather, B_2 , is a singlet under $SU(2)$.

Fig. 1.2 shows the low energy TCSA spectrum which reproduces the basic structure: a low lying triplet with mass M , and a single excitation at roughly $\sqrt{3}M$. The expected value of the mass M can be determined from the coupling constant used in the TCSA. The relation between the coupling of the sine-Gordon model and the mass M is given as

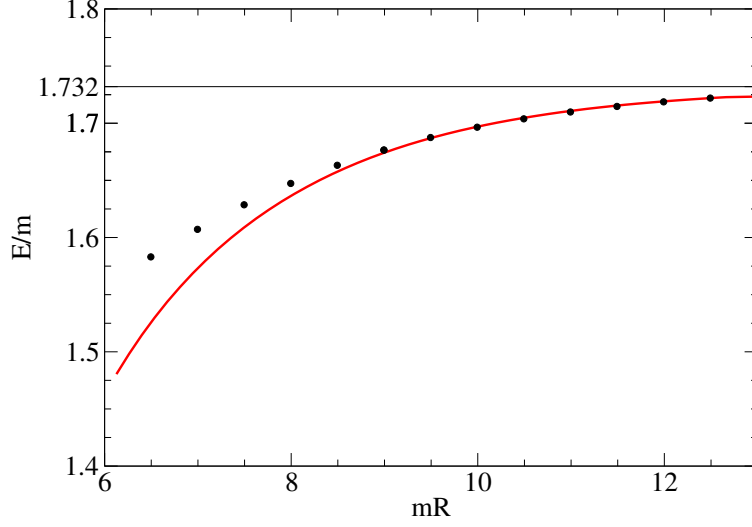


Figure 1.3: Single particle state B_2 : Analytic prediction for its mass with finite size effects (continuous line) compared to the TCSA data.

[77]

$$h = \lambda = \frac{\Gamma(\frac{\beta^2}{8\pi})}{\pi\Gamma(1 - \frac{\beta^2}{8\pi})} \left[M\sqrt{\pi} \frac{\Gamma(\frac{1}{2} + \frac{\xi}{2\pi})}{2\Gamma(\frac{\xi}{2\pi})} \right]^{2 - \frac{\beta^2}{4\pi}}, \quad (1.46)$$

where $\xi = \frac{\beta^2}{8} \frac{1}{1 - \frac{\beta^2}{8\pi}} = \frac{\pi}{3}$. With $h = 0.0942753..$ we expect the mass to be 1 while from the TCSA we find $\bar{M} = 1.0016$, in excellent agreement.

For the second breather, found roughly at $\sqrt{3}M$, a more careful analysis of the TCSA data is required. For this excitation there are significant finite size corrections. These corrections can be understood as virtual processes on the cylinder (first considered in [91] and later developed in more detail for one dimensional field theories in [58, 21]) which are suppressed exponentially as R becomes large. These corrections can be considered to have two contributions, the μ -term and the F-term [58]. The μ -term for B_2 is of the form

$$\Delta m_{B_2}^\mu(R) = -3\sqrt{3}e^{-MR/2}, \quad (1.47)$$

while the F-term equals

$$\Delta m_{B_2}^F(R) = \sum_i' \int_{-\infty}^{\infty} \frac{d\theta}{2\pi} e^{-m_i R \cosh \theta} m_i R \cosh(\theta) (S_{B_2, i}^{B_2, i}(\theta + i\pi/2) - 1), \quad (1.48)$$

where the sum \sum_i' runs over all particles in the theory where $S_{B_2, i}^{B_2, i}(\theta + i\pi/2)$ does not have a multiple pole for real θ . For completeness these S-matrices are as follows:

$$S_{\{S, \bar{S}, B_1\}, B_2}^{\{S, \bar{S}, B_1\}, B_2} = \frac{\sinh(\theta) + i \sin(\frac{\pi}{2}) \sinh(\theta) + i \sin(\frac{\pi}{6})}{\sinh(\theta) - i \sin(\frac{\pi}{2}) \sinh(\theta) - i \sin(\frac{\pi}{6})},$$

$$S_{B_2, B_2}^{B_2, B_2} = \frac{\sinh(\theta) + i \sin\left(\frac{2\pi}{3}\right) \sin^2\left(i\frac{\theta}{2} - \frac{\pi}{6}\right) \cos^2\left(i\frac{\theta}{2} + \frac{\pi}{6}\right)}{\sinh(\theta) - i \sin\left(\frac{2\pi}{3}\right) \sin^2\left(-i\frac{\theta}{2} - \frac{\pi}{6}\right) \cos^2\left(-i\frac{\theta}{2} + \frac{\pi}{6}\right)}. \quad (1.49)$$

For B_2 the only particle that satisfies the no multiple pole condition is B_2 itself. Thus the F-term for B_2 is of order $e^{-\sqrt{3}MR}$, and so considerably smaller than the μ -term. To determine whether we should include it at all we need to make an estimate of higher order terms of the finite size corrections (of order $e^{-\sigma_{B_2}R}$) neglected in the computation of μ - and F-terms. Using Ref. [58] as a guide we find $\sigma_{B_2} = 1$. Given that these higher order terms are larger than the F-term, we will henceforth ignore the F-term.

If we now fit $m_{B_2} + \Delta m_{B_2}(R)$ to the TCSA data, we find that $M_{B_2}/M = 1.7322 \pm 0.0002$. Using this mass, we plot $m_{B_2} + \Delta m_{B_2}$ against the TCSA data in Fig. 1.3. This shows excellent agreement between the theory and the TCSA data for $R > 9$.

We now turn to the ground state energy E_{gs} . The TCSA gives E_{gs} as would be computed in conformal perturbation theory to all orders. This perturbative energy can be expressed as the sum of a linear term in R , proportional to a bulk energy density, ϵ_{bulk} , plus a term given by the thermodynamic Bethe ansatz E_{TBA} [79, 21].

$$E_{gs} = \epsilon_{\text{bulk}}R + E_{TBA}(R). \quad (1.50)$$

The bulk contribution to E_{gs} is given by [80]

$$\epsilon_{\text{bulk}} = -\frac{M^2}{4} \tan \frac{\xi}{2} = -\alpha M^2 R. \quad (1.51)$$

For sine-Gordon with $\beta^2 = 2\pi$, $\alpha = 0.14438\dots$. The contribution from $E_{TBA}(R)$ is given by the solution of a coupled set of integral equations involving the S -matrices of the various excitations in the model [79, 21]. At large R , this contribution reads

$$\begin{aligned} E_{TBA}(R) = & -3M \int_{-\infty}^{\infty} \frac{d\theta}{2\pi} \cosh(\theta) e^{-MR \cosh(\theta)} \\ & -\sqrt{3}M \int_{-\infty}^{\infty} \frac{d\theta}{2\pi} \cosh(\theta) e^{-\sqrt{3}MR \cosh(\theta)} + \mathcal{O}(e^{-2MR}), \end{aligned} \quad (1.52)$$

and essentially marks the correction to the energy due to the spontaneous emission of a virtual particle from the vacuum which travels around the system before being reabsorbed. Fig. 1.4 shows the TCSA data against the theoretical values of E_{gs} (including the full, not just the leading order large R , contribution coming from $E_{TBA}(R)$). There is a good agreement for R smaller than $mR = 8$ and then slight deviations thereafter, which can be reduced by increasing the value of N_{tr} (see Fig. 1.4).

Above the single particle states, one encounters sets of two-particle states consisting of pairs of particles from the triplet and the singlet of the SG model. These two-particle

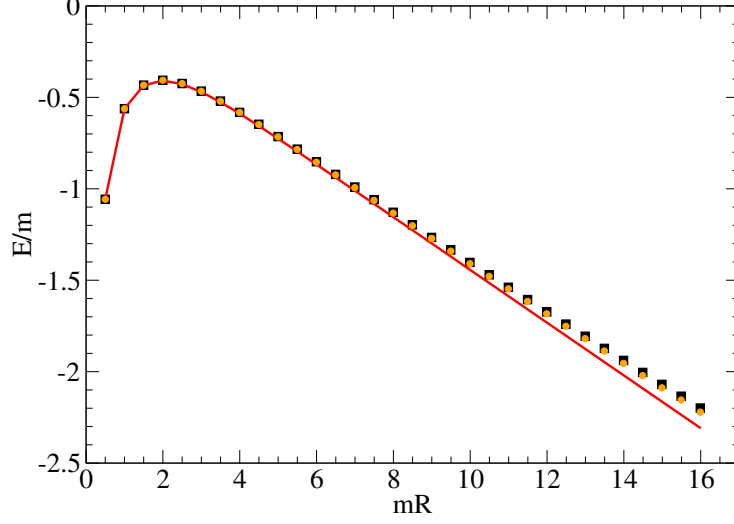


Figure 1.4: Ground state energy: analytic prediction (continuous line) compared to the TCSA results. Black squares: TCSA with $N_{\text{tr}} = 9$; orange circles: TCSA with $N_{\text{tr}} = 10$.

states can be organized into $SU(2)$ multiplets. For example, two-particle states involving the triplet decompose as $(\mathbf{3} \otimes \mathbf{3}) = (\mathbf{5} \oplus \mathbf{3} \oplus \mathbf{1})$. These states suffer finite size corrections due to scattering between the particles. These effects can be taken into account by solving the quantization conditions for the momentum in finite volume:

$$2\pi n_i = mR \sinh \theta_i - i \ln S_{ij}(\theta_i - \theta_j), \quad i = 1, 2, \quad (1.53)$$

where θ_i ($i = 1, 2$) are the rapidities of the particles that parametrize their energy-momentum, $(E, p) = (m \cosh \theta_i, m \sinh \theta_i)$, and S_{ij} is the scattering matrix between the two particles [81]. The solution of these equations, for a pair (n_1, n_2) , yields the rapidities as a function of R , and so the energy of these states. Fig. 1.5 shows reasonably good agreement between the analytical and the TCSA results, particularly at large values of R . At smaller R , single particle virtual processes become important, leading to deviations between the TCSA and our analytic estimates.

1.4 $SU(2)_1$ perturbed by current-current interactions

In this section we consider the perturbation of the $SU(2)_1$ WZW model by the marginal current-current operator,

$$H = H_{SU(2)_1} - g \int dx \bar{J}_L(x) \cdot \bar{J}_R(x). \quad (1.54)$$

Unlike the perturbation by the spin-1/2 field, here the sign of g matters as it differentiates the model's behavior in the IR limit [78]. For $g > 0$ the perturbation is marginally relevant and asymptotically free. The corresponding theory is a massive integrable rational

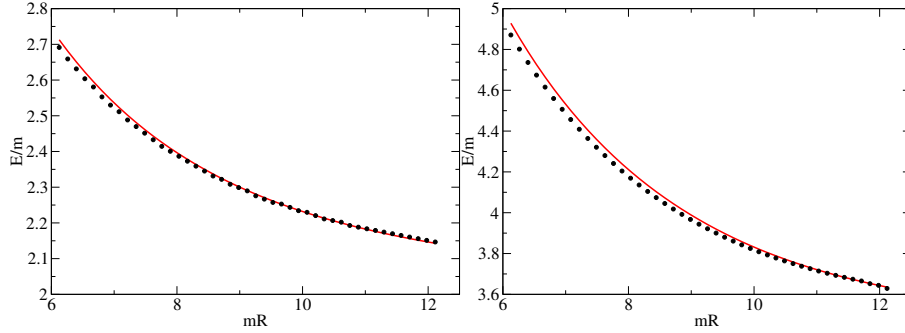


Figure 1.5: Two-particle states: comparison between the analytic results and the TCSA data. Left panel: a two particle state involving two triplet particles with total $S_z = 0$ and $(n_1, n_2) = (-1, 1)$. Right panel: a two-breather B_2 state with $(n_1, n_2) = (-1, 1)$. Continuous line: analytical results derived from Eq. (1.53). Dots: TCSA data.

field theory (RFT) coinciding with the $SU(2)$ Thirring model [82]. And for $g < 0$ the coupling is marginally irrelevant and the theory undergoes a massless RG flow towards the $SU(2)_1$ fixed point.

We address two questions here. We first ask if we can determine with the TCSA the universal correction (as explained below) to the ground state energy due to the marginal perturbation. And second, we question if the numerical renormalization group improvement of the TCSA works in the context of marginal perturbations [61, 62, 63, 64, 65].

1.4.1 Universal Term in Ground State Energy from the TCSA

In the small g regime, the correction to the ground state energy on the cylinder is given in perturbation theory by [83]:

$$E_0 = -\frac{\pi}{6R}c - \frac{g^2}{2!}R \left(\frac{2\pi}{R}\right)^{2x-2} \frac{3}{4}I_2 - \frac{g^3}{3!}bR \left(\frac{2\pi}{R}\right)^{3x-4} I_3, \quad (1.55)$$

where

$$I_2 = \int d^2z |z|^{x-2} |z-1|^{-2x};$$

$$I_3 = \int d^2z_1 d^2z_2 |z_1|^{x-2} |z_2|^{x-2} |z_1-1|^{-x} |z_2-1|^{-x} |z_1-z_2|^{-x}. \quad (1.56)$$

We write these expressions so that they are valid for a general dimension, x , of the perturbing operator, $\phi(= \bar{J}_L \cdot \bar{J}_R$ for $x = 2$). Our conventions are such that two point function (on the plane) is

$$\langle \phi(r)\phi(0) \rangle = \frac{3}{4} \frac{1}{|r|^{2x}},$$

The normalization can be fixed by the flowing quick argument. The operator is explicitly expressed as

$$\phi = J_L^0 J_R^0 + \frac{1}{2} J_L^+ J_R^- + \frac{1}{2} J_L^- J_R^+ \quad (1.57)$$

and thus for the two point function we formally have

$$\left\langle \left[J_L^0 J_R^0 + \frac{1}{2} J_L^+ J_R^- + \frac{1}{2} J_L^- J_R^+ \right] \left[J_L^0 J_R^0 + \frac{1}{2} J_L^+ J_R^- + \frac{1}{2} J_L^- J_R^+ \right] \right\rangle$$

and just

$$\langle J_L^0 J_R^0 J_L^0 J_R^0 \rangle + \frac{1}{4} \langle J_L^+ J_R^- J_L^- J_R^+ \rangle + \frac{1}{4} \langle J_L^- J_R^+ J_L^+ J_R^- \rangle$$

are different from zero. Using the OPE between current-operators the result is

$$\frac{1}{4} + \frac{1}{4} + \frac{1}{4} = \frac{3}{4}.$$

The corresponding three point function equals

$$\langle \phi(r_1) \phi(r_2) \phi(r_3) \rangle = \frac{b}{|r_{12}|^x |r_{13}|^x |r_{23}|^x}, \quad (1.58)$$

with $b = 3/2$. Indeed, as for the two point function, the three point function can be expressed in term of the non-zero terms

$$\frac{1}{4} \langle J_J^0 J_R^0 J_L^+ J_R^- J_L^- J_R^+ \rangle + \frac{1}{4} \langle J_J^0 J_R^0 J_L^- J_R^+ J_L^+ J_R^- \rangle,$$

plus other two similar terms which differ just for the position of $J_L^0 J_R^0$. Summing all these three equal contributions the result is:

$$3 \left(\frac{1}{4} + \frac{1}{4} \right) = \frac{3}{2}.$$

The β -function for this theory, within our conventions, is given by

$$\frac{d\tilde{g}}{dl} = (2 - x)\tilde{g} + \frac{4\pi b}{3\Gamma^2(x/2)}\tilde{g}^2. \quad (1.59)$$

where \tilde{g} is then the dimensionless coupling and l is a logarithmic length scale. To convert to the conventions of Refs. [83, 84], we need to take $\phi \rightarrow -\sqrt{\frac{4}{3}}\phi$.

Although the theory is defined on a cylinder, under a conformal transformation the integrals I_2 and I_3 can be written as integrals over the plane, as given above in Eq. (1.56). It is evident from expressions (1.56) that they are UV divergent and require regulation. The divergent pieces of these integrals contribute to the non-universal piece of E_0 (non-universal because their value depends on the regulation scheme). If ϵ_p is a short

distance regulator in the plane (i.e. the difference of two plane integration variables is not permitted to be smaller than ϵ_p), both I_2 and I_3 contain terms proportional to ϵ_p^{-2} (for $x = 2$). Under a conformal transformation, ϵ_p is related to a short distance regulator on the cylinder, ϵ_c , by $\epsilon_p = 2\pi\epsilon_c/R$. Thus the divergent pieces lead non-universal correction of the form

$$E_{0,non-univ} = (a_2 g^2 + a_3 g^3 + \dots) \frac{R}{\epsilon_c^{2x-2}}, \quad (1.60)$$

i.e. these corrections scale linearly with the system size.

On the other hand, the universal corrections coming from I_2 and I_3 are independent of the details of the regulator. Such corrections are usually accessed through analytic continuation in the operator dimension x . For sufficiently small x , the resulting perturbative integrals become convergent. For such a range of x , one then introduces a regulator, ϵ_p , and expands in a Taylor series, finding that I_2 and I_3 have the form [83, 84]:

$$\begin{aligned} I_2(x, \epsilon_p) &= c_2 \epsilon_p^{2(2-x)-2} + I_{2,univ.}(x) + \mathcal{O}(\epsilon_p^{6-2x}); \\ I_3(x, \epsilon_p) &= c_3 \epsilon_p^{3(2-x)-2} + I_{3,univ.}(x) + \epsilon_p^{2-x} I_{3,subleading}(x) + \mathcal{O}(\epsilon_p^{6-2x}); \\ I_{3,subleading}(x) &= -6\pi \frac{\epsilon_p^{2-x}}{2-x} I_{2,univ.}(x). \end{aligned} \quad (1.61)$$

Because everything is convergent, expressions can be obtained for $I_{2,univ.}(x)$ and $I_{3,univ.}(x)$ as a function of x . The universal terms' values close to $x = 2$ are then the analytically continued parts of the expansion of I_2 and I_3 that are independent of the UV regulator (the non-universal terms, in contrast, in general either diverge or vanish close to $x = 2$). The relationship between $I_{3,subleading}(x)$ and $I_{2,univ.}(x)$ arises from the OPE, $\phi\phi \sim b\phi$ [84].

In the case at hand, the universal contributions near $x = 2$ are [83, 84]

$$\begin{aligned} I_{2,univ.}(x \sim 2) &= -\frac{\pi}{4}(2-x); \\ I_{3,univ.}(x \sim 2) &= -2\pi^2; \\ I_{3,subleading}(x \sim 2) &= \frac{3\pi^2}{2}. \end{aligned} \quad (1.62)$$

We also include the evaluation of $I_{3,subleading}(x)$ because exactly at $x = 2$ the prefactor of this term becomes independent of ϵ_p . Its evaluation, with important consequences, will turn out to depend upon the choice of the regulator.

The universal and subleading parts of I_2 and I_3 allows us to write the universal part of E_0 solely as a function of the running coupling $\tilde{g}(l)$ [84]. $E_{0,univ}$ in terms of the bare

dimensionless coupling, $\tilde{g} = g\epsilon_c^{2-x}$, is equal to

$$c(\tilde{g}) \equiv -\frac{6R}{\pi}E_{0,univ} = c + (24\pi)\left(\frac{3}{8}(\epsilon_p^{-y}\tilde{g})^2I_{2,univ} + \frac{b}{6}(\epsilon_p^{-y}\tilde{g})^3I_{3,univ}\right). \quad (1.63)$$

Supposing $y \equiv (2-x) > 0$, we can use the β -function to express \tilde{g} in terms of $\tilde{g}(l)$:

$$\tilde{g} = \frac{\tilde{g}(l)\epsilon_p^y}{1 - \frac{\tilde{g}(l)}{\tilde{g}^*}(1 - \epsilon_p^y)}, \quad (1.64)$$

where $\tilde{g}^* = \frac{4\pi b}{3(2-x)} + \mathcal{O}(2-x)$ is the zero of the β -function. We then have

$$c(\tilde{g}(l)) = c + 24\pi\left(-\frac{3}{4}\frac{\pi(2-x)}{8}\tilde{g}^2(l) - \tilde{g}^3(l)\left(\frac{b\pi^2}{12} + \mathcal{O}(2-x)\right) + \mathcal{O}(\tilde{g}^4(l))\right). \quad (1.65)$$

$c(\tilde{g}(l))$ is nothing more than Zamolodchikov's c-function [85]. We see that $\partial_{\tilde{g}(l)}c(\tilde{g}(l))$ has the same zero, \tilde{g}^* , as the β -function, as it should. We also see that exactly at the marginal point, $x = 2$, there is a finite third order correction in $\tilde{g}(l)$ to the ground state energy.

An interesting question is what of this universal behavior can be extracted from the TCSA. While it has been suggested in Ref. [55] that the dependency of the TCSA data upon the UV regulator (here, the truncation level, N_{tr}) obscures such terms, it has been shown in Ref. [86] that upon the subtraction of leading and sub-leading order divergences, universal IR behavior can be observed.

In order to determine the nature of the universal behaviour in the TCSA approach, we need to compute the integrals I_2 and I_3 with the TCSA regulator in place. This however can be straightforwardly done [86]. The essential idea is that these integrals can be expanded in powers of the integration variables. These expansions can be then compared with a Lehmann expansion of the corresponding n -point function.

By truncating the Lehmann expansion to the same low energy states used in the TCSA, we learn how to truncated the expansions for $I_{2,3}$, and we are able to compute them with the TCSA regulator. The resulting integrals, precisely at the marginal point $x = 2$, are surprisingly simple and can be computed exactly to be:

$$\begin{aligned} I_2^{TCSA} &= \pi N_{tr}(N_{tr} + 1); \\ I_3^{TCSA} &= 3\pi^2 N_{tr}(N_{tr} + 1). \end{aligned} \quad (1.66)$$

We now carry on this strategy: first we force the UV regularization of the TCSA in the Lehmann representation of the n -point functions, then we expand the integrals (1.61) at $x = 2$ in powers of the integration variables. We then truncate these expansions by comparing with the regularized Lehmann representations; at this stage the integrals can

be performed with the TCSA regulator implemented [88, 86].

We compute first the integral I_2 , coming from the **two point function**. By introducing operators $\mathcal{P}_{N_{\text{tr}}}$ and $\bar{\mathcal{P}}_{N_{\text{tr}}}$ that project out all chiral states of level higher than N_{tr} , we can write the two point function appearing in the evaluation of the second order perturbative contribution to the ground state energy as

$$\langle \mathcal{T} \phi(x, t) \phi(0, 0) \rangle = \langle \mathcal{T} \mathcal{P}_{N_{\text{tr}}} \bar{\mathcal{P}}_{N_{\text{tr}}} \phi(x, t) \mathcal{P}_{N_{\text{tr}}} \bar{\mathcal{P}}_{N_{\text{tr}}} \phi(0, 0) \mathcal{P}_{N_{\text{tr}}} \bar{\mathcal{P}}_{N_{\text{tr}}} \rangle, \quad (1.67)$$

where \mathcal{T} is the usual time ordering operator. These projectors truncate the Lehmann expansion, computed with the insertion of a resolution of the identity between the operators of (1.67):

$$\sum_{0 \leq m, \bar{m} \leq N_{\text{tr}}} \langle 0 | \phi(0, 0) | m \rangle \otimes | \bar{m} \rangle \langle m | \otimes \langle \bar{m} | \phi(x, t) | 0 \rangle. \quad (1.68)$$

Here the sum is limited to all states whose conformal level is less than N_{tr} . Furthermore, we just considered the contribution with $t < 0$ coming from the time ordering (also the contribution $t > 0$ must be considered). Using the time and space translation operator, $e^{-Ht - iPx}$, and defining $z = e^{\frac{2\pi}{R}(ix+t)}$ and $\bar{z} = e^{\frac{2\pi}{R}(-ix+t)}$, we can rewrite the above expression as

$$\sum_{0 \leq m, \bar{m} \leq N_{\text{tr}}} \langle 0 | \phi(0, 0) (| m \rangle \otimes | \bar{m} \rangle \langle m | \otimes \langle \bar{m} |) \phi(0, 0) | 0 \rangle z^m \bar{z}^{\bar{m}}. \quad (1.69)$$

The correlation function is reduced to a truncated sum on powers in z and \bar{z} .

We want now to expand the integral, I_2^{TCSA} , in order to make it comparable with (1.69). Transforming the integral in I_2 back to the cylinder we obtain,

$$I_2^{TCSA} = 2 \cdot \left(\frac{2\pi}{R} \right)^2 \int_0^R dx \int_{-\infty}^0 dt \frac{z}{(z-1)^2} \frac{\bar{z}}{(\bar{z}-1)^2}, \quad (1.70)$$

where the factor of two counts the two contributions coming from time ordering. If we then expand the integrand as a power series in z, \bar{z}

$$I_2 = 2 \cdot \left(\frac{2\pi}{R} \right)^2 \int_0^R dx \int_{-\infty}^0 dt \sum_{n=0}^{\infty} n z^n \sum_{m=0}^{\infty} m \bar{z}^m, \quad (1.71)$$

The comparison with Eq. (1.69), indicates to truncate the sums as follows

$$I_2 = 2 \cdot \left(\frac{2\pi}{R} \right)^2 \int_0^R dx \int_{-\infty}^0 dt \sum_{n=0}^{N_{\text{tr}}} n z^n \sum_{m=0}^{N_{\text{tr}}} m \bar{z}^m. \quad (1.72)$$

The integral has now implemented the TCSA regulator expressed by projectors of Eq. (1.67) and sums are now easily computed:

$$I_2 = \pi N_{\text{tr}} (N_{\text{tr}} + 1). \quad (1.73)$$

Comparing with the evaluation in [83, 84], we see that we obtain a relationship between the TCSA regulator and the short distance cutoff, ϵ_p , used in [83, 84]:

$$\epsilon_p = \frac{1}{\sqrt{N_{\text{tr}}(N_{\text{tr}} + 1)}}. \quad (1.74)$$

The third order correction is determined by the **three point function** which can be computed following the same strategy. We implement the TCSA regulator by inserting the projectors

$$\langle \mathcal{T} \mathcal{P}_{N_{\text{tr}}} \bar{\mathcal{P}}_{N_{\text{tr}}} \phi(x, t) \mathcal{P}_{N_{\text{tr}}} \bar{\mathcal{P}}_{N_{\text{tr}}} \phi(0, 0) \mathcal{P}_{N_{\text{tr}}} \bar{\mathcal{P}}_{N_{\text{tr}}} \phi(x', t') \mathcal{P}_{N_{\text{tr}}} \bar{\mathcal{P}}_{N_{\text{tr}}} \rangle, \quad (1.75)$$

resulting, in the case where $t' < 0 < t$ (similarly other contributions from the time-ordering must be accounted), to

$$\sum_{0 \leq m, \bar{m}, n, \bar{n} \leq N_{\text{tr}}} \langle 0 | \phi(x, t) | m \rangle \otimes | \bar{m} \rangle \langle m | \otimes \langle \bar{m} | \phi(0, 0) | n \rangle \otimes | \bar{n} \rangle \langle n | \otimes \langle \bar{n} | \phi(x', t') | 0 \rangle. \quad (1.76)$$

Again, space time translation operators are applied and, keeping the notation $d z = e^{\frac{2\pi}{R}(ix+t)}$, $\bar{z} = e^{\frac{2\pi}{R}(-ix+t)}$, $w = e^{\frac{2\pi}{R}(ix'+t')}$, and $\bar{w} = e^{\frac{2\pi}{R}(-ix'+t')}$, we obtain

$$\sum_{0 \leq m, \bar{m}, n, \bar{n} \leq N_{\text{tr}}} \langle 0 | \phi(0, 0) | m \rangle \otimes | \bar{m} \rangle \langle m | \otimes \langle \bar{m} | \phi(0, 0) | n \rangle \otimes | \bar{n} \rangle \langle n | \otimes \langle \bar{n} | \phi(0, 0) | 0 \rangle z^{-m} \bar{z}^{-\bar{m}} w^n \bar{w}^{\bar{n}}, \quad (1.77)$$

that is a polynomial truncated at order N_{tr} in z, \bar{z}, w, \bar{w} . The expression (1.77) must be compared with the expansion of I_3 in Eq. (1.56) on the cylinder, to understand how to truncate it in order to reproduce the regularization of the TCSA.

The computation of I_3^{TCSA} is just slightly more complicated. The integral reads:

$$I_3^{TCSA} = \int dz d\bar{z} dw d\bar{w} \frac{1}{(z - w)(\bar{z} - \bar{w})(z - 1)(w - 1)(\bar{z} - 1)(\bar{w} - 1)}. \quad (1.78)$$

Mapping to the cylinder, the time ordering gives 6 contributions, $t < t' < 0$, $t > t' > 0$, $t < 0 < t'$ and those with $t \leftrightarrow t'$, all being equal. We show, as an example, the integral for $t > 0 > t'$:

$$\left(\frac{2\pi}{R}\right)^4 \int_0^R dx \int_0^R dx' \int_0^\infty dt \int_{-\infty}^0 dt' \frac{z \bar{z} w \bar{w}}{(z - w)(\bar{z} - \bar{w})(z - 1)(w - 1)(\bar{z} - 1)(\bar{w} - 1)}, \quad (1.79)$$

where $z = e^{\frac{2\pi}{R}(ix+t)}$, $\bar{z} = e^{\frac{2\pi}{R}(-ix+t)}$, $w = e^{\frac{2\pi}{R}(ix'+t')}$, and $\bar{w} = e^{\frac{2\pi}{R}(-ix'+t')}$. We compute its contribution by expanding the above in a power series of z, \bar{z}, w, \bar{w} and truncating it at

the N_{tr} -th power. Matching the truncation in the Lehmann expansion of Eq. (1.77), the integrand in (1.79) becomes

$$\frac{|z|^2|w|^2}{|z-w|^2|z-1|^2|w-1|^2} = \frac{1}{|1-w/z|^2} \frac{1}{|1-1/z|^2} \frac{1}{|1-w|^2} \frac{|w|^2}{|z|^2} \quad (1.80)$$

$$\begin{aligned} &= \sum_{j,k,\bar{j},\bar{k},\bar{l} \in C} \left(\frac{z}{w}\right)^{j+1} \left(\frac{\bar{z}}{\bar{w}}\right)^{\bar{j}+1} z^{-k} \bar{z}^{-\bar{k}} w^l \bar{w}^{\bar{l}} \\ &= \sum_{j,k,\bar{j},\bar{k},\bar{l} \in C} w^{j+l+1} \bar{w}^{\bar{j}+\bar{l}+1} z^{-k-j-1} \bar{z}^{-\bar{k}-\bar{j}-1}, \end{aligned} \quad (1.81)$$

where C is defined by

$$\begin{aligned} 1 &\leq j+l+1 \leq N_{\text{tr}}; \\ 1 &\leq j+k+1 \leq N_{\text{tr}}; \\ 1 &\leq \bar{j}+\bar{l}+1 \leq N_{\text{tr}}; \\ 1 &\leq \bar{j}+\bar{k}+1 \leq N_{\text{tr}}. \end{aligned} \quad (1.82)$$

and all the indexes are positive or zero. The integrals can now be computed and the summations evaluated to be

$$\pi^2 \sum_C \frac{1}{(j+l+1)(j+k+1)} = \pi^2 \frac{N_{\text{tr}}(N_{\text{tr}}+1)}{2}. \quad (1.83)$$

Once combined with the other five equal contributions, we obtain the final result:

$$I_3^{TCSA} = 3\pi^2 N_{\text{tr}}(N_{\text{tr}}+1), \quad (1.84)$$

and we obtained (1.66).

The expressions (1.66) contain both non-universal terms (as it is evident from the dependency on N_{tr}) and potential universal terms. The question becomes how to identify which is which. We do so by comparison with the evaluation of I_2 and I_3 in Refs. [83, 84] already given in Eq.(1.62). At $x = 2$, $I_2(x = 0)$ is purely non-universal, i.e. $I_{2,\text{univ.}}(x = 2) = 0$. This corresponds to our finding that I_2 is proportional to $N_{\text{tr}}(N_{\text{tr}}+1)$ and indicates that the regulator, ϵ_p , used in Ref. [83, 84] can be identified with the TCSA regulator via $\epsilon_p^{-2} \propto N_{\text{tr}}(N_{\text{tr}}+1)$. However I_3^{TCSA} is also proportional to $N_{\text{tr}}(N_{\text{tr}}+1)$, which seems to imply that the third order contribution to E_{gs} , as with second order, is purely non-universal. We see then already at $x = 2$ that the TCSA regulator leads to a different universal structure to $E_{0,\text{univ}}$ than the Lorentz invariant regulator employed in [83, 84].

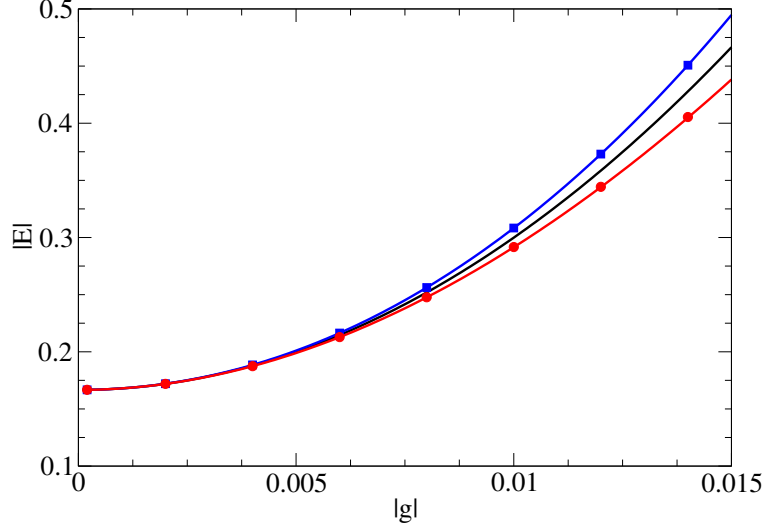


Figure 1.6: Plots of the ground state energy of $SU(2)_1 + \bar{J}_L \cdot \bar{J}_R$ as a function of the marginal coupling g . Solid lines give the perturbative computation for both $g > 0$ relevant (blue) and $g < 0$ irrelevant (red). The black line shows the second order perturbative correction in g . The data points represent the corresponding numerical data from the TCSA.

We verify the accuracy of this perturbative computation by comparing it with the TCSA numerics. In Fig.1.6 we plot E_0 at small g evaluated numerically against the perturbative results. We obtain excellent agreement. To analyze more closely the possible presence of a universal term in the numerics, we plot in Fig. 1.7 the residual ground state energy arrived at by subtracting from the numerical data the perturbative contributions (solely non-universal) corresponding to $I_2^{TCSA} + I_3^{TCSA}$. To determine whether the numerics indicate any universal contribution, we plot the residual as a function of g and fit the results to a function of the form $g^3(a + gbN_{\text{tr}}(N_{\text{tr}} + 1))$ (see Fig. 1.7). These fits put an approximate bound (the value of a) on the third order universal term consistent with the numerics. We find it to be considerably smaller than that found in Ref. [83, 84], consistent with our previous statement that in the regulation scheme used by the TCSA, there is no universal term at third order in the coupling.

To get at the origin of the discrepancy between the TCSA evaluation of $E_{0,\text{univ}}$ and that of Refs. [83, 84], we evaluate the integrals, I_2 and I_3 in the TCSA regulation scheme away from the marginal point. These integrals have the structure (compare with Eq. (1.61))

$$I_2^{TCSA}(x, N_{\text{tr}}) = I_{2,\text{div.}}^{TCSA}(x)(N_{\text{tr}}(N_{\text{tr}} + x - 1))^{x-1} + I_{2,\text{univ.}}^{TCSA}(x) + I_{2,\text{subleading}}^{TCSA}N_{\text{tr}}^{2x-6};$$

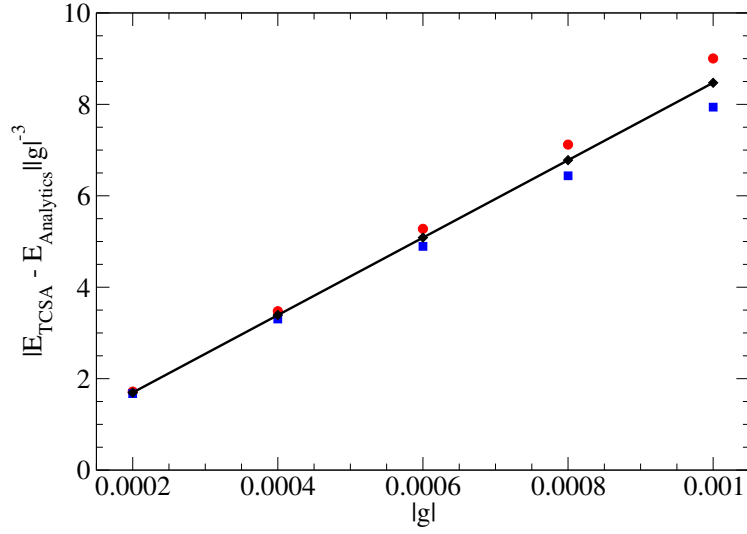


Figure 1.7: Plots of the residual ground state energy (the TCSA data with the perturbative contributions, I_2^{TCSA} and I_3^{TCSA} , subtracted off) as a function of g for $N_{tr} = 9$ (red: irrelevant g ; blue: relevant g). The average of the two results (black curve) is fitted with the function, $g^3(a + gbN_{tr}(N_{tr} + 1))$ (this average removes lower order logs that might appear from resumming high order contributions). The fitting parameters are $a = 0.002 \pm 0.001$ and $b = 94.12 \pm 0.02$.

$$I_3^{TCSA}(x, N_{tr}) = I_{3,div.}^{TCSA}(x)(N_{tr}(N_{tr} + x - 1))^{x-1} + I_{3,univ.}^{TCSA}(x) + I_{3,subleading}^{TCSA}N_{tr}^{2x-4}. \quad (1.85)$$

Let us start deriving the above expression for I_2 for generic x , and computing the coefficients of the divergent, universal and subleading terms. Once transformed back onto the cylinder, the integral reads

$$I_2^{TCSA}(x) = 2 \cdot \left(\frac{2\pi}{R}\right)^2 \int_0^R dx \int_{-\infty}^0 dt \frac{|z|^x}{|z - 1|^{2x}}. \quad (1.86)$$

Expanding the integrands in powers of z and \bar{z} , truncating with level N_{tr} , and performing the integrals leaves us with (compare Eq. (1.72))

$$\begin{aligned} I_2^{TCSA}(x) &= 2\pi \sum_{n=0}^{N_{tr}-1} \frac{\Gamma^2(n+x)}{(n+\frac{x}{2})\Gamma^2(x)(n!)^2} \\ &\equiv I_{2,div.}^{TCSA}(x)(N_{tr}(N_{tr} + x - 1))^{x-1} + I_{2,univ.}^{TCSA}(x) + I_{2,subleading}^{TCSA}(x)N_{tr}^{2x-6}. \end{aligned} \quad (1.87)$$

The coefficient of the **leading term** in the above can be determined from the Euler-Maclaurin formula converting a sum to an integral in combination with our exact result at $x = 2$. The result is

$$I_{2,div.}^{TCSA}(x) = \frac{2\pi}{\Gamma^2(x)(2x-2)}. \quad (1.88)$$

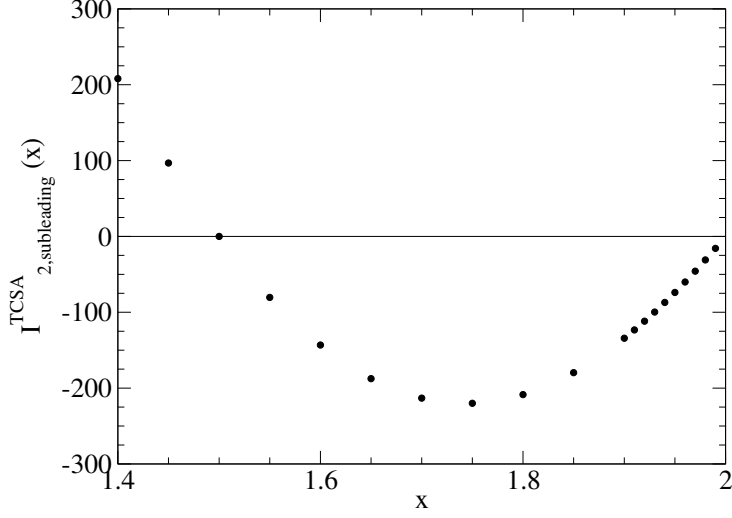


Figure 1.8: Plot of $I_{2,subleading}^{TCSA}(x)$ as a function of x .

The **universal coefficient**, $I_{2,univ.}^{TCSA}$, can be determined from performing the integral in Eq. (1.86) for $0 < x < 1$ and then analytically continuing [83]:

$$I_{2,univ.}^{TCSA}(x) = \frac{\pi \Gamma^2(\frac{x}{2}) \Gamma(1-x)}{\Gamma^2(1-\frac{x}{2}) \Gamma(x)}. \quad (1.89)$$

Finally we determine the coefficient of the **subleading term**, $I_{2,subleading}^{TCSA}(x)$, numerically: we compute the sum in Eq. (1.87) numerically as a function of N_{tr} , subtract the first two terms in the second line of Eq. (1.87), and fit what remains to extract the coefficient of N_{tr}^{2x-6} . The results are plotted in Fig. (1.8). We note in particular that as $x \rightarrow 2$, $I_{2,subleading}^{TCSA}(x) \rightarrow 0$.

The computation for $I_3^{TCSA}(x)$ is now much less trivial. It is done by first representing $I_3(x)$ as an integral over the cylinder:

$$I_3(x) = \left(\frac{2\pi}{4}\right)^4 \int_0^R dx_1 dx_2 \int_{-\infty}^{\infty} dt_1 dt_2 \frac{|z_1|^x |z_2|^x}{|z_1 - z_2|^x |z_1 - 1|^x |z_2 - 1|^x}, \quad (1.90)$$

where $z_i = e^{2\pi(ix_i + t_i)/R}$. Expanding the integrand in powers of z_i , performing the integrals, and truncating the remaining summations on the basis of a comparison with the Lehmann expansion leaves us with

$$\begin{aligned} I_3^{TCSA}(x) &= 12\pi^2 \sum_{j=0}^{N_{tr}-1} \sum_{\bar{j}=0}^j \sum_{l=0}^{N_{tr}-j-1} \sum_{k=0}^{N_{tr}-j-1} \frac{\gamma_j \gamma_{\bar{j}} \gamma_l \gamma_{j+l-\bar{j}} \gamma_k \gamma_{k+j-\bar{j}}}{(j+l+\frac{x}{2})(j+k+\frac{x}{2})}, \\ \gamma_j &= \frac{\Gamma(j+\frac{x}{2})}{\Gamma(\frac{x}{2})\Gamma(j+1)}. \end{aligned} \quad (1.91)$$

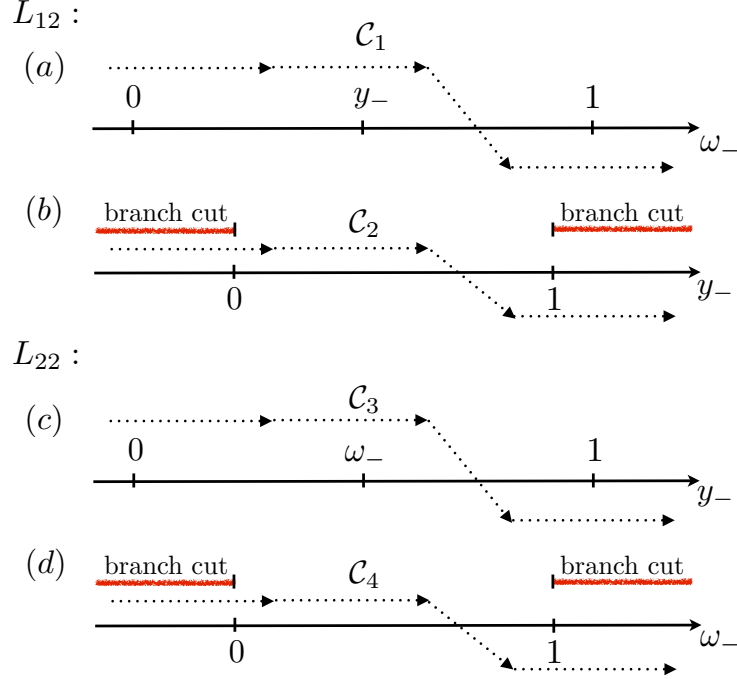


Figure 1.9: Definition of contours used in evaluating $I_3^{TCSA}(x)$. There are branch points at all labelled points: $0, 1, y_-$, and w_- . The red lines mark additional branch cuts with branch points at 0 and 1 that result from integrating w_- in the case of L_{12} and y_- in the case of L_{22} .

$I_3^{TCSA}(x)$ then has a similar structure to $I_2^{TCSA}(x)$:

$$I_3^{TCSA}(x) = I_{3,div.}^{TCSA}(x)(N_{tr}(N_{tr} + x - 1))^{x-1} + I_{3,univ.}^{TCSA}(x) + I_{3,subleading}^{TCSA}(x)N_{tr}^{x-2}. \quad (1.92)$$

We infer that the leading term of $I_3^{TCSA}(x)$ must be proportional to $(N_{tr}(N_{tr} + x - 1))^{x-1}$ – otherwise the relationship between the TCSA cutoff, N_{tr} , and ϵ_p established in the evaluation of I_2 would breakdown. (We will in any case verify this numerically in what is to come.)

The coefficient of the **leading term** can be found by converting the sums to integrals:

$$I_{3,div.}^{TCSA}(x) = \frac{12\pi^2}{\Gamma^6(\frac{x}{2})} \int_0^1 dj \int_0^j d\bar{j} \int_0^{1-j} dl \int_0^{1-j} dk \frac{(j\bar{j}lk(l+j-\bar{j})(k+j-\bar{j}))^{\frac{x}{2}-1}}{(j+l)(k+l)}. \quad (1.93)$$

We can also evaluate analytically the **universal coefficient** $I_{3,univ.}^{TCSA}(x)$. This can be computed by performing the integral in Eq. (1.56) for values of x where it is convergent and then analytically continuing. To make this evaluation we first perform the integration by parts suggested in Ref. [84]:

$$I_{3,univ.}^{TCSA}(x) = I_{3,univ.}(x) = \frac{2-x}{4-3x} \int d^2 z_1 d^2 z_2 \frac{|z_1+1|^{x-2}|z_2+1|^{x-2}}{|z_1-z_2|^x|z_1|^x|z_2|^x} \left(\frac{z_1}{1+z_1} + \frac{\bar{z}_1}{1+\bar{z}_1} \right). \quad (1.94)$$

We now evaluate this integral following the techniques introduced in Ref. [93] and used in Ref. [94]. Writing $z_i = x_i + iy_i$ and making the changes of variables:

$$y_i \rightarrow ie^{-i2\epsilon}y_i, \quad (1.95)$$

followed by

$$y_{\pm} = x_1 \pm y_1; \quad w_{\pm} = x_2 \pm y_2, \quad (1.96)$$

allows us to rewrite $I_3(x)$ as

$$\begin{aligned} I_3(x) &= \frac{2-x}{2(4-3x)} \int dy_+ (y_+ - 1 - i\epsilon\Delta_y)^{\frac{x}{2}-1} (y_+ - i\epsilon\Delta_y)^{-\frac{x}{2}} \\ &\times \int dw_+ (w_+ - y_+ - i\epsilon(\Delta_w - \Delta_y))^{-\frac{x}{2}} (w_+ - 1 - i\epsilon\Delta_w)^{\frac{x}{2}-1} (w_+ - i\epsilon\Delta_w)^{-\frac{x}{2}} \\ &\times \int dy_- (y_- - 1 + i\epsilon\Delta_y)^{\frac{x}{2}-2} (y_- + i\epsilon\Delta_y)^{-\frac{x}{2}+1} \\ &\times \int dw_- (w_- - y_- + i\epsilon(\Delta_w - \Delta_y))^{-\frac{x}{2}} (w_- - 1 + i\epsilon\Delta_w)^{\frac{x}{2}-1} (w_- + i\epsilon\Delta_w)^{-\frac{x}{2}}, \end{aligned} \quad (1.97)$$

where $\Delta_{w/y} = (w/y)_+ - (w/y)_-$. The positions of the contours for w_- and y_- relative to the various branch cuts of the arguments depend on the values of w_+ and y_+ . Only for certain values of w_+ and y_+ is it not possible to deform the contours w_-/y_- to infinity without encountering poles or branch cuts. This allows us to restrict the limits of w_+ and y_+ dramatically, simplifying the above integral to

$$\begin{aligned} I_3(x) &= \frac{2-x}{2(4-3x)} (L_1 + L_2); \\ L_1 &= -L_{11}L_{12}; \quad L_2 = -L_{21}L_{22}; \\ L_{11} &= \int_0^1 dw_+ \int_0^{w_+} dy_+ (1 - y_+)^{\frac{x}{2}-1} w_+^{-\frac{x}{2}} (w_+ - y_+)^{-\frac{x}{2}} (1 - w_+)^{\frac{x}{2}-1} y_+^{-\frac{x}{2}}; \\ L_{12} &= \int_{C_2} dy_- \int_{C_1} dw_- (1 - y_-)^{\frac{x}{2}-2} y_-^{-\frac{x}{2}+1} (w_- - y_-)^{-\frac{x}{2}} (1 - w_-)^{\frac{x}{2}-1} w_-^{-\frac{x}{2}}; \\ L_{21} &= \int_0^1 dy_+ \int_0^{y_+} dw_+ (1 - y_+)^{\frac{x}{2}-1} w_+^{-\frac{x}{2}} (y_+ - w_+)^{-\frac{x}{2}} (1 - w_+)^{\frac{x}{2}-1} y_+^{-\frac{x}{2}}; \\ L_{22} &= \int_{C_3} dy_- \int_{C_4} dw_- (1 - y_-)^{\frac{x}{2}-2} y_-^{-\frac{x}{2}+1} (y_- - w_-)^{-\frac{x}{2}} (1 - w_-)^{\frac{x}{2}-1} w_-^{-\frac{x}{2}}. \end{aligned} \quad (1.98)$$

The contours $C_i, i = 1, 2, 3, 4$ are defined in Fig. (1.9). These four separate integrals can now readily be expressed in terms of known functions ($B(x, y)$ is the Euler β -function and ${}_3F_2$ is a generalized hypergeometric function):

$$L_{11} = \frac{\sqrt{\pi}}{2^x \sin(\frac{\pi x}{2})} \frac{\Gamma(1 - \frac{x}{2})\Gamma(1 - \frac{3x}{4})\Gamma(\frac{3}{2} - \frac{x}{2})\Gamma(\frac{x}{4})\Gamma(\frac{x}{2})}{\Gamma(\frac{x}{2})\Gamma(2 - x)\Gamma^2(1 - \frac{x}{4})},$$

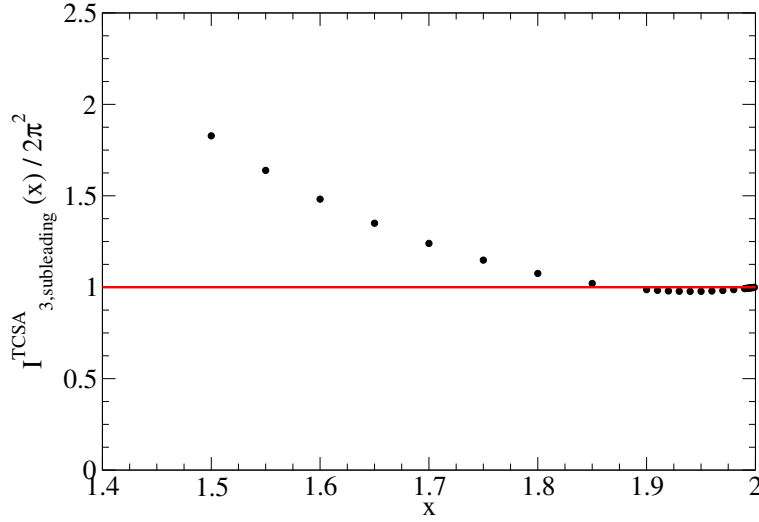


Figure 1.10: Plot of $I_{3,subleading}^{TCSA}(x)/(2\pi)^2$ as a function of x .

$$\begin{aligned}
 L_{12} &= -\frac{\pi(x-2)B(\frac{x}{2}, \frac{x}{2})}{2\sin(\frac{\pi x}{2})} {}_3F_2(2 - \frac{x}{2}, \frac{x}{2}, \frac{x}{2}, 2, x, 1); \\
 L_{21} &= L_{11}; \\
 L_{22} &= B(\frac{x}{2}, \frac{x}{2} - 1)\Gamma(\frac{x}{2})\Gamma(1 - \frac{x}{2}) {}_3F_2(\frac{x}{2}, \frac{x}{2} - 1, 1 - \frac{x}{2}, x - 1, 1, 1), \quad (1.99)
 \end{aligned}$$

Finally we can evaluate the coefficient of the **subleading term**, $I_{3,subleading}^{TCSA}(x)$, numerically. We compute this coefficient by evaluating the sum in Eq. (1.91) for a range of N_{tr} , subtracting off $I_{3,div.}^{TCSA}$ and $I_{3,univ.}^{TCSA}$. The remainder is proportional to N_{tr}^{x-2} and we extract $I_{3,subleading}^{TCSA}$ as the fitting coefficient. The results are found in Fig. 1.10. We see in particular that $I_{3,subleading}^{TCSA}(x) \rightarrow 2\pi^2$ as $x \rightarrow 2$.

The results we found for the x -dependent coefficients in (1.85) are thus summarized in:

$$\begin{aligned}
 I_{2,div.}^{TCSA}(x) &= \frac{2\pi}{\Gamma^2(x)(2x-2)}; \\
 I_{2,univ.}^{TCSA}(x) &= \frac{\pi\Gamma^2(\frac{x}{2})\Gamma(1-x)}{\Gamma^2(1-\frac{x}{2})\Gamma(x)}; \\
 I_{3,div.}^{TCSA}(x) &= \frac{12\pi^2}{\Gamma(\frac{x}{2})^6} \int_0^1 dj \int_0^j d\bar{j} \int_0^{1-j} dl \int_0^{1-j} dk \frac{(j\bar{j}kl(l+j-\bar{j})(k+j-\bar{j}))^{\frac{x}{2}-1}}{(j+l)(k+j)}; \\
 I_{3,univ.}^{TCSA}(x) &= -\frac{2-x}{4-3x} \frac{1}{2} (L_{11}L_{12} + L_{21}L_{22});
 \end{aligned}$$

$$\begin{aligned}
L_{11} &= \frac{\sqrt{\pi}}{2^x \sin(\frac{\pi x}{2})} \frac{\Gamma(1 - \frac{x}{2})\Gamma(1 - \frac{3x}{4})\Gamma(\frac{3}{2} - \frac{x}{2})\Gamma(\frac{x}{4})\Gamma(\frac{x}{2})}{\Gamma(\frac{x}{2})\Gamma(2 - x)\Gamma^2(1 - \frac{x}{4})}; \\
L_{12} &= -\frac{\pi(x-2)B(\frac{x}{2}, \frac{x}{2})}{2 \sin(\frac{\pi x}{2})} {}_3F_2(2 - \frac{x}{2}, \frac{x}{2}, \frac{x}{2}, 2, x, 1); \\
L_{21} &= L_{11}; \\
L_{22} &= B(\frac{x}{2}, \frac{x}{2} - 1)\Gamma(\frac{x}{2})\Gamma(1 - \frac{x}{2}) {}_3F_2(\frac{x}{2}, \frac{x}{2} - 1, 1 - \frac{x}{2}, x - 1, 1, 1), \quad (1.100)
\end{aligned}$$

and, as explained, we are only able to evaluate numerically the sub leading coefficient. Close to $x = 2$ we find

$$\begin{aligned}
I_{2,subleading}^{TCSA}(x=2) &= 0; \\
I_{3,subleading}^{TCSA}(x=2) &= 2\pi^2. \quad (1.101)
\end{aligned}$$

Now how does this compare to the results of [83, 84]? Remarkably the universal (constant) parts of I_2 and I_3 are the same (compare Eq. (1.61)):

$$\begin{aligned}
I_{2,univ.}^{TCSA}(x) &= I_{2,univ.}(x); \\
I_{3,univ.}^{TCSA}(x) &= I_{3,univ.}(x). \quad (1.102)
\end{aligned}$$

In particular

$$\begin{aligned}
I_{2,univ.}^{TCSA}(x \sim 2) &= -\frac{\pi}{4}(2 - x); \\
I_{3,univ.}^{TCSA}(x \sim 2) &= -2\pi^2. \quad (1.103)
\end{aligned}$$

We however see discrepancies in the subleading term, $I_{3,subleading}$:

$$I_{3,subleading}(x \sim 2) = \frac{3\pi^2}{2}; \quad I_{3,subleading}^{TCSA}(x \sim 2) = 2\pi^2. \quad (1.104)$$

This difference is a consequence of the TCSA's different (non-Lorentz invariant) regulator. It is possible to understand this difference as $I_{3,subleading}$ is finite at $x = 2$ due to a cancellation in a pole term due to an OPE and a zero in $I_{2,univ.}$. This delicate cancellation leaves $I_{3,subleading}$ sensitive to choice of regulator in a way that $I_{3,univ.}$ is not.

What are then the implications of $I_{3,subleading}(x)$ depending upon the regulator? Firstly we obtain an altered Zamolodchikov c-function:

$$c_{TCSA}(\tilde{g}(l)) = c + 24\pi \left(-\frac{3}{4} \frac{\pi(2-x)}{8} \tilde{g}^2(l) - \tilde{g}^3(l) \left(\frac{b\pi^2}{12} (1 - \epsilon_{TCSA}^{2-x}) \right) \right) \quad (1.105)$$

where $\epsilon_{TCSA} = N_{\text{tr}}^{-1}$. Interestingly the TCSA c -function agrees with that derived previously in Ref. ([84]) for $x < 2$ in the large N_{tr} (small ϵ_p) limit. However it is not solely a function of $\tilde{g}(l)$ as would be suggested by scaling theory.

As we have already noted, at $x = 2$ the $\tilde{g}^3(l)$ term vanishes in $c_{TCSA}(\tilde{g})$. This suggests that corrections that nominally contribute to the universal part of the ground state energy are sensitive to the use of a non-Lorentz invariant regulator. It turns out this may make it difficult to compare universal corrections computed in the setting of a Lorentz invariant field theory with universal corrections in models where Lorentz invariance is not present, i.e. lattice models. It would be interesting if this is the reason behind the suboptimal comparison for the specific heat of a spin-1/2 Heisenberg chain reported in Ref. [89] between the quantum transfer matrix solution of the lattice model and the corresponding Lorentz invariant field theoretic treatment of the spin chain [90] could be understood in this light. In this work uncomputed higher order corrections in $\tilde{g}(l)$ had to be employed as fitting parameters so as to obtain good agreement between the two treatments for the specific heat. We caution however that we do not claim that all universal quantities are regulator dependent. We ourselves have shown that $I_{3,\text{univ.}}(x)$ as evaluated both with the TCSA regulator and with the Lorentz invariant regulator agree. And Ref. [89] finds excellent agreement between the exact solution of the magnetic susceptibility of the lattice spin-1/2 chain and that of its Lorentz invariant field theoretic reduction.

1.4.2 NRG and Marginal Perturbations

In this subsection we apply the numerical renormalization group to the study of the marginal current-current perturbation of $SU(2)_1$. The NRG is a technique that allows the TCSA to include states at much higher conformal levels than would be possible with a straight exact diagonalization. It does so by taking a cue from Kenneth Wilson's NRG [13]: it takes into account the states that have a weaker influence on the low energy eigenstates of the full theory, in this case high energy conformal states, only in numerically manageable chunks. It works in the case of a relevant perturbation because such perturbations guarantee that the high energy conformal Hilbert space only affects weakly the low energy sector of the theory. Thus it is not clear, *a priori*, whether the NRG will work in the case of a marginal perturbation where the high and low energy sectors of the theory are more tightly coupled. We will, however, see that the NRG does work, reproducing with high accuracy the results of the TCSA run with a straight exact diagonalization.

Fig. 1.11 shows the RG evolution of the energies of the ground state, the first excited state, and the fifth excited state. The NRG results converge towards the exact diagonalization results with excellent accuracy. At least for the low lying energies in marginally

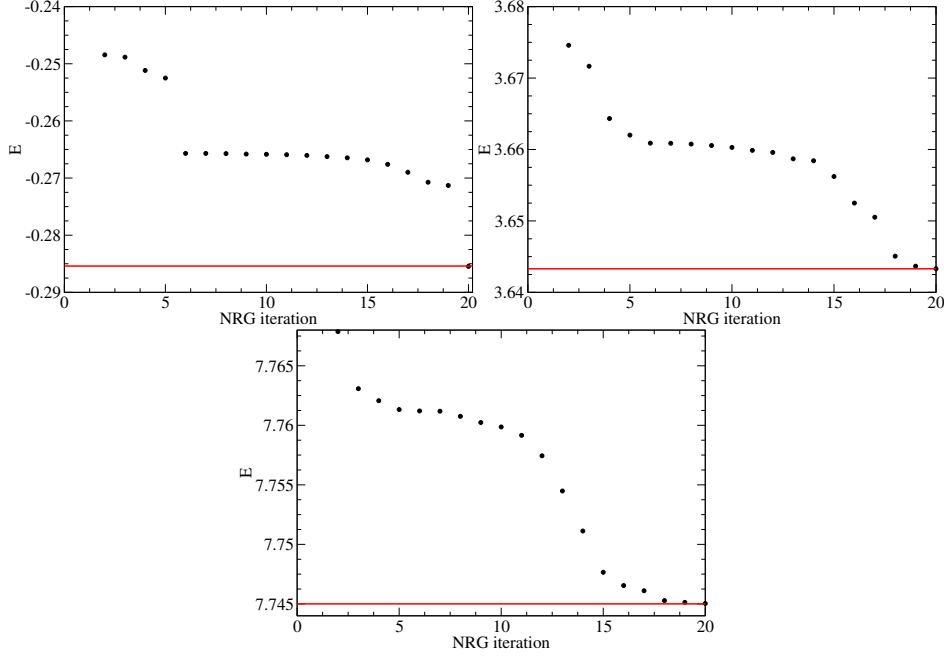


Figure 1.11: Plots of the ground state (left), the first excited state (center), and the fifth excited state (right) energies as a function of RG step. The energies of the last RG step correspond to taking into account all states up to a truncation of $N_{\text{tr}} = 11$. Here $g = 0.008$ is marginally irrelevant. The NRG base matrix size and step size (N and Δ in the notation of [62]) are $N = 4767$ and $\Delta = 500$. The total number of states in the Verma module of the Identity is 14767. The solid line is the TCSA result done with an exact diagonalization at level $N_{\text{tr}} = 11$.

perturbed conformal field theories, the NRG seems to be able to reproduce the expected energies, despite their dependencies upon the TCSA UV cutoff, N_{tr} .

1.5 $SU(2)_2$ perturbed by the spin-1 field

In this section we apply the TCSA to a deformation of the $SU(2)_2$ WZW model [22]. The $SU(2)_2$ WZW model is a $c = \frac{3}{2}$ conformal field theory with three primary fields, the spin-0 identity field, a spin $\frac{1}{2}$ field, $\phi_{1/2, \pm 1/2}$, and a spin 1 field, $\phi_{1, \{\pm 1, 0\}}$, with conformal weights $\Delta = 0$, $\Delta_{1/2} = \frac{3}{16}$, and $\Delta_1 = \frac{1}{2}$ respectively. A representation of the $SU(2)_2$ operator algebra cannot be given just in terms of vertex operators. Hence we defined also two auxiliary operators ψ and σ which satisfies the following fusion rules:

$$\begin{aligned} \psi \cdot \psi &\sim 1 \quad , \quad \sigma \cdot \sigma \sim 1 \\ \text{and } \psi \cdot \sigma &\sim \frac{1}{\sqrt{2}} \sigma \quad . \end{aligned} \tag{1.106}$$

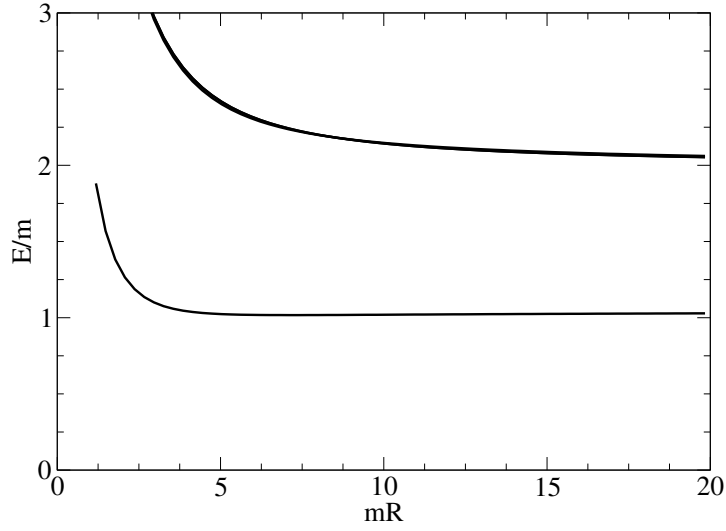


Figure 1.12: Plot of the energies of the four lowest excited states as a function of R in the sector $S_z = 0$. The ground state energy has been subtracted. The data are found for a truncation level $N_{\text{tr}} = 6$. There is a single low lying state with mass $M = 1.001$ and spin $S_z = 0$, which is a member of the fundamental triplet of particles. The higher energy level is three fold degenerate and corresponds to two-particle states.

The $SU(2)$ current operators can thus be defined as

$$\begin{aligned} J^0 &= i\partial\phi \\ J^\pm &= \sqrt{2}\psi : e^{\pm i\phi} :, \end{aligned} \quad (1.107)$$

and the algebra (1.31) for $k = 2$ can be recovered by just exploiting the OPEs as in (1.44). Similarly we can work out the commutators between currents and fields, which we defined to be

$$\begin{aligned} \phi_{1/2,\pm 1/2} &= \sigma : e^{\pm i\phi/2} : \\ \phi_{1,\pm 1} &=: e^{\pm i\phi} : \\ \phi_{1,0} &= \psi \end{aligned} \quad (1.108)$$

We here report some non trivial commutators to show the role of σ and ψ

$$\begin{aligned} [J^\pm, \phi_{1/2,\mp 1/2}] &\sim \sqrt{2}\psi e^{\pm i\phi} \cdot \sigma e^{\mp i\phi/2} \sim \sqrt{2}(\psi \cdot \sigma) (e^{\pm i\phi} \cdot e^{\mp i\phi}) \\ &\sim \sqrt{2} \frac{1}{\sqrt{2}} \sigma e^{\pm i\phi/2} \rightarrow \phi_{1/2,\pm 1/2} \\ [J^\pm, \phi_{1,\mp 1}] &\sim \sqrt{2}\psi e^{\pm i\phi} \cdot e^{\mp i\phi} \rightarrow \sqrt{2}\psi \end{aligned} \quad (1.109)$$

It follows that, with our notations, the commutations between currents and spin-1/2 fields are the same as in (1.35), while the commutations with the spin-1 field become

($m = 0, \pm 1$):

$$\begin{aligned} [J^0, \phi_{1,m}] &= m\phi_{0,m} \\ [J^\pm, \phi_{1,\mp 1}] &= \sqrt{2}\phi_{1,0} \\ [J^\pm, \phi_{1,0}] &= \sqrt{2}\phi_{1,\pm 1} . \end{aligned} \tag{1.110}$$

We computed (but for a phase) the structure constants of Table 1.3 from the OPEs between the primaries (1.108).

$SU(2)_2$ WZW model describes three non-interacting massless Majorana fermions (the spin-1 fields). Perturbing $SU(2)_2$ with the spin-1 field,

$$H = H_{SU(2)_2} + g \int dx (\phi_{1,1} \bar{\phi}_{1,-1} - \phi_{1,0} \bar{\phi}_{1,0} + \phi_{1,-1} \bar{\phi}_{1,1}) , \tag{1.111}$$

makes the fermions massive. Finding such a spectrum however is a strong check on the TCSA as the massive Majorana fermions are not simply expressible in the conformal current algebra basis.

Fig. 1.12 shows the low lying excited states from the TCSA. The coupling g is fixed to a value where the mass of the first excited state is 1. The TCSA captures this state (the $S_z = 0$ state of the triplet of massive Majoranas) as well as a set of three two particle states with an energy approximately equal to 2. The Majorana fermions are non-interacting, hence their mass must scale linearly with g . This behavior is shown in Fig. 1.13a. We also consider the finite size corrections to one of the two-particle states. Even though non-interacting, the quantization condition for the two-particle state, Eq. 1.53, is non-trivial as one needs to quantize with a doublet of distinct integers (n_1, n_2) , $n_1 \neq n_2$. Fig. 1.13b shows that the TCSA energy of the two-particle state matches the prediction derived from Eq. 1.53.

1.6 Discussions on TCSA and perturbed $SU(2)_k$.

Up to now, we have applied the TCSA to perturbations of $SU(2)_k$. The general methodology is illustrated with various examples. We began by studying the $SU(2)_1 + Tr(g)$ perturbation, equivalent to the sine-Gordon model at a particular value of its coupling. We showed the TCSA accurately captured both the ground state energy and excited state spectrum including finite size corrections. We next turned to $SU(2)_1 + \bar{J}_L \cdot \bar{J}_R$, a WZW model perturbed by a marginal interaction. We demonstrated that one can accurately identify analytically the leading UV divergences in perturbation theory that characterize the ground state energy as computed numerically by the TCSA. By subtracting these UV divergences (i.e. the non-universal contributions to the ground state energy) we isolated

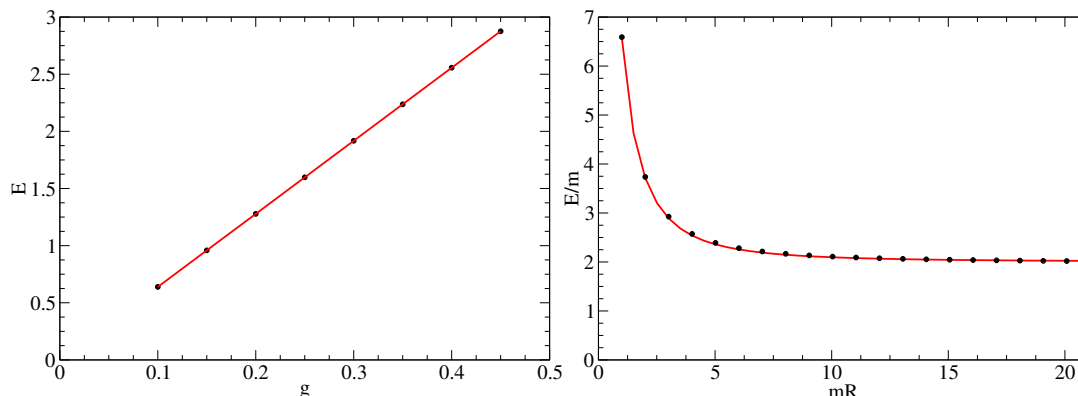


Figure 1.13: a) Linear scaling of the mass of the triplet with the coupling g . b) A comparison of the energy of a two-particle state with $(n_1, n_2) = (-1, 1)$ between TCSA numerics (black dots) and analytics (solid red line).

the universal contribution to the ground state energy due to the marginal perturbation. We find that it differs from that predicted with calculations using Lorentz invariant regulators. Interestingly, away from the marginal point, the universal structure of the ground state energy is restored. Finally we considered $SU(2)_2$ perturbed by $Tr(g)^2$. This model is equivalent to three massive non-interacting Majorana fermions. The TCSA, is able to reproduce the expected spectrum. This is a non-trivial check of our methodology as the Majorana fermions do not have a simple representation in the current algebra basis employed by the approach.

We have developed this capability to study perturbed WZW models in order to tackle a number of problems. In particular, we have two in mind. In the first, we plan to examine the dimerized-frustrated $J_1 - J_2 - \delta$ Heisenberg model whose Hamiltonian is

$$H = \sum_n J_1 (1 + \delta(-1)^n) \bar{S}_n \cdot \bar{S}_{n+1} + J_2 \bar{S}_n \cdot \bar{S}_{n+2}. \quad (1.112)$$

Field theory analyses [67] argue that the low energy sector of this theory is equivalent to

$$H = H_{SU(2)_1} + g \int dx \bar{J}_R \cdot \bar{J}_L + h \int dx (\phi_{1/2,1/2} \bar{\phi}_{1/2,-1/2} - \phi_{1/2,-1/2} \bar{\phi}_{1/2,1/2}), \quad (1.113)$$

where $g \propto J_2 - J_{2c}$ and $h \propto \delta$. If the marginal perturbation g is absent, the model's spin gap, Δ_S , would scale simply with h : $\Delta_S \propto h^{2/3}$. In the presence of g , however, this scaling is altered to become $\Delta_S \propto h^{2/3}/|\log(h)|^{1/2}$. However this altered scaling has been difficult to see in DMRG studies of the dimerized-frustrated Heisenberg model [69, 68]. It would be extremely interesting to analyze this scaling behavior using the TCSA.

Our study here of $SU(2)_1 + \bar{J}_L \cdot \bar{J}_R$ has thus lain the groundwork for this future study.

The second problem that we intend to tackle is the study of possible integrable perturbations of $SU(2)_k$ for $k > 1$. There are indications, coming from Zamolodchikov-type

counting arguments [87], that those perturbations do exist. We intend to study these perturbations with the TCSA, extracting both the spectrum of the model as well as evidence for or against their integrability. The example analyzed in this paper concerning $SU(2)_2$ shows that this goal is within reach.

After the successful application of TCSA to perturbed WZW models, we wonder whether the method can be extended to situations where the space of states is uncountable. In this scenario, it is difficult to understand a priori in which way a truncation should be implemented, as well as what would be the resulting approximation of the system. In the rest of this Chapter dedicated to TCSA, we face this problem and adapt the method to address a specific class of quantum field theory with uncountable space of states: the Landau-Ginzburg theories.

These theories are believed to be non-integrable and hence difficult to tackle analytically. In particular the structure of stable neutral excitation at low energy has been conjectured in Ref. [46], and a numerical confirmation is our main objective. Beside this, understanding how to extend TCSA in the case of an uncountable space of states is interesting by itself as a methodological improvement of the technique.

Before explaining how to apply the TCSA to LG theories we introduce the conjecture in the next Section.

1.7 Landau-Ginzburg Theories and stable bound states.

In this Section, we introduce the conjecture about the structure of the stable low energy excitation spectrum in the important class of quantum field theories given by the Landau-Ginzburg (LG) models. The most familiar example of these models is the Φ^4 LG theory, based on a real scalar field $\phi(x)$ with euclidean action given by

$$\mathcal{S} = \frac{1}{8\pi} \int [(\partial_\mu \phi)^2 + g_2 \phi^2 + g_4 \phi^4] \quad g_4 > 0 . \quad (1.114)$$

For $g_2 > 0$ the theory has a unique vacuum while for $g_2 < 0$ the theory possesses two degenerate vacua, connected by kink excitations. In particular, one of our goals is to confirm a conjecture put forward in [46], i.e. that a non-integrable quantum field theory with degenerate vacua (connected by kink excitations), cannot have more than two stable excitations per vacuum.

The spectrum of non-integrable quantum field theories with topological excitations (kink-like) can be studied by means of Semiclassical Methods [44, 45, 95, 46]. The simplest example of these theories involves a scalar real field $\phi(x)$ and a Lagrangian density

$$\mathcal{L} = \frac{1}{2}(\partial_\mu \phi)^2 - U(\phi) , \quad (1.115)$$

where the potential $U(\phi)$ has several degenerate minima at $\phi_a^{(0)}$ ($a = 1, 2, \dots, n$), as the one shown in Figure 1.14. These minima correspond to the different vacua $|a\rangle$ of the associate quantum field theory.

Basic Excitations. The basic excitations of this kind of models are the kinks and anti-kinks which interpolate between two neighboring vacua. Semiclassically they are described by the static solutions of the equation of motion, i.e.

$$\partial_x^2 \phi(x) = U'[\phi(x)] , \quad (1.116)$$

with boundary conditions $\phi(-\infty) = \phi_a^{(0)}$ and $\phi(+\infty) = \phi_b^{(0)}$, where $b = a \pm 1$. Denoting by $\phi_{ab}(x)$ the solutions of this equation and by $\epsilon_{ab}(x)$ the classical energy density

$$\epsilon_{ab}(x) = \frac{1}{2} \left(\frac{d\phi_{ab}}{dx} \right)^2 + U(\phi_{ab}(x)) , \quad (1.117)$$

the classical expression of the corresponding kink mass is given by

$$M_{ab} = \int_{-\infty}^{\infty} \epsilon_{ab}(x) . \quad (1.118)$$

Once put in motion by a Lorentz transformation, i.e. $\phi_{ab}(x) \rightarrow \phi_{ab}[(x \pm vt)/\sqrt{1-v^2}]$, these configurations describe in the quantum theory the kink states $|K_{ab}(\theta)\rangle$, where a and b are the indices of the initial and final vacuum, respectively. The quantity θ is the rapidity variable which parameterizes the relativistic dispersion relation of these excitations, i.e.

$$E = M_{ab} \cosh \theta , \quad P = M_{ab} \sinh \theta . \quad (1.119)$$

Conventionally $|K_{a,a+1}(\theta)\rangle$ denotes the *kink* between the pair of vacua $\{|a\rangle, |a+1\rangle\}$ while $|K_{a+1,a}(\theta)\rangle$ is the corresponding *anti-kink*: the multi-particle states are then given by a string of these excitations, with the adjacency condition of the consecutive indices for the continuity of the field configuration

$$|K_{a_1,a_2}(\theta_1) K_{a_2,a_3}(\theta_2) K_{a_3,a_4}(\theta_3) \dots\rangle , \quad (a_{i+1} = a_i \pm 1) . \quad (1.120)$$

Neutral Bound States. In addition to the kinks, in the quantum theory there may also exist their bound states. These are the neutral excitations $|B_c(\theta)\rangle_a$ ($c = 1, 2, \dots$)

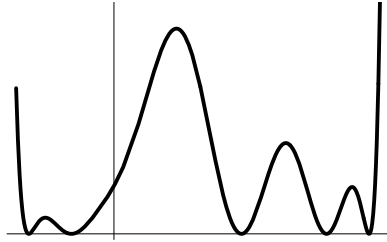


Figure 1.14: Potential $U(\phi)$ of a quantum field theory with kink excitations.

around each of the vacua $|a\rangle$. For a theory based on a Lagrangian of a single real field, in infinite volume these states are all non-degenerate: in fact, there are no extra quantities which commute with the Hamiltonian and that can give rise to a multiplicity of them. The neutral particles must be identified as the bound states of the kink-antikink configurations that start and end at the same vacuum $|a\rangle$, i.e. $|K_{ab}(\theta_1) K_{ba}(\theta_2)\rangle$. If such two-kink states have a pole at an imaginary value iu_{ab}^c within the physical strip $0 < \text{Im } \theta < \pi$ of their rapidity difference $\theta = \theta_1 - \theta_2$, then their bound states are defined through the factorization formula which holds in the vicinity of this singularity

$$|K_{ab}(\theta_1) K_{ba}(\theta_2)\rangle \simeq i \frac{g_{ab}^c}{\theta - iu_{ab}^c} |B_c\rangle_a . \quad (1.121)$$

In this expression g_{ab}^c is the on-shell 3-particle coupling between the kinks and the neutral particle. Moreover, the mass of the bound states is simply obtained by substituting the resonance value iu_{ab}^c within the expression of the Mandelstam variable s of the two-kink channel

$$s = 4M_{ab}^2 \cosh^2 \frac{\theta}{2} \longrightarrow m_c = 2M_{ab} \cos \frac{u_{ab}^c}{2} . \quad (1.122)$$

In order to determine the resonance values u_{ab}^c , one can make use of a remarkably simple formula due to Goldstone-Jackiw [45], that applies in a semiclassical approximation, i.e. when the coupling constant goes to zero and the mass of the kinks becomes correspondingly very large with respect to any other mass scale. In its refined version, given in [95], this formula reads as follows

$$f_{ab}^\phi(\theta) = \langle K_{ab}(\theta_1) | \phi(0) | K_{ab}(\theta_2) \rangle \simeq \int_{-\infty}^{\infty} dx e^{iM_{ab}\theta x} \phi_{ab}(x) , \quad (1.123)$$

where $\theta = \theta_1 - \theta_2$. Substituting in this formula $\theta \rightarrow i\pi - \theta$, the corresponding expression may be interpreted as the following Form Factor

$$F_{ab}^\phi(\theta) = f(i\pi - \theta) = \langle a | \phi(0) | K_{ab}(\theta_1) K_{ba}(\theta_2) \rangle , \quad (1.124)$$

where appears the neutral kink states around the vacuum $|a\rangle$ of interest. Eq. (1.123) deserves several comments:

- the appealing aspect of the formula (1.123) consists of the relation between the Fourier transform of the *classical* configuration of the kink, – i.e. the solution $\phi_{ab}(x)$ of the differential equation (1.116) – and the *quantum* matrix element of the field $\phi(0)$ between the vacuum $|a\rangle$ and the 2-particle kink state $|K_{ab}(\theta_1) K_{ba}(\theta_2)\rangle$;
- given the solution of eq. (1.116) and its Fourier transform, the poles of $F_{ab}(\theta)$ within the physical strip of θ identify the neutral bound states which couple to ϕ . The mass of the neutral particles can be extracted by using eq. (1.122), while the on-shell 3-particle coupling g_{ab}^c can be obtained from the residue at these poles (Figure 1.15)

$$\lim_{\theta \rightarrow iu_{ab}^c} (\theta - iu_{ab}^c) F_{ab}(\theta) = i g_{ab}^c \langle a | \phi(0) | B_c \rangle . \quad (1.125)$$

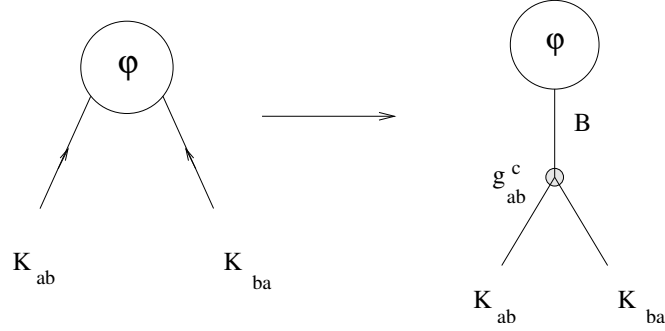


Figure 1.15: Residue equation for the matrix element on the kink states.

The simplest application of this analysis is to the broken phase of the Φ^4 Landau-Ginzburg, whose potential can be chosen as

$$U(\phi) = \frac{\lambda}{4} \left(\phi^2 - \frac{m^2}{\lambda} \right)^2 . \quad (1.126)$$

Denoting with $|\pm 1\rangle$ the vacua relative to the classical minima $\phi_{\pm}^{(0)} = \pm \frac{m}{\sqrt{\lambda}}$ and expanding around them, $\phi = \phi_{\pm}^{(0)} + \eta$, we have

$$U(\phi_{\pm}^{(0)} + \eta) = m^2 \eta^2 \pm m\sqrt{\lambda} \eta^3 + \frac{\lambda}{4} \eta^4 . \quad (1.127)$$

Hence, ordinary perturbation theory predicts the existence of a neutral particle for each of the two vacua, with a bare mass given by $m_b = \sqrt{2}m$, irrespectively of the value of the coupling λ . Let us see, instead, what is the conclusion reached by the semiclassical analysis. The classical kink solutions are

$$\phi_{-a,a}(x) = a \frac{m}{\sqrt{\lambda}} \tanh \left[\frac{mx}{\sqrt{2}} \right] , \quad a = \pm 1 \quad (1.128)$$

and their classical mass is

$$M_0 = \int_{-\infty}^{\infty} \epsilon(x) dx = \frac{2\sqrt{2}}{3} \frac{m^3}{\lambda} . \quad (1.129)$$

By taking into account the contribution of the small oscillations around the classical static configurations, the kink mass gets corrected as [44]

$$M = \frac{2\sqrt{2}}{3} \frac{m^3}{\lambda} - m \left(\frac{3}{\pi\sqrt{2}} - \frac{1}{2\sqrt{6}} \right) + \mathcal{O}(\lambda) . \quad (1.130)$$

So, introducing

$$c = \left(\frac{3}{2\pi} - \frac{1}{4\sqrt{3}} \right) > 0 ,$$

and the dimensionless quantities

$$g = \frac{3\lambda}{2\pi m^2} \quad ; \quad \xi = \frac{g}{1 - \pi c g} \quad , \quad (1.131)$$

the mass of the kink can be expressed as

$$M = \frac{\sqrt{2}m}{\pi \xi} = \frac{m_b}{\pi \xi} \quad . \quad (1.132)$$

Since the kink and the anti-kink solutions are equal functions (up to a sign), their Fourier transforms have the same poles and therefore the spectrum of the neutral particles will be the same on both vacua, in agreement with the Z_2 symmetry of the model. We have

$$f_{-a,a}(\theta) = \int_{-\infty}^{\infty} dx e^{iM\theta x} \phi_{-a,a}(x) = i a \sqrt{\frac{2}{\lambda}} \frac{1}{\sinh\left(\frac{\pi M}{\sqrt{2}m}\theta\right)} \quad .$$

By making now the analytical continuation $\theta \rightarrow i\pi - \theta$ and using the above definitions (1.131), we have

$$F_{-a,a}(\theta) = \langle a \mid \phi(0) \mid K_{-a,a}(\theta_1) K_{a,-a}(\theta_2) \rangle \propto \frac{1}{\sinh\left(\frac{(i\pi-\theta)}{\xi}\right)} \quad . \quad (1.133)$$

whose poles are placed at

$$\theta_n = i\pi(1 - \xi n) \quad , \quad n = 0, \pm 1, \pm 2, \dots \quad (1.134)$$

Notice that, if

$$\xi \geq 1 \quad , \quad (1.135)$$

none of these poles is in the physical strip $0 < \text{Im } \theta < \pi$. Consequently, in the range of the coupling constant

$$\frac{\lambda}{m^2} \geq \frac{2\pi}{3} \frac{1}{1 + \pi c} = 1.02338\dots \quad (1.136)$$

the theory does not have any neutral bound states, neither above the vacuum to the right nor above the one to the left. Viceversa, if $\xi < 1$, there are $n = \left[\frac{1}{\xi}\right]$ neutral bound states, where $[x]$ denote the integer part of the number x . Their semiclassical masses are given by

$$m_n = 2M \sin\left[n \frac{\pi \xi}{2}\right] = n m_1 \left[1 - \frac{3}{32} \frac{\lambda^2}{m^4} n^2 + \dots\right] \quad . \quad (1.137)$$

It is easy to see that the leading term of this expression is given by multiples of the mass of the elementary boson $|B_1\rangle$. This leads to the interpretation of the n -th breather as a loosely bound state of n of it, with the binding energy provided by the remaining terms of the above expansion. However, as a consequence of the non-integrability of the theory,

all particles with mass $m_n > 2m_1$ will eventually decay. Investigating further this aspect and analyzing the picture which emerges by varying ξ , if there are at most two particles in the spectrum, it is always valid the inequality $m_2 < 2m_1$. However, if $\xi < \frac{1}{3}$, for the higher particles one always has

$$m_k > 2m_1 \quad , \quad \text{for } k = 3, 4, \dots, n \quad . \quad (1.138)$$

Hence, according to the semiclassical analysis, the spectrum of neutral particles of ϕ^4 theory is, for each vacuum, as follows [46]:

- if $\xi > 1$, there are no neutral particles;
- if $\frac{1}{2} < \xi < 1$, there is one particle;
- if $\frac{1}{3} < \xi < \frac{1}{2}$ there are two particles;
- if $\xi < \frac{1}{3}$ there are $\left\lceil \frac{1}{\xi} \right\rceil$ particles, although only the first two are stable, because the others are resonances.

1.8 TCSA for Landau-Ginzburg theories.

In this section we discuss the implementation of the Truncated Conformal Spectrum Approach (TCSA) to Landau-Ginzburg theories. TCSA is a numerical method suitable to study theories which can be written as a Conformal Field Theory (CFT) plus some relevant perturbations, where these perturbations are expressed in terms of matrix elements of the primary operators of the CFT itself. Such a Hamiltonian can be truncated by just discarding all states above a truncation level N_{tr} or, equivalently, by introducing a UV energy cutoff within the conformal theory (E_{tr}). The resulting truncated Hamiltonian is then diagonalized. As far as the low energy states of the perturbed and the original CFT theory are adiabatically related, the error made on the determination of the lower eigenvalues decreases exponentially while increasing the truncation.

If the CFT has a countable number of representations, whose highest-weight states are ordered in energy, the truncation can be performed by keeping those representations with the energy of the highest-weight state below the UV cutoff. Serious problems arise instead when the CFT has an uncountable set of representations, as it happens in the Landau-Ginzburg theories described by an euclidean action of the form

$$\mathcal{S} = \frac{1}{8\pi} \int d^2x \left(\partial_\mu \phi \partial^\mu \phi + \sum_n g_n \phi^n \right). \quad (1.139)$$

The kinetic part is a $c = 1$ CFT, the free boson, while the potential can be considered as a multiple perturbation thereof. The spectrum generating algebra of this CFT is $U(1)_1$

defined by the commutation relations

$$[a_n, a_m] = n\delta_{n+m,0} \quad , \quad [\bar{a}_n, \bar{a}_m] = n\delta_{n+m,0}$$

for the holomorphic and antiholomorphic sectors respectively. This algebra admits a continuum of representations with conformal dimension $h = \bar{h} = \alpha^2/2$, for all $\alpha \in \mathbb{R}$. Hence this direct approach results in an uncountable set of primary states in the conformal basis, making impossible the reduction of the Hilbert space of the $c = 1$ theory to a finite subspace by just introducing a UV cutoff. Therefore, to apply TCSA to LG theories we need to follow another route and to select a discrete computational basis over which the Hamiltonian can be truncated in a meaningful way.

It is also important to notice that the field $\phi(x)$ and all its powers are not primary fields of the $c = 1$ CFT of the free boson. In the following we will address this issue introducing two specific methods to express the powers ϕ^m in terms of primary fields of the theory.

1.8.1 The (conformal) computational basis.

With the aim of selecting a manageable computational basis, let's consider a free compactified boson [2], which is defined on the cylinder of circumference R , and takes values on a circle of length $2\pi/\beta$ so that

$$\phi(x + R) \equiv \phi(x) + \frac{2\pi}{\beta}w. \quad (1.140)$$

The integer w counts the number of windings of the field in its internal space while the spatial coordinate runs once around the cylinder. The compactification induces a quantization of the momentum that results in a countable set of primaries $V_{n,w}$, with conformal weights

$$h_{n,w} = \frac{1}{2} \left(n\beta + \frac{w}{2\beta} \right)^2 \quad , \quad \bar{h}_{n,w} = \frac{1}{2} \left(n\beta - \frac{w}{2\beta} \right)^2 \quad (1.141)$$

where n and w are integer numbers, and energies

$$E_{n,w} = \frac{2\pi}{R} \left[(n\beta)^2 + \left(\frac{w}{2\beta} \right)^2 \right] - \frac{\pi}{6R}. \quad (1.142)$$

The primary state related to each representation can be defined by the action of a vertex operator on the vacuum, i.e. $|n, w\rangle \equiv V_{n,w}(0)|0\rangle$. The conformal towers, built by acting with $U(1)_1$ holomorphic and antiholomorphic modes on each primary state, provide a discrete basis where to represent the Hamiltonian.

The TCSA can be now straightforwardly applied to the compactified boson, and the

truncation is realized by keeping states (including primaries) with energy below the UV cutoff. Increasing the compactification radius, the number of representations increases and the \mathbb{R} -valued free boson is in principle recovered in the limit $1/\beta \rightarrow \infty$. So, in a nutshell, the idea is to use the truncated basis of the compactified boson in the limit of very large compactification radius as a computational basis for the perturbed theory (1.139), with the number of representations, and thus the number of states in the theory, that grows at most linearly with the compactification radius at a fixed truncation.

Since we will be interested in the sector of the spectrum with zero topological charge, we restrict from now on our attention to the $w = 0$ winding sector, although the following results can be easily generalized to generic winding numbers. The highest weight states, denoted now by $|n\rangle$, are thus generated from the vacuum $|0\rangle$ by applying the primary fields as

$$|n\rangle \equiv e^{i\beta n\phi(0)} |0\rangle \quad \text{with} \quad \phi(0) = \phi_L(0) + \phi_R(0) . \quad (1.143)$$

The energies of such highest weight states are given by

$$E_n = \frac{2\pi}{R} \left[\frac{(n\beta)^2}{2} - \frac{1}{12} \right] . \quad (1.144)$$

From each highest weight state, the descendants are obtained by applying the left and right modes of the field,

$$|n, a_L, a_R\rangle = a_{-1}^{p_1} a_{-2}^{p_2} \dots \bar{a}_{-1}^{q_1} \bar{a}_{-2}^{q_2} \dots |n\rangle . \quad (1.145)$$

Their energy is computed to be

$$E = E_n + \sum_{j=1} j (p_j + q_j) , \quad (1.146)$$

and the restriction to energies below E_{tr} is now a well defined operation.

1.8.2 The perturbation: the Fourier method

Even though the compactified boson provides the computational basis for the TCSA, we have still to understand how to write the perturbation part of the Hamiltonian within this framework. Perturbations of the LG theories are powers of the bosonic field $\phi(x)$ and in general they are *not* periodic of $2\pi/\beta$. Hence, they do not belong to the operator content of the considered CFT. The most natural way-out to represent the perturbation within the compactified theory is to expand the various powers $\phi^m(x)$ in terms of their Fourier series

$$\phi^m(x) \equiv \sum_{p \in \mathbb{Z}} c_p e^{ip\beta\phi(x)} , \quad (1.147)$$

where the Fourier coefficients are computed according to

$$c_p = \frac{\beta}{2\pi} \int_{-\pi/\beta}^{\pi/\beta} d\phi e^{-i\beta p\phi} \phi^m = \frac{p(-1)^n}{(n\beta)^p} \sum_{\substack{k=0 \\ k \text{ even}}}^{p-2} (-1)^{\frac{k}{2}+1} \frac{(p-1)!}{(p-k-1)!} (\pi n)^{p-k-2}. \quad (1.148)$$

In this way, the operator $\phi^m(x)$ is written as a linear combination of primary fields of the theory and its matrix elements between two states $|n, a_L, a_R\rangle$ and $|n', b_L, b_R\rangle$ can then be written as a sum of matrix elements of the primaries

$$M_{ab}^{(m)} = \sum_{p \in \mathbb{Z}} c_p \left(\frac{2\pi}{R} \right)^{(p\beta)^2} \langle n, a_L, a_R | e^{ip\beta\phi} | n', b_L, b_R \rangle. \quad (1.149)$$

The scaling factors $(2\pi/R)^{(n\beta)^2}$, which originate from the conformal mapping of the three-point function of the primary fields from the plane to the cylinder, provide the correct conformal dimension to the operators entering the Fourier series (1.147). It is important to observe that these factors implement a normal ordering of the operators so that, at the matrix level, we have that $\phi^{2n} \neq (\phi^2)^n$. Each remaining expectation value can be split as

$$\langle n, a_L, a_R | e^{ip\beta\phi} | n', b_L, b_R \rangle = \langle n, a_L | e^{ip\beta\phi_L} | n', b_L \rangle \langle n, a_R | e^{ip\beta\phi_R} | n', b_R \rangle, \quad (1.150)$$

and computed just using the commutator between the vertex operators and the modes

$$[a_n, e^{ip\beta\phi}] = -p\beta e^{ip\beta\phi}, \quad (1.151)$$

and the definition of the three-point-function:

$$\langle n | \phi^m(0) | n' \rangle = \int_{-\pi/\beta}^{\pi/\beta} d\phi \phi^m e^{i(n-n')\beta\phi}. \quad (1.152)$$

Let us mention that a simple check of the soundness of this approach to implement the TCSA for perturbed $c = 1$ CFT based on the compactified boson, is provided by the Sine-Gordon model. We have indeed tested that our method is able to reproduce well known results about this model, as briefly discussed in Appendix A.

However, to fully implement the strategy discussed so far, one must pay attention to another subtle aspect: it is well known in the TCSA literature [21] that operators with conformal dimension higher than one lead to UV divergences that must be treated properly to extract universal features from the numerical data. In our case the Fourier series associated to the various powers $\phi^m(x)$ requires infinitely many UV divergent terms to approximate the LG potential on the target space. A rather pragmatic way to cure this pathology is to truncate the Fourier expansion (1.147) to include only UV convergent operators, i.e. those with conformal dimension less than one, $|n| < 1/\beta$.

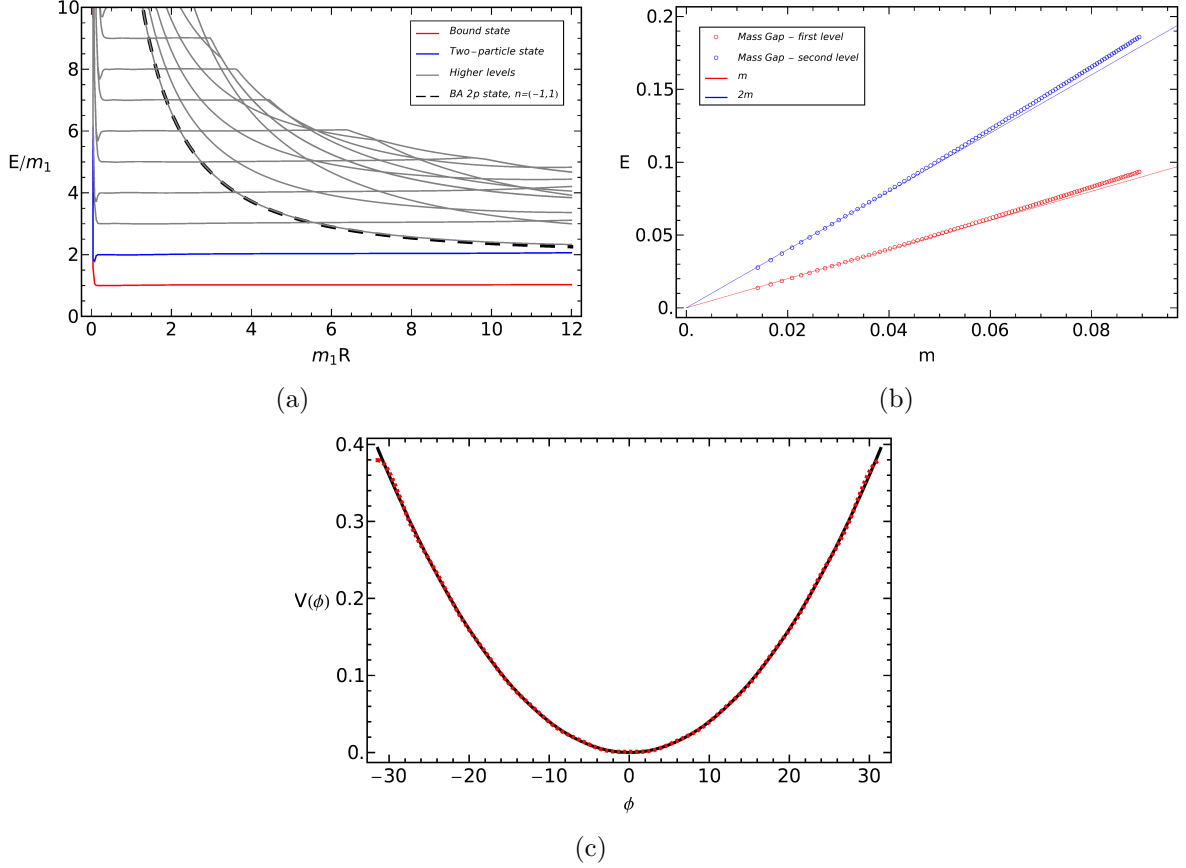


Figure 1.16: In panel (a) we show the energy levels with the ground states subtracted for the ϕ^2 perturbation. Here $\beta = 0.1$, $g_2 = 0.0004$, and $N_{\text{tr}} = 6$. The mass is given by $m_1 = 2\sqrt{g_2} = 0.04$. The solid black line represents the (trivial) Bethe-ansatz prediction. In panel (b) we show the energy of the first two levels as a function of $m = 2\sqrt{g_2}$. Their values are compared with the expected one of a free theory (here $m_1 R = 4$). Panel (c) shows the exact shape of the target potential in black, and its approximation with a dashed red line. For $\beta = 0.1$ the first 21 primaries in the representation (1.147) are retained.

In order to test whether this method provides sound results, we have firstly studied the simplest LG theory, i.e. the free massive boson

$$\mathcal{S} = \frac{1}{8\pi} \int d^2x \left(\partial_\mu \phi \partial^\mu \phi + g_2 \phi^2 \right) . \quad (1.153)$$

It turns out that the numerical results are in rather good agreement with theoretical predictions already for $\beta = 0.1$ and $N_{\text{tr}} = 6$. The representation (1.147) is truncated in this case to 21 vertex operators with conformal dimension $(n\beta)^2 < 1$ and the ϕ^2 potential is closely approximated, see Fig. 1.16(c). In Fig. 1.16(a), we show the low energy spectrum of the theory. The plot refers to the energy differences with respect to the ground state energy of the theory and, as in other similar plots shown below, once we have determined the smallest particle mass m_1 , the energy differences have been rescaled with such mass and plotted as function of $m_1 R$. We will always restrict to states with zero total momentum. It is however trivial to study also sectors with higher total momentum.

The general features of these energy difference lines are pretty clear

- For small values of $m_1 R$, the Hamiltonian of the unperturbed CFT dominates and therefore the resulting spectrum is the conformal one, with the typical dependence $1/R$ of the various lines. The degeneracies that we find are those expected for the free compactified boson: there is a single ground state (not shown in the figure since it has been subtracted), while the low lying states are coupled in doublets corresponding to the primaries with $\pm n$ for increasing $n < \frac{1}{\beta}$. Potting more states it is also possible to see the corresponding descendants with the correct degeneracy.
- For larger values of $m_1 R$, we expect the perturbation to become more and more important until eventually some truncation effects start to be dominant and the data are no longer reliable. Therefore the physically sensitive data must be extracted in the intermediate region, the so called *scaling region*, soon after a very rapid crossover to a massive (gapped) theory takes place. The state with a single particle is the one colored in red while the second level (blue) is a state with two particles, both at zero momentum. This state has energy exactly $2m_1$, the threshold. These two particles do not interact in this case, since the theory is free. The higher horizontal lines can be interpreted as states with many non-interacting particles, each of them with zero total momentum. Finally, the lines decreasing as $1/(m_1 R)$ may be regarded as total zero momentum states with many particles, event though some of them can have non-zero momentum. The lowest of these momentum lines corresponds to a double degenerate state with two particles of momentum $k_n = (2\pi/R)n$, for $n = \pm 1$. For $R \rightarrow \infty$, it will get closer and closer to the threshold line. This picture is confirmed by the comparison with the trivial Bethe-ansatz prediction of the energy of a two particle state with Bethe numbers $(1, -1)$ and with no interaction, $E = 2\sqrt{k_1^2 + m_1^2}$. This is shown in the plot as the black, dashed line. Finally, in Fig. 1.16(b) we show

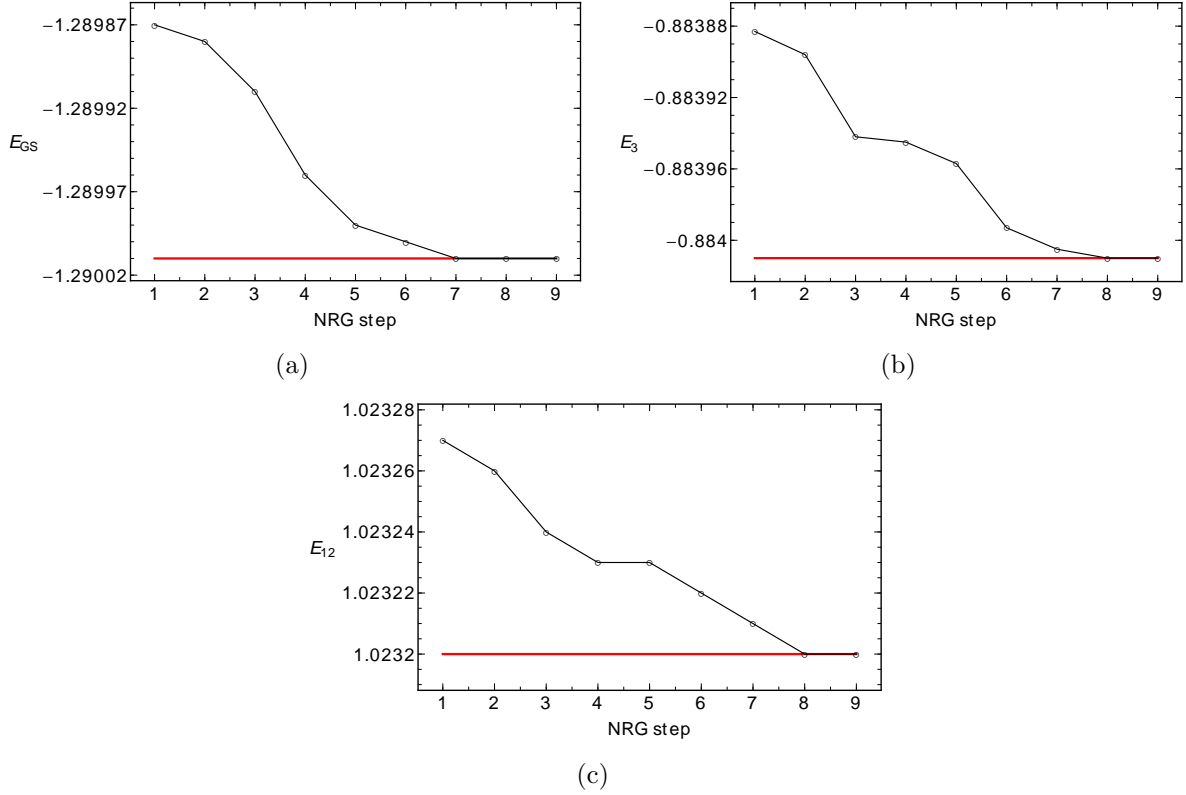


Figure 1.17: We show the convergence of the NRG (black dots) to the exact diagonalization (solid red curve) within the Fourier-method. The truncation level is always fixed to $N_{\text{tr}} = 7$ and $\beta = 0.07$, hence the computational basis contains $N_{\text{tot}} = 11003$ states. Here we chose $N = 6003$, $\Delta N = 500$. The coupling are fixed to be: $g_2 = -0.025$, and $g_4 = 2.6172 \times 10^{-5}$, while $m_1 R \approx 0.51$. We show the convergence of the NRG for (a) the ground state, (b) the third state (the bound state B_1), and (c) the 12th state.

the energy of the two first levels as function of the mass $m = 2\sqrt{g_2}$ at fixed cylinder radius R . The agreement with the expected values m and $2m$ again confirms the reliability of the method.

In the following we will address just Z_2 invariant LG theories, but the method straightforwardly applies also to potential containing odd powers of ϕ .

1.8.3 Numerical Renormalization Group

The accuracy of the numerical values of the energy levels can be improved by means of the Numerical Renormalization Group (NRG). The NRG is a technique that allows the TCSA to include states at much higher conformal levels than would be possible with a straight exact diagonalization.

In this procedure we implicitly assume the localization of the low energy states of the

full theory on the low energy states of the computational basis. Even if this assumption is guaranteed in principle only for relevant perturbations, in Ref. [32] it has been shown that, in the case of a marginal perturbation where the high and low energy sectors of the theory are more tightly coupled, the method still works properly.

In the framework of the compactified boson we need to deal with many perturbations with different conformal dimensions. We have checked that even in this case the method applies and the energies computed with the NRG converge to those obtained by direct diagonalization, as shown in Fig. 1.17.

1.9 Double well potential and stable neutral bound states.

In this section we present a series of results which support the conjecture on the number of stable neutral bound states discussed in Section 1.7 for various double well potentials. Let us start our discussion from the Φ^4 LG theory

$$\mathcal{S} = \frac{1}{8\pi} \int d^2x \left(\partial_\mu \phi \partial^\mu \phi + g_2 \phi^2 + g_4 \phi^4 \right) , \quad (1.154)$$

in the regime where two wells are present, i.e. $g_2 < 0$, and $g_4 > 0$. We have restricted our analysis to the regime $\xi \ll 1$ (see eq. (1.131) for the definition of ξ), in which the Fourier method is supposed to perform better as the shape of the potential is well approximated by a limited number of terms. Although in this regime $[1/\xi]$ neutral bound states are predicted to exist, just two of them can be stable.

Let's now describe our results for a representative choice of the ϕ^4 potential with $\xi \approx 10^{-4}$. The potential we consider is shown in Fig. 1.18(a) (black solid line), together with its Fourier approximation (dashed red line), while in Fig. 1.18(b) we present the low energy spectrum.

As for the ϕ^2 potential, we subtract to all energy levels the ground state energy and we rescale these differences with an estimate of the first mass m_1 . As usual, in the small $m_1 R$ region the conformal part of the Hamiltonian dominates and the low energy levels have the correct degeneracy of the unperturbed CFT: we have a single ground state⁹ corresponding to the identity operator and double degenerate states corresponding to other primary fields. On the other hand, for large values of $m_1 R$ (in this case $(m_1 R) \gtrsim 12$), truncation effects become important and the data are no longer reliable. Hence in this case the scaling region of this theory is identified by the interval $1 < m_1 R < 12$. Here one can see that the first level (green) rapidly goes to zero, which signals the finite-volume double degenerate ground state: indeed, due to finite-volume tunneling effect, the two infinite-volume degenerate ground states have an exponentially small splitting of their energies

⁹The single ground state is subtracted to other energy levels, hence it does not appear in the figure.

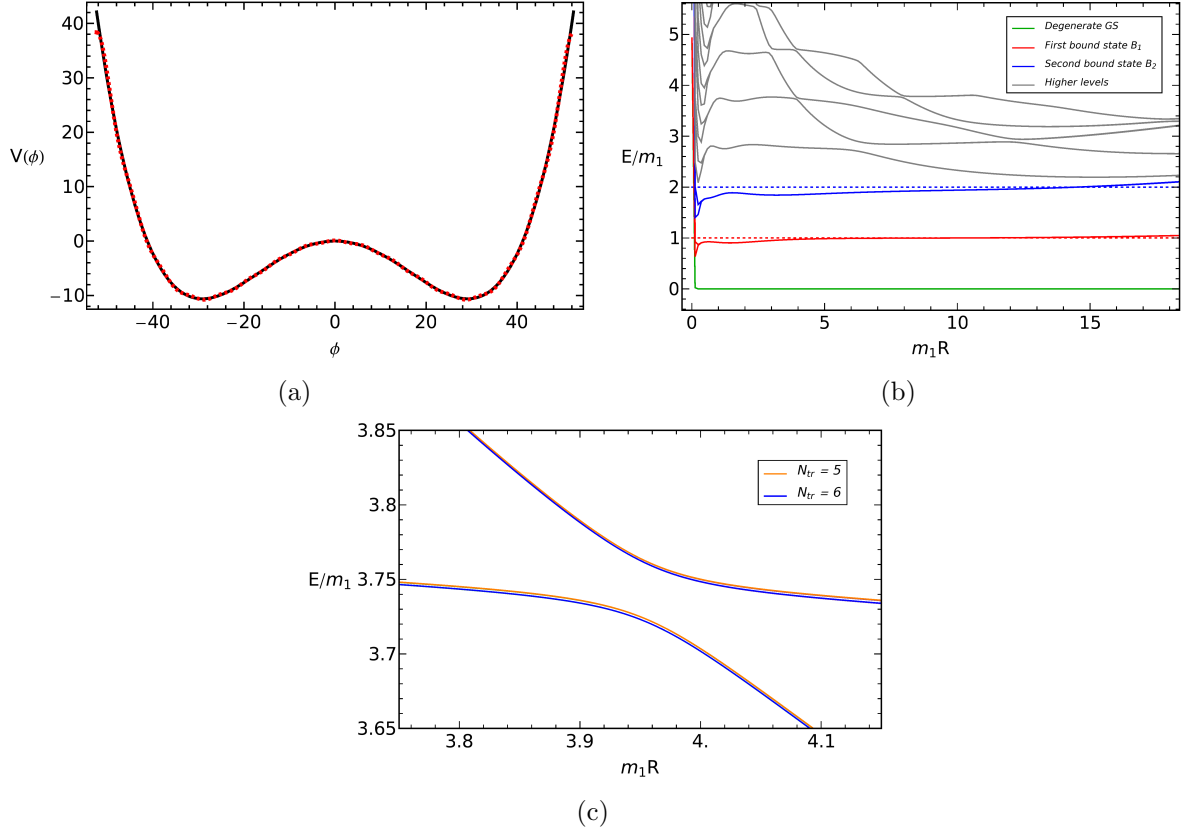


Figure 1.18: (a) The potential for $g_2 = -0.025$, $g_4 = 1.47218 \times 10^{-5}$ and $\xi \approx 5.6 \times 10^{-4}$ is shown in black. The dashed red line represents its approximation within the Fourier method when the Fourier representation (1.147) is truncated to the 33 terms with $(n\beta)^2 < 1$, with $\beta = 0.06$. (b) The low energy levels of the mass spectrum for the Φ^4 LG theory. The truncation level is fixed to $N_{tr} = 6$, and $\beta = 0.06$. In this regime the semiclassical analysis tells that just the first two of the $[1/\xi]$ predicted neutral bound states on each vacuum can be stable. The two lower states become exponentially degenerate for $m_1 R > 0.1$ and they correspond to the double degenerate ground state of the Φ^4 LG theory (green line). The first double-degenerate level (red) is believed to be the neutral bound state B_1 , while the double-degenerate blue line is related to the second bound state B_2 . The conjectured spectrum is thus recovered. The mass of B_2 is predicted to be $m_2 \approx 2 - \frac{3}{8}\xi^2 \approx 2 - 10^{-6}$. Panel (c) shows a detail of the avoided crossing at $m_1 R \approx 4$.

once the theory is defined on a cylinder of radius R . Above this double degenerate ground state a gap is opened and two degenerate states are present (red), each of them corresponding to the neutral bound state B_1 . Above these two more degenerate states (blue) finally appear just below the threshold at $2m_1$, and correspond to B_2 .

Within the region $1 < m_1 R < 4$, one can observe almost parallel levels roughly spaced

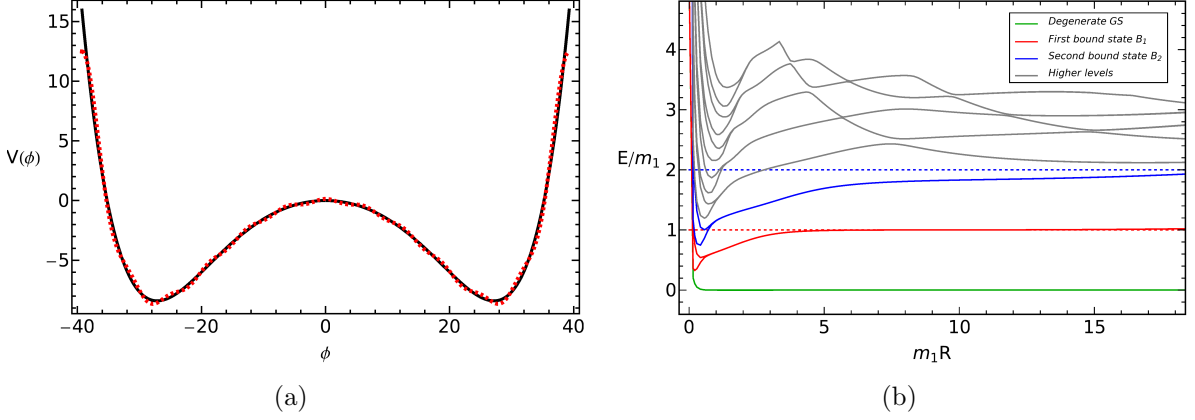


Figure 1.19: (a) The exact ϕ^6 potential with couplings $g_2 = -0.015$, $g_4 = -5.68047 \times 10^{-6}$, and $g_6 = 1.43412 \times 10^{-8}$ is shown in black. The red dashed line represents the approximation used within the Fourier method, for $\beta = 0.08$ (the 25 primaries with $(n\beta)^2 < 1$ are retained). (b) The low energy mass spectrum of the Φ^6 LG theory for the two wells potential. The truncation level is fixed to $N_{\text{tr}} = 6$, and $\beta = 0.08$.

by an energy $\Delta E \approx m_1$, which can be interpreted as the states predicted by eq. (1.137) with $n \geq 3$. The energy levels decreasing in $m_1 R$ are reminiscent of the momentum lines already seen for the free Φ^2 LG theory in Fig. 1.16(a). With respect to the free theory where all the levels were crossing with each others, in the spectrum of Fig. 1.18(b) there are instead many avoided crossings, although their identification may require to study the region where they occur with a higher numerical resolution. An example is given in Fig. 1.18(c) where we show a detail of the avoided crossing at $m_1 R \approx 4$.

In summary, the spectrum we obtain satisfies all the expectations about the Φ^4 LG theory. Moreover, we find that the number of *stable* neutral bound states is at most two per minimum, as predicted in Ref. [46].

We have also tested the conjecture of Ref. [46] in the double well phase of the Φ^6 LG theory for the potential depicted in Fig. 1.19(a). For this LG theory, we study the potential in the range of its parameters for which it is most faithfully reproduced by its truncated Fourier approximation. In this regime we find again the same features that we discussed for the ϕ^4 potential, as can be seen in the energy spectrum presented in Fig. 1.19(b). Also in this case, after a very short conformal behavior of the energy levels, a massive regime is quickly reached with a double degenerate ground state (green), a first double degenerate single particle state B_1 (red), and a second double degenerate single particle state B_2 (blue). Again we find the unstable states of eq. (1.137) for $n \geq 3$ and some reminiscent of the momentum lines decreasing with $m_1 R$.

At this point, a discussion about how the parameter β can be chosen to improve the accuracy of the numerical results is in order. In principle, the precision of TCSA data

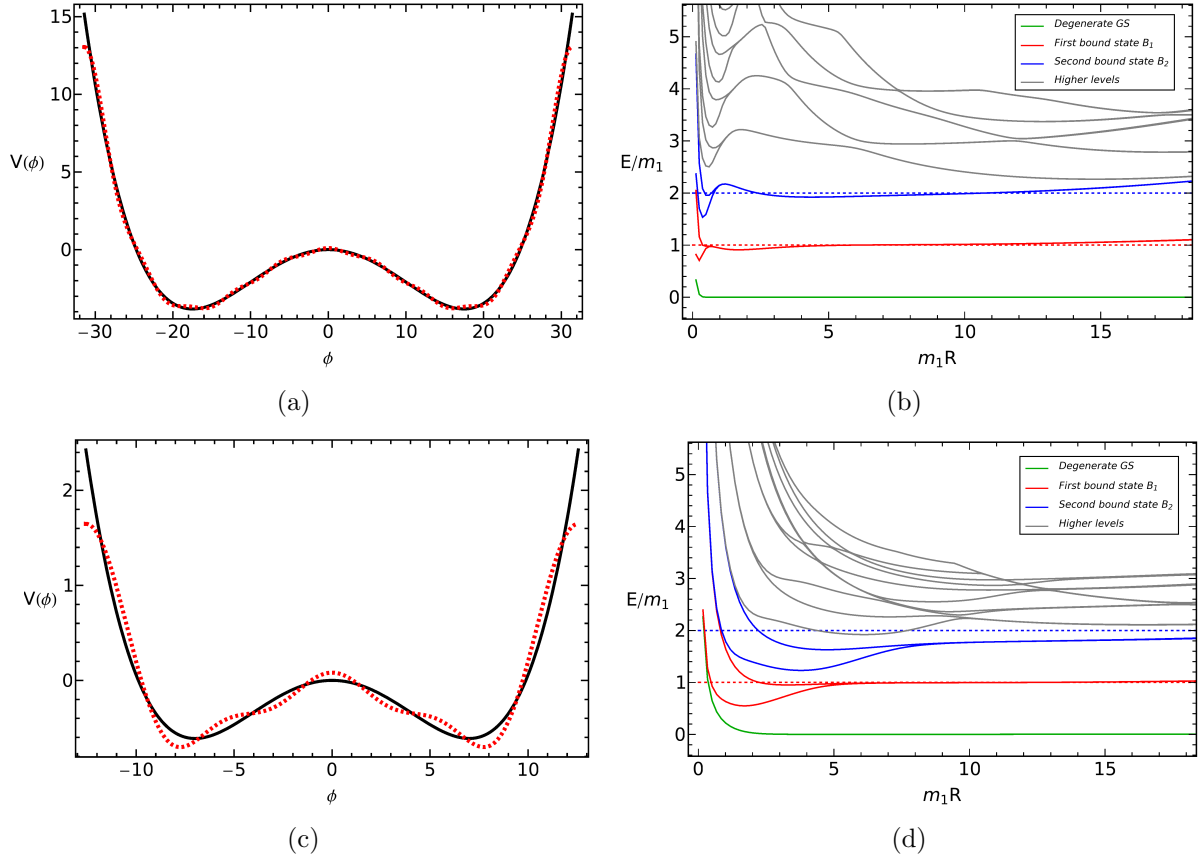


Figure 1.20: We show the effect of a different compactification radius $1/\beta$ on the spectrum of the Φ^4 LG theory already presented in Fig. 1.18. In the left panels, the black lines represent the exact shape of the ϕ^4 potential for (a) $g_2 = -0.025$, $g_4 = 4.08938 \times 10^{-5}$, $\beta = 0.1$, and (c) $g_2 = -0.025$, $g_4 = 2.55586 \times 10^{-4}$, $\beta = 0.25$. The dashed red lines in the same panels are the approximations used within the Fourier method. The related spectra are shown respectively in (b) and (d). Observe that the general quality of the spectrum as well as the precision of the approximation of the second bound state (predicted mass $m_2 \approx 2$) increases decreasing β .

can be improved to the desired accuracy by making β smaller and smaller. The idea is to implement the following transformation on the field that leaves the theory unchanged from the physical point of view:

$$\phi' = \frac{\beta}{\beta'} \phi. \quad (1.155)$$

The new field ϕ' lives in the interval $[-\pi/\beta', \pi/\beta']$ and, beside of an overall multiplicative factor in the Lagrangian, this transformation induces the following rescaling of the couplings:

$$g'_{2n} = \left(\frac{\beta'}{\beta} \right)^{2n-2} g_{2n}. \quad (1.156)$$

As already mentioned, this transformation does not change the physics of the problem. Hence, if we could retain all terms in the truncated Fourier approximation and all states in the computational basis, this transformation would not actually change anything. On the contrary, from the numerical point of view, with $\beta' < \beta$ we both increase the number of terms in the Fourier representation and the number of conformal towers included in the computational basis. This amounts to a better approximation of the studied potential and of the low energy states, but involves a higher computational cost, since the dimension of the matrix to be diagonalized increases. In Fig. 1.20, we show the same ϕ^4 theory discussed in Fig. 1.18 but with different choices of β (and with the parameters rescaled as discussed in eq. (1.156)). As expected, the best approximation is found for the smallest value of β .

1.9.1 LG theories and minimal models.

An important remark concerns the LG theories studied in this paper and the LG theories entering the description of minimal models of CFT proposed by Zamolodchikov [96]. Let us discuss in particular the vacuum structure of these two theoretical frameworks which happen to share the same name.

In our case, the starting point has been a CFT with $c = 1$ and we have used the computational basis of the (compactified) boson $\phi(x)$ to compute the matrix elements of the various powers entering the interaction terms. For the normal order prescription, for the corresponding matrices we have $\phi^{2n} \neq (\phi^2)^n$, and therefore one should not expect that the vacuum structure identified by the classical potential will be necessarily realized by the TCSA implementation of the Hamiltonian. Consider for instance the Φ^6 LG theory associated to the potential

$$V(\phi) = \phi^2 (\phi^2 - a^2)^2 = \phi^6 - 2a^2 \phi^4 + a^4 \phi^2 . \quad (1.157)$$

At the classical level, this theory has three degenerate vacua, one at the origin and the other two placed at $\phi = \pm a$. One could think that the same vacuum structure would be realized in the TCSA implementation of this LG potential by tuning the coupling constants in front of the various matrices as in eq. (1.157), but this turns out to be false. First of all, notice that the second derivatives around different minima are always different:

$$V''(0) \equiv m_0^2 = 2a^4 \quad , \quad V''(\pm a) \equiv m_a^2 = 8a^4 \quad , \quad (1.158)$$

with $m_a^2 > m_0^2$. This means that, while *classically* the minima are degenerate, this is no longer true once quantum corrections are introduced. Indeed, in a semi-classical picture [97], these quantum corrections will depend on the shape of the potential near each minimum: calling $E_{\text{vac}}^{(0)}$ and $E_{\text{vac}}^{(\pm a)}$ the vacuum energy state around each classical minima,

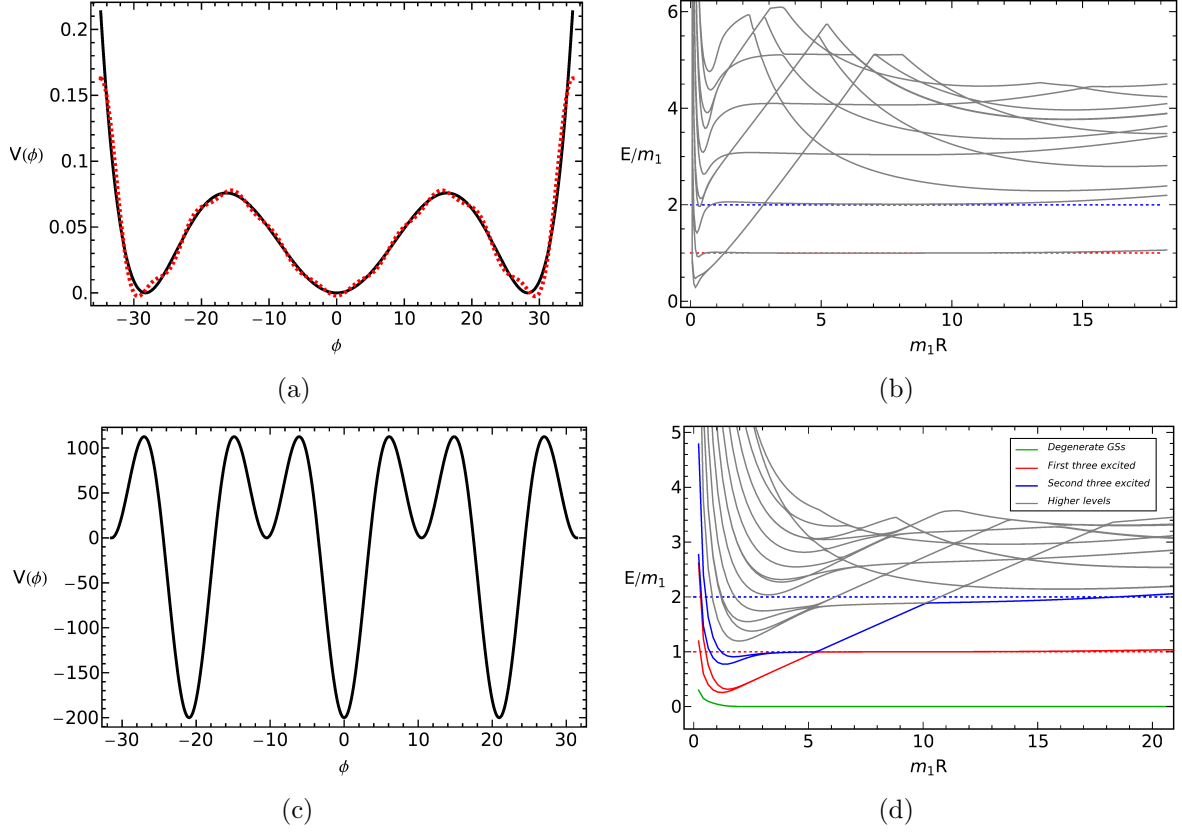


Figure 1.21: (a) The ϕ^6 potential with $g_2 = 0.00064$, $g_4 = -1.6 \times 10^{-6}$, and $g_6 = 1. \times 10^{-9}$ at $\beta = 0.09$. Although the potential has three degenerate wells, in the spectrum (b) there are two towers of states, the first relative to the vacuum in the central well, and the second relative to the two degenerate vacua produced by the two lateral wells. The states relative to the central well are single degenerate and they are parallel to the corresponding ground state (hence they are horizontal when the ground state is subtracted). The states belonging to the lateral wells are double degenerate and are increasing linearly in $m_1 R$. (d) The low energy spectrum for the potential $V(\phi) = -\cos(3\beta\phi) - \cos(6\beta\phi)$ at $\beta = 0.1$, depicted in (c). The shape of the potential is the same around each minimum. The first two states (green) quickly converge to zero, signaling a triple degenerate ground state. The spectrum contains two stable triplets (red and blue) of neutral bound states. The levels increasingly linearly in $m_1 R$ belong to the three smaller wells with higher minima.

a semi-classical analysis gives

$$\begin{aligned} E_{\text{vac}}^{(0)} &\equiv \frac{\hbar R}{4\pi} \int \sqrt{k^2 + m_0^2} dk + \mathcal{O}(\hbar^2) \\ E_{\text{vac}}^{(\pm a)} &\equiv \frac{\hbar R}{4\pi} \int \sqrt{k^2 + m_a^2} dk + \mathcal{O}(\hbar^2) \end{aligned} \quad (1.159)$$

Regularizing the integrals above by a ultraviolet cut-off Λ , the lifting of the classical degeneracy is given by

$$\Delta E_{\text{vac}} = E_{\text{vac}}^{(\pm a)} - E_{\text{vac}}^{(0)} \simeq \frac{\hbar R}{4\pi} (m_a^2 - m_0^2) \log \Lambda . \quad (1.160)$$

So, the expectation is that the quantum corrections will select as ground state energy the one associated to the vacuum at the origin (that becomes therefore the true vacuum of the theory), while the energies relative to the classical vacua at $\phi = \pm a$ will be shifted symmetrically higher with respect to it. This is indeed what is observed in the data coming from a TCSA implementation of the potential in eq. (1.157): in Fig. 1.21(b), where are plotted the differences of energies with respect to the ground state, one can observe a single degenerate tower of states relative to the vacuum at the origin and a double degenerate set of lines which increase linearly in R with respect to the previous ones. The double degeneracy of these linearly increasing lines is obviously due to the symmetry between the original classical vacua at $\phi = \pm a$.

The same effect of lifting the classical vacuum degeneracy also holds for higher order LG. For instance, considering a more complicated example

$$V = \phi^2(\phi^2 - a^2)^2(\phi^2 - b^2)^2 , \quad (1.161)$$

with $b^2 > a^2$, the classical degenerate vacua placed at $\phi = 0$, $\phi = \pm a$ and $\phi = \pm b$ cannot have all the same curvature¹⁰. Hence, considering the quantum corrections, less than five ground states are expected.

It is easy to see that, within the polynomial LG potentials, it is impossible to realize a situation where all classical vacua share the same curvature. The only exceptions are given by potentials which have just two symmetric wells with respect to the origin (as for instance in the broken phase of Φ^4). Potentials with perfect symmetric vacuum structure (i.e. with the same curvature at all the minima) can only be realized with non polynomial terms. If it is the curvature at the vacua which is responsible for the lifting of the degeneracy, designing a perfect symmetric vacuum structure one should obtain energy levels in the TCSA with a degeneracy equal to the number of vacua. This is what we have checked by engineering an ad-hoc potential, made of double Sine-Gordon model,

¹⁰It is important to stress that, although some of the minima could in principle be tuned in order to have equal second derivative, higher derivatives will be different and quantum corrections will discriminate between these minima at higher order.

with three perfectly equal minima, as shown in Fig. 1.21(c). The spectrum with three degenerate ground states is shown in Fig. 1.21(d). Above the three degenerate ground states in this case there are other six stable bound states, organized in two triplets.

Coming back to polynomial interactions, in principle there could be a *classical* LG potential leading to a desired number of degenerate *quantum* vacua but this implies a fine-tuning search in the coupling constant space, a task that is generally quite hard to fulfill¹¹.

Different story for the so-called LG picture proposed by Zamolodchikov [96] for the minimal models of CFT. First of all, in this case, the LG scheme is nothing else but a very useful bookkeeping of the number of relevant fields of the Kac table (which can be associated to the composite operators : $\sigma^m(x)$: of the most relevant operator $\sigma(x)$ of the theory), of their Z_2 parity and the overall fusion rules of the models. However, in all these minimal models it is present a very robust algebraic structure which ensures the right number of degenerate vacua once they are perturbed away from criticality (see Ref. [98] and references therein). In particular, for the minimal models associated to the LG $\sigma^{2(m-1)}$ and perturbed in the massive regime by the conformal field $\Phi_{1,3}$, it is the fusion rule of this operator that automatically gives rise to a theory which has $(m - 1)$ degenerate vacua.

1.10 The Derivative-method.

Supported by the promising results obtained for the massive free boson, we have extended the Fourier method to more complicated potentials, paying though a huge computational cost. Indeed, to describe faithfully even the ϕ^6 -double well potential, the number of primaries to be included in (1.147) grows significantly. Since we can keep only UV convergent primaries we need to take β very small, which results in an increased number of states to handle numerically.

To try to overcome this problem we have explored an alternative method to treat the perturbations. The starting observation is that the matrix elements can be formally written as

$$M_{ab}^{(m)} = (-i)^m \langle n, a_L, a_R | \partial_\gamma^{(m)} e^{i\gamma\phi} | n, b_L, b_R \rangle \Big|_{\gamma=0}. \quad (1.162)$$

In other words, we need to compute the matrix element with the generic operator of $e^{i\gamma\phi}$, then derive with respect to γ and finally set $\gamma = 0$. More details can be found in Appendix B. Clearly $e^{i\gamma\phi}$ does not belong to the operator content of the theory for generic γ , and the prescription relies on the assumption that all computations can be done as if it was an actual primary of the theory. In particular the commutator with modes is

¹¹It would be interesting to understand if this fine-tuned potential reproduces the correct physics of the expected corresponding massive phase or just the correct degeneracy of the ground state.

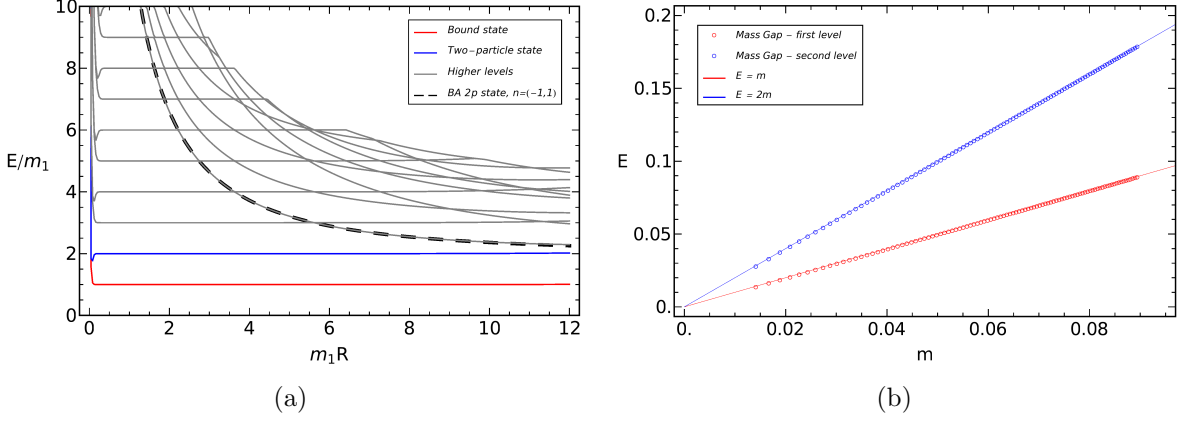


Figure 1.22: In panel (a) we show the energy levels with the ground state subtracted for the ϕ^2 perturbation, obtained within the derivative method. Here $\beta = 0.1$, $g_2 = 0.0004$, and $N_{\text{tr}} = 6$. The mass is given by $m = 2\sqrt{g_2} = 0.04$. The solid black line represents the (trivial) Bethe-ansatz prediction. In panel (b) we show the energy of the first two levels as function of $m = 2\sqrt{g_2}$. Their values are compared with the expected one of a free theory (here $m_1 R = 4$).

defined to be

$$[a_n, e^{i\gamma\phi}] \equiv -\gamma e^{i\gamma\phi}. \quad (1.163)$$

This assumption, even though is strictly formal, can be justified by the fact that we want to simulate the gaussian field of the LG theory. Imposing the commutation relation (1.163) includes a specificity of the gaussian field which could improve the agreement with the target theory. In the compactified theory indeed, the correct and straightforward definition of (1.163) would include a boundary term proportional to the Dirac delta which contributes to the matrix element and vanishes just in the infinite radius limit, $1/\beta \rightarrow \infty$ (for additional details see Appendix C).

We have compared the numerical results for the free ϕ^2 LG theory against those computed with the one obtained with the Fourier method, observing a significant improvement in precision. Within this derivative method, the low energy spectrum and the comparison with the Bethe-ansatz is shown in Fig. 1.22(a), while the first two mass gaps are plotted in Fig. 1.22(b) as function of the coupling $m = 2\sqrt{g_2}$. Data are stable for large regions in $m_1 R$ and the agreement with analytics is remarkable. Compared with the Fourier method, the derivative method performs even better. The spectrum is stable for a larger interval of $m_1 R$ and the two particle state by (trivial) Bethe-ansatz is better approximated.

However, despite this success with the free ϕ^2 potential, we have realized that this method cannot describe LG theories without further modifications. The reason is that normal ordering is not implemented in the derivative method as it is. Hence, each power of ϕ^{2n} is trivially commuting with ϕ^2 itself, and the unique element of non-commutativity

is at the level of $U(1)_1$ -modes. In the Fourier method, instead, the normal ordering is encoded in the R -dependent factors of eq. (1.147).

Since the derivative method performed so well with the Φ^2 theory, it would be interesting to extend it to higher power of the field ϕ in a way that keeps into account the correct normal ordering of operators.

1.11 Discussion on TCSA and Landau-Ginzburg theories.

In this paper we have studied the implementation of the TCSA to Landau-Ginzburg theories. The kinetic part of these theories is a conformal field theory but its spectrum is uncountable and this makes it not suitable for a direct TCSA-implementation. We overcame this problem by considering the conformal basis of the compactified boson, which is discrete and can be truncated by the introduction of a UV cutoff. In the limit where the compactification radius goes to infinity the original LG theory is recovered. The powers of the field $\phi(x)$ entering the potential are expressed in terms of their Fourier representation in the interval $[-\pi/\beta, \pi/\beta]$, so that matrix elements can be computed and the TCSA implemented. Due to the large number of Verma modules, we have improved the method implementing a Numerical Renormalization Group.

We obtained a good description of the free ϕ^2 LG theory, for which analytic predictions have been perfectly reproduced.

The method was then used to study the low energy neutral excitations of the Φ^4 and of the Φ^6 LG theories in their double well phase, where basic neutral excitations are breathers made of kinks and anti-kinks interpolating between the two vacua. The masses and consequently the number of stable bound states were estimated semiclassically in Ref. [46]; within all our simulations the semiclassical predictions are verified.

We furthermore observed that the quantum implementation of the LG theories with a classical set of vacua leads to a lift of their classical degeneracy. Indeed, while classical vacua are determined just by the minima, quantum corrections depend upon the shape of the potential in their vicinity. In particular, it is impossible to have, within LG theories, a potential whose multiple classical degenerate vacua share the same curvature, if there are more than two minima. However, this is markedly different from what proposed by Zamolodichikov [96] where underlying symmetries protect the correct degeneracy of ground states.

We furthermore explored an alternative procedure to compute the matrix elements of the LG perturbations, called derivative method, which performs remarkably well with

the Φ^2 LG theory. However, within this method the normal ordering of operators is not yet implemented. Hence, less trivial LG theories cannot be addressed at the moment, and the extension of the technique is an interesting perspective for future investigations.

Chapter 2

Quantum-statistics induced flow patterns in driven ideal Fermi Gas.

Based on arXiv:1306.0422v1.

Experimental advances in the rapid quenching and imaging of ultracold atoms [99, 100, 101, 102, 103, 104], as well as in the microscopy of nanoscale structures [105], make it possible to observe interesting effects of current-carrying systems with specific features attributable to their quantum nature. From the theoretical point of view, many predictions are available [101, 102, 103, 104, 105], also thanks to improvements in numerical methods. Most of these systems are characterized by an infinite number of states, and many techniques to reduce the cardinality of the spectra have been developed. Among these, as far as the spatial geometry of the system is important, a typical procedure is to discretize the system on a finite lattice¹.

In this second part of the thesis we discuss the role of Fermi statistics in the formation of new, experimentally detectable features in a two-dimensional ideal² Fermi gas which flows out of a small orifice into a large volume.

Differently from a classical ideal gas, which flows under the same conditions, and cannot develop any turbulence, the Fermi gas senses the Pauli exclusion and it is unknown which kind of flow should be expected. Indeed, the quantum statistics, acting as an analogue of an interaction, could result in significant modifications in the structure of the flow, which may exhibit fingerprints of the quantum nature of the gas.

The analogy between classical and quantum fluids is marked in the presence of strong interactions. Indeed, it has long been known – ever since the beginning of

¹Consider that, if the lattice has n -sites, the number of states in the theory is immediately reduced to n in the case of a single particle.

²Non-interacting.

quantum mechanics [106] – that interacting quantum fluids can be described in terms of the same hydrodynamic equations that describe classical interacting (viscous) fluids³ [25, 26, 27, 28, 29]. In fact, the many-body time-dependent Schrödinger equation is *exactly* equivalent to the equations of motion for the density and velocity field, namely the continuity equation and a hydrodynamic equation – albeit with an unknown stress tensor [106, 26, 23].

As any viscous fluid, interacting quantum liquids can exhibit a transition between laminar and turbulent flows when driven strongly. This has been shown, for instance, using the Density Functional Theory (DFT) for the electron liquid in Ref. [29, 23, 30]. In particular the flow of electrons out of a narrow constriction was studied while increasing the driving until turbulence sets up and unstable eddies are generated. Experiments on electron liquids to detect this phenomenon have been proposed [107, 108, 109]. For instance, in Ref. [108] it is suggested to measure the magnetic field generated by vortices of turbulent electrons.

Furthermore, it has been argued, that electronic systems close to quantum criticality are best suited to exhibit such turbulence, as they feature a small ratio of shear viscosity and entropy density; undoped graphene [107, 110] or cold atoms at unitarity above T_c [111] being probably the simplest such systems.

More specific effects in the flow of *quantum* fluids have been studied, both experimentally and theoretically [112, 113, 114, 115, 116, 117, 24], in the context of vorticity and turbulence in *superfluids*, focussing on dynamics and interactions of quantized vortices. The definition of turbulence in this last field is very different from what is called turbulence in the classical fluid. In classical fluids, indeed, the term usually refers to the development of chaotic patterns in the velocity field, while in the context of superfluids the word turbulence has a twofold meaning. The system is typically described by two interpenetrating fluids: a normal viscous fluid and a superfluid. While the dynamics of the normal viscous fluid is exactly that of a classical fluid and is described by Navier-Stokes' equations [24] (such that turbulence develops in the usual form), within the superfluid component quantum mechanics results in the formation of quantized vortices which interact and form a complicated tangle, to which the term quantum turbulence refers.

Another interesting aspect of *fermionic* quantum fluids has not received much attention so far. Complex flow patterns are generally attributed to the particles' interactions which generate non-linearity and chaoticity in the dynamics. It is therefore interesting to ask if, in absence of interactions, quantum statistics alone gives rise to non-trivial flows. With the advent of atomic gases where interactions among atoms can be tuned to essentially zero [101], the question whether the exclusion principle alone – a form of *collective* repulsion – may lead to interesting flow patterns, if the Fermi gas is driven out-of-equilibrium, can be tackled seriously.

³Namely, the Navier-Stokes' equations [24].

Non-trivial phenomena are known to arise in out-of-equilibrium flow of free fermions from recent works in $1d$ gases [118, 119, 120, 121], where the formation of shocks and interference ripples after a local quench was observed. The setup and the underlying physics is rather simple. A Fermi sea is deformed with a bump which is left free to evolve under a free Hamiltonian. The space displacement on top of the bump is much smaller than at the bottom such that, due to Heisenberg uncertainty, particles lying on the top have higher momenta and spread faster than those at the bottom. Hence, during the dynamics the shape of the bump deforms until the particles on the top overcome those at the bottom. This population inversion results in a series of shocks and ripples in the density. This effect is thus suggesting that even more interesting phenomena could develop in higher dimensions where richer patterns such as eddies or complex streamlines could form.

Moreover, already at equilibrium, Pauli exclusion alone leads to interesting interference phenomena in free fermions, such as Friedel oscillations [122], and one may expect even more complex patterns out-of-equilibrium. In particular Friedel oscillations develop, as a consequence of Fermi statistics, every time boundaries and/or some strong potential are present in the system. These oscillations are going to play a central role in our interpretation of the results presented in this Chapter.

We study the simplest case where some nontrivial flow is expected to develop as a consequence Fermi statistics: driven ideal fermions in restricted geometries in *two* dimensions. We show that they indeed develop non-trivial patterns in the vorticity (the curl of the current), which are manifestations of the Fermi statistics. Antiferromagnetic patterns are found not only in transients (unlike in the above-mentioned $1d$ studies), but also in the long-time steady state⁴. The latter should facilitate their observation in experiments, such as most recent transport measurements in cold atoms where constrictions as we consider here have been realized [103, 104]. Note instead that the ideal Bose gas, if prepared in a condensed state at $T = 0$, reduces to a single-particle problem, so that particular effects of “anti-exclusion” are absent. However, we recall that the case of free bosons is a pathological limit, which is likely to be modified by any weak interaction, as it alters the low energy spectrum and thus ensures superfluidity.

The setup we considered is shown in Fig. 2.1: a narrow channel (A) of width ϵ is connected to a much wider region (B) of width W , at $x = 0$. We study the system for values of W ranging from $W = 4\epsilon$ to $W = 20\epsilon$, and we are interested in the limit of very long regions, L . The choice of this geometry is motivated by simplicity and one of the simplest non-integrable geometries where nontrivial flows are expected to emerge is chosen. Moreover, geometries very similar to ours have been realized for instance in

⁴A steady state is a state where all observables of the system are invariant under translations in time.

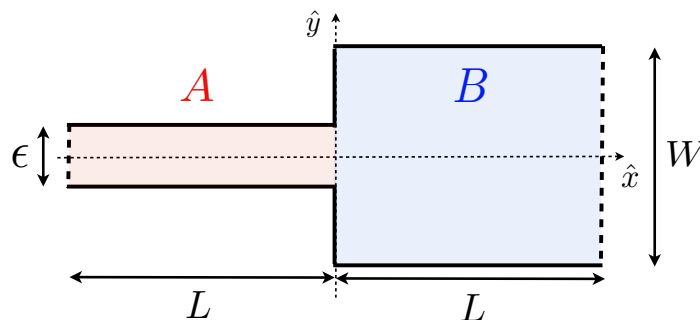


Figure 2.1: (Color online) Set-up studied: a narrow channel (A) is connected to a wide region (B). In the micro-canonical formalism the dashed boundaries are hard walls, while they represent external leads (Markovian baths) in the Lindblad approach. If the distance L from the junction to those boundaries is large enough, the vicinity of the orifice behaves as in an open system.

Ref. [103, 104] where two reservoirs containing $\sim 10^4$ atoms of fermionic ^6Li are put in contact with a very narrow channel ($\sim 20\mu\text{m}$) and a current is established between the reservoirs by preparing the two with an initial unbalancing in chemical potential.

In this Chapter, we analyze the dynamics and the steady state properties of the spatial density $\langle \hat{n}(x, y, t) \rangle$, of the current density $\langle \hat{\mathbf{J}}(x, y, t) \rangle$, and of the vorticity $\nabla \times \langle \hat{\mathbf{J}}(x, y, t) \rangle$ in the region close to orifice.

The computation of these observables for large L is numerically a prohibitive task. Therefore we approximate the system in two different ways that we assume to give similar results close to orifice. This assumption will be tested a posteriori.

We first study a closed system approximated on a lattice where we compute the above observables within the micro-canonical formalism [123, 124]. The dynamics is then followed until a quasi-steady state⁵ is formed. The second system is a driven open system coupled to external baths at $x = \pm L$. Again a lattice is introduced. The transport is studied by solving the Lindblad equation within what is called the “third quantization” formalism [37, 38]. Within this approach, we have direct access to the non-equilibrium steady state⁶ (NESS) properties.

In general, the steady state of the open system and the quasi-steady state that may establish in a closed system, are usually closely related, except near to the boundaries. In fact, the two approaches to transport are expected to be equivalent in the thermodynamic limit, if interactions and (potentially) impurity scattering induce thermalization

⁵We say that a closed system is in a quasi-steady state if, far from the boundaries, the system looks steady until reflections from the boundaries occur.

⁶A non-equilibrium steady state is a state that looks steady but some external work is done on the system.

and momentum randomization far from the junction.

However, for our system of non-interacting fermions the equivalence of the two methods is not guaranteed, since reflected waves from the contacts at $x = \pm L$ can coherently propagate back to the junction, in the NESS of the open system. Despite this caveat we found that the two approaches give quantitatively very similar results in specific regimes where reflections appear to be of minor importance. Moreover, in both cases the steady state seems to be determined by just two control parameters, which makes it reasonable to match the two descriptions. In other regimes instead, the agreement is just qualitative. Here we expect the micro-canonical approach to be a better description for a realistic system with weak but finite interactions, since it gives information about the system *before* reflections from boundaries occur. We therefore present our central results within this framework.

We will discuss in detail both formalisms, and, in particular, we will focus on differences and similarities between the two approaches.

2.1 The closed system: micro-canonical formalism.

The micro-canonical approach is used to describe a closed system in which the energy and the number of particles are both conserved. To build the closed system the dashed lines in Fig. 2.1 are replaced by solid lines which describe real walls. However, we are interested in the limit of large L where these boundaries will play no active role in the dynamics⁷, except for very late times, when some wave can be reflected.

The initial state ($t < 0$) is realized by preparing the set up in Fig. 2.1 with fermions of mass m in the ground state of the initial Hamiltonian

$$H_0 = -\frac{\hbar^2}{2m}\nabla^2 + V_{\text{in}}\theta(x), \quad (2.1)$$

where $\theta(x)$ is the Heaviside step function. The potential V_{in} lives in the box B and it determines how particles are distributed between the box A and B . This initial condition results in average densities \bar{n}_A and \bar{n}_B in regions A and B , respectively.

If $V_{\text{in}} = 0$, the resulting initial density has a flat profile and $\bar{n}_A = \bar{n}_B \equiv \bar{n}$. We care to choose $\bar{n}\epsilon^2 \gtrsim \frac{\pi}{4}$, otherwise there are no propagating modes in the channel A and the density is exponentially suppressed.

It is important to observe that the density in the box B , Fig. 2.2, is not uniform. Oscillations at the scale of the Fermi wavelength, usually called Friedel oscillations, are indeed present. This kind of features always appears in fermionic densities when bound-

⁷Although the boundaries at $\pm L$ do not influence the dynamics, as it will be clear later, a trace of these is present in the initial state.

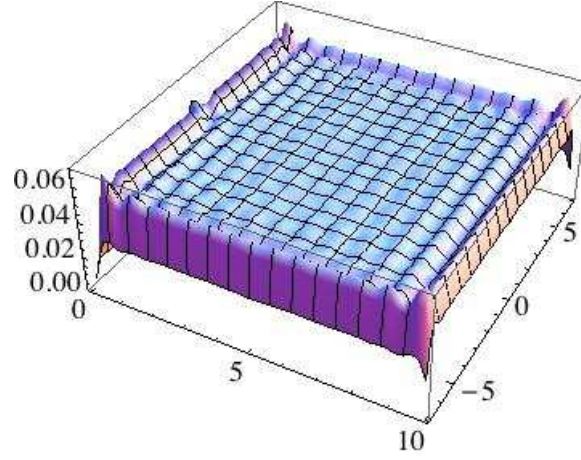


Figure 2.2: The spatial density in the box B before the quench: $\langle \hat{n}(x, y, t \leq 0) \rangle$. The Fermi surface is not uniform; Friedel-oscillations are visible.

aries are present.

If, instead, V_{in} is increased, the average density in the box B decreases until it vanishes for $V_{\text{in}} \rightarrow \infty$. In this regime, the gas is fully confined within the narrow channel A and we thus define $\bar{n} = \bar{n}_A$.

Within the two boxes A and B we define “effective chemical potentials” as those of Fermi seas with *uniform* densities $n_{A(B)}$:

$$\mu_{A(B)} = 4\pi \frac{\hbar^2}{2m} \bar{n}_{A(B)}. \quad (2.2)$$

Similarly, in the two extreme cases $V_{\text{in}} = 0$ and $V_{\text{in}} \rightarrow \infty$, we define a dimensionless parameter, $\bar{n}\epsilon^2$, an “effective chemical potential”

$$\mu = 4\pi \frac{\hbar^2}{2m} \bar{n}, \quad (2.3)$$

and an “effective Fermi wavelength”

$$\lambda_F = \sqrt{\frac{\pi}{\bar{n}}}. \quad (2.4)$$

These last two quantities are respectively the Fermi wavelength and the chemical potential of a Fermi sea with *uniform* density \bar{n} . Within the micro-canonical formalism, all the above definitions refer to the initial state.

We want to turn on a current from the narrow channel A to the large box B . This flow is realized by a sudden local quench. At $t = 0$, the Hamiltonian is abruptly changed

to a new one, which governs the time evolution for $t > 0$:

$$H = -\frac{\hbar^2}{2m}\nabla^2 + V_{\text{fin}}\theta(-x). \quad (2.5)$$

If $V_{\text{fin}} = 0$, the evolution is unbiased, and the flow is due to the difference between the chemical potentials in the two boxes: $\mu_A - \mu_B$ which is proportional to $\bar{n}_A - \bar{n}_B$. Hence, in the case $V_{\text{in}} = 0$ where $\bar{n}_A = \bar{n}_B$, there is no current flowing unless a finite V_{fin} is applied. Otherwise, if $V_{\text{fin}} > 0$ a current is established for any (non-negative) value of V_{in} .

To enlighten the effect of quantum-statistics in a clearer way, we compare the results obtained within two different protocols.

The first protocol, called *expansion into fermions*, is characterized by an equal average density all over the geometry in the initial state (obtained by fixing $V_{\text{in}} = 0$). At $t = 0$ the final potential, V_{fin} , of the order of the chemical potential $V_{\text{fin}} \approx \mu/2$, is turned on to push fermions out of the narrow channel A into the large box B . Under the influence of this bias, fermions are forced to exit from the narrow channel and to flow into a preexisting fermionic density whose profile is non-uniform because of Friedel oscillations (Fig. 2.2), induced by the boundaries.

In the second setting, called *expansion into free space*, the initial state is characterized by $V_{\text{in}} \rightarrow \infty$, and the gas is trapped in the small channel. At $t = 0$ the system is released and the gas is left free to expand into the empty region B ($V_{\text{fin}} = 0$).

These two protocols will be useful to clarify the role of Friedel-oscillations (and hence of Fermi statistics) in the resulting flows.

We compute the spatial density and the current density by projecting the initial state into the new eigenstates of the Hamiltonian H and computing the two observables as now explained.

The first important observation is that the initial wave function is a Slater determinant and, since both Hamiltonians are non interacting it remains so at all times. Hence it is enough to solve for the time-dependent single-particle eigenvalues and eigenfunctions before the quench and after:

$$\begin{aligned} H_0\psi_\alpha^{(0)}(x, y) &= E_\alpha\psi_\alpha^{(0)}(x, y), \\ H\psi_\beta(x, y) &= E_\beta\psi_\beta(x, y). \end{aligned} \quad (2.6)$$

The fermionic field operators before and after the quench are built as

$$\begin{aligned}\hat{\Psi}(x, y) &= \sum_{\alpha} \psi_{\alpha}^{(0)}(x, y) a_{\alpha}^{(0)}, \quad \hat{\Psi}^{\dagger}(x, y) = \sum_{\alpha} \psi_{\alpha}^{(0)*}(x, y) a_{\alpha}^{(0)\dagger}, \quad t \leq 0 \\ \hat{\Psi}(x, y) &= \sum_{\beta} \psi_{\beta}(x, y) a_{\beta}, \quad \hat{\Psi}^{\dagger}(x, y) = \sum_{\beta} \psi_{\beta}^{*}(x, y) a_{\beta}^{\dagger}, \quad t \geq 0\end{aligned}\quad (2.7)$$

with $\{a_{\alpha}^{(0)}, a_{\alpha'}^{(0)\dagger}\} = \delta_{\alpha, \alpha'}$, and $\{a_{\beta}, a_{\beta'}^{\dagger}\} = \delta_{\beta, \beta'}$. We define $\psi_{\beta}(x, y, t) \equiv e^{-iE_{\beta}t/\hbar} \psi_{\beta}(x, y)$, and the spatial density and current density for $t > 0$ can be computed as

$$\begin{aligned}\langle \hat{n}(x, y, t) \rangle &= \langle e^{iHt/\hbar} \hat{\Psi}^{\dagger}(x, y) \hat{\Psi}(x, y) e^{-iHt/\hbar} \rangle \\ &= \sum_{\beta, \beta'} \psi_{\beta}^{*}(x, y, t) \psi_{\beta'}(x, y, t) \langle g^{(0)} | a_{\beta}^{\dagger} a_{\beta'} | g^{(0)} \rangle.\end{aligned}\quad (2.8)$$

$$\begin{aligned}\langle \hat{\mathbf{J}}(x, y, t) \rangle &= \frac{\hbar}{2mi} \lim_{\mathbf{r} \rightarrow \mathbf{r}'} [\nabla_{\mathbf{r}} - \nabla_{\mathbf{r}'}] \langle e^{iHt/\hbar} \hat{\Psi}^{\dagger}(\mathbf{r}) \hat{\Psi}(\mathbf{r}') e^{-iHt/\hbar} \rangle \\ &= \frac{\hbar}{m} \Im \left[\sum_{\beta, \beta'} \psi_{\beta}^{*}(x, y, t) \nabla \psi_{\beta'}(x, y, t) \langle g^{(0)} | a_{\beta}^{\dagger} a_{\beta'} | g^{(0)} \rangle \right].\end{aligned}\quad (2.9)$$

where $|g^{(0)}\rangle$ is the ground state of H_0 . Using the completeness of eigenfunctions of H_0

$$\psi_{\alpha}^{(0)}(x, y) = \sum_{\beta} \Theta_{\beta\alpha} \psi_{\beta}(x, y), \quad \text{with } \Theta_{\beta\alpha} = \langle \psi_{\beta} | \psi_{\alpha}^{(0)} \rangle, \quad (2.10)$$

and imposing the continuity of the second quantized fermionic operators across the quench ($t = 0$), we can express a and a^{\dagger} in terms of $a^{(0)}$ and $a^{(0)\dagger}$ as

$$\begin{aligned}\hat{\Psi}(x, y) &= \sum_{\alpha} \psi_{\alpha}^{(0)}(x, y) a_{\alpha}^{(0)} = \sum_{\alpha} \left[\sum_{\beta} \Theta_{\beta\alpha} \psi_{\beta}(x, y) \right] a_{\alpha}^{(0)} = \sum_{\beta} \psi_{\beta}(x, y) \left[\sum_{\alpha} \Theta_{\beta\alpha} a_{\alpha}^{(0)} \right] \\ &= \sum_{\beta} \psi_{\beta}(x, y) a_{\beta}\end{aligned}\quad (2.11)$$

It follows that creation and annihilation operators after the quench can be written in terms of those before the quench as

$$a_{\beta} = \sum_{\alpha} \Theta_{\beta\alpha} a_{\alpha}^{(0)}, \quad a_{\beta}^{\dagger} = \sum_{\alpha} \Theta_{\beta\alpha}^{*} a_{\alpha}^{(0)\dagger} \quad (2.12)$$

and, considering that $a^{(0)}$ and $a^{(0)\dagger}$ are creators and annihilators on the initial vacuum $|g^{(0)}\rangle$, we arrive at

$$\langle g^{(0)} | a_{\beta}^{\dagger} a_{\beta'} | g^{(0)} \rangle = \sum_{\alpha\alpha'} n_{\alpha\alpha'} \Theta_{\beta\alpha}^{*} \Theta_{\beta'\alpha'}, \quad (2.13)$$

where the fermionic occupation number $n_{\alpha\alpha'}$ is $\delta_{\alpha\alpha'}$ if α is an occupied state ($\alpha \in \text{occ}$), 0 otherwise. The spatial density and the current density are thus computed for $t > 0$ to

be respectively:

$$\begin{aligned}\langle \hat{n}(x, y, t) \rangle &= \sum_{\alpha \in \text{occ}} \sum_{\beta, \beta'} \psi_{\beta}^*(x, y, t) \psi_{\beta'}(x, y, t) \Theta_{\beta\alpha}^* \Theta_{\beta'\alpha}, \\ \langle \hat{\mathbf{J}}(x, y, t) \rangle &= \frac{\hbar}{m} \Im \left[\sum_{\alpha \in \text{occ}} \sum_{\beta, \beta'} \psi_{\beta}^*(x, y, t) \nabla \psi_{\beta'}(x, y, t) \Theta_{\beta\alpha}^* \Theta_{\beta'\alpha} \right].\end{aligned}\quad (2.14)$$

The eigensystems (2.6) are solved numerically. In principle, both systems have an infinite number of eigenstates and we need a method to truncate this set to finite meaningful subsets. In the systems, where the geometry is naturally important, a standard method to reduce the number of states⁸ is to restrict the space to a lattice. The lattice is able to reproduce the main features of the geometry and results in a natural reduction of the dimension of the Hamiltonians to be linear in the number of sites. An important remark is that we always choose the lattice spacing, a , much smaller than the effective Fermi wavelength, $\frac{a}{\lambda_F} \ll 1$. Although this results in having many sites and thus a high computational cost, the above constraint must be considered in order to capture faithfully the features of the flow at the natural scale where Fermi statistics is expected to manifest, the Fermi wavelength itself.

With this in mind, we construct a discrete tight-binding Hamiltonian with a hopping strength $g = \frac{\hbar^2}{2ma^2}$, and we solve numerically the related finite-dimensional eigensystems to obtain the ingredients to use in Eq. (2.14). The dynamics is followed in the time window $\hbar/\mu \lesssim t \lesssim L/v_F$, where $v_F \approx \sqrt{2\mu/m}$, in order to exclude reflection effects from the dashed boundaries in Fig. 2.1. Within this times, the flow is rather stable close to the orifice, and a quasi-steady state seems to form, but for very weak time oscillations. This suggests that in an very long system a true quasi-steady state will establish at late times⁹. In Section 2.3 we are going to show that this is also confirmed by a different approach to the transport problem.

2.2 Physical results.

In this section we discuss the main physical results extracted by analyzing the flow of the ideal Fermi gas in the geometry of Fig. 2.1, within the micro-canonical formalism. The motivation of this choice is that, as it will be clear later, the micro-canonical formalism captures better than the Lindblad description the physics close to the orifice in the specific regimes where non-trivial features appear.

In the following, we show that two regimes, connected by a smooth crossover, are encountered upon increasing $\bar{n}\epsilon^2$. We refer to the regime at $\bar{n}\epsilon^2 \gg 1$, where the Fermi

⁸We remark that single particle Hamiltonians are diagonalized.

⁹Since it is a closed system, sooner or later revival effects will destroy the steady state.

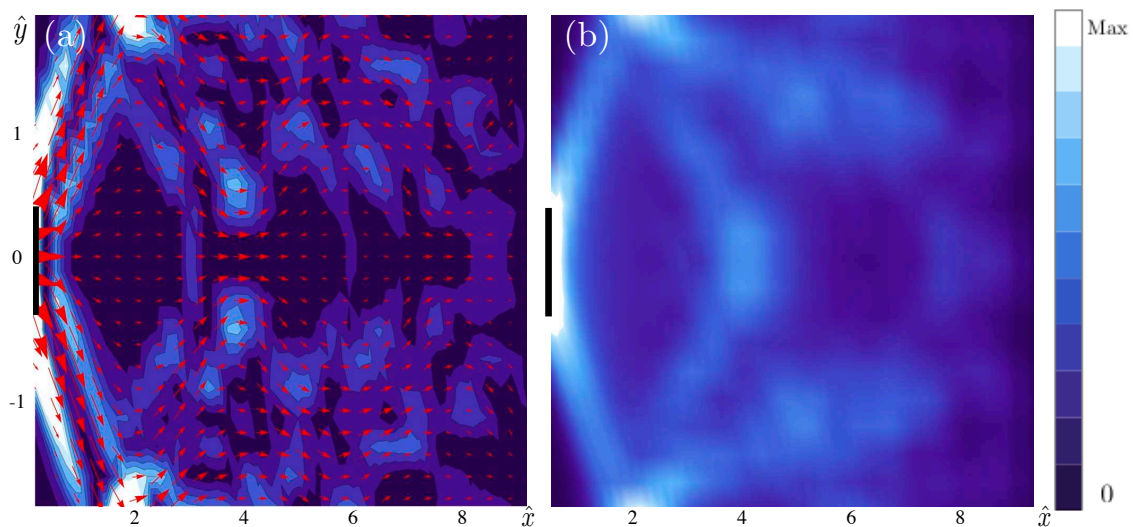


Figure 2.3: (a) The Current density \mathbf{J} and contour plot of $|\nabla \times \mathbf{J}|$ computed in the micro-canonical quasi-steady state, for $\bar{n}\epsilon^2 \approx 5$, at time $t \approx 16\hbar/\mu$. The protocol used is the *expansion into free space*, although the same current and vorticity pattern is recovered in the *expansion into fermions*, as far as the same $\bar{n}\epsilon^2$ is chosen with $V_{\text{fin}} \approx \mu/2$. (b) The spatial density corresponding to (a). Distances are measured in units of the orifice width ϵ (notice that the aspect ratio is 2:5). In all plots lighter colors correspond to larger values (linear scale)

wavelength is small with respect to the channel width ϵ , as **high-density** regime. Within this regime the flow develops in way which is simply understood by semi-classical diffraction theory. If $\bar{n}\epsilon^2 \sim 1$, instead, the Fermi wavelength is comparable with ϵ and the flow exhibits peculiar patterns that we show to be sensitive to quantum statistics (**low-density** regime).

At **high densities**, $\bar{n}\epsilon^2 \gg 1$, semi-classical diffraction is expected to hold. Indeed, as long as the Fermi wavelength is much smaller than the channel width ϵ , the flow is naturally more classical. Accordingly, we find a relatively simple steady state pattern. In this high density regime, the resulting flow does not depend on the protocol used, *expansion into fermions* or *expansion into free space*. For a representative choice of $\bar{n}\epsilon^2 \approx 5$ within the protocol of *expansion into free space*, the current density pattern and the absolute value of its vorticity ($|\nabla \times \mathbf{J}|$) are shown in Fig. 2.3(a), as well as the density pattern in Fig. 2.3(b).

The most prominent feature of the current pattern in Fig. 2.3(a), is a diffraction beam exiting from the orifice, whose angle is determined by the transverse momentum of the highest propagating band in channel A (here the second band). Those beams are reflected at $y = \pm W/2$ and give rise to two islands of intense vorticity around $(4\epsilon, \pm\epsilon/2)$. They are

thus simple boundary effects due to reflections at finite W , see also the density pattern in Fig. 2.3(b). The main characteristics of this regime is a rhomboidal region, of size $\sim W^2$, of very small and uniform vorticity centered at $(2\epsilon, 0)$.

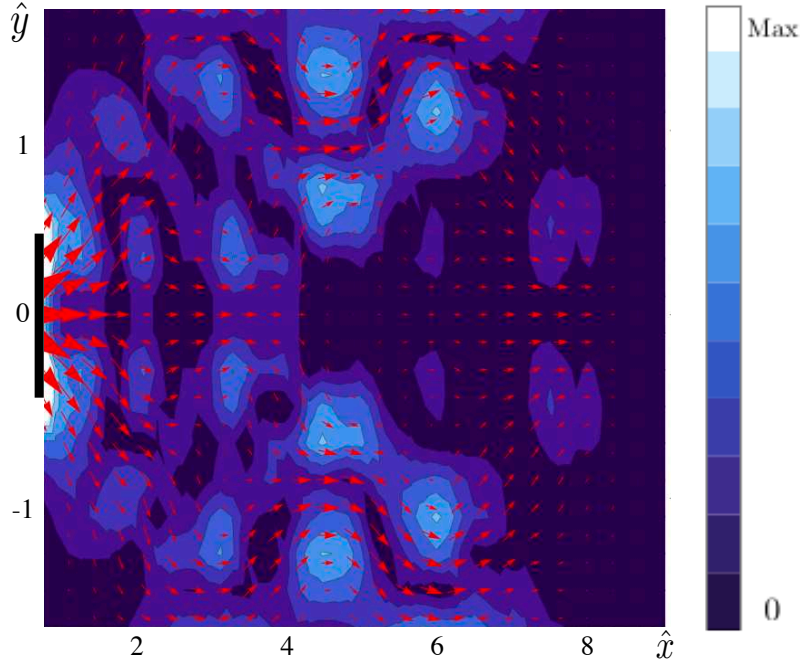


Figure 2.4: Current density \mathbf{J} and contour plot of $|\nabla \times \mathbf{J}|$ computed in the micro-canonical quasi-steady state, for $\bar{n}\epsilon^2 \approx 1.1$, at $t \approx 16\hbar/\mu$. Distances are measured in units of the orifice width ϵ (notice that the aspect ratio is 2:5).

The flow pattern is much more interesting at **low-density**, $\bar{n}\epsilon^2 \sim 1$, where quantum effects are more pronounced. In this regime and within the protocol *expansion into fermions*, additional structures – of the size of the Fermi wavelength $\sim \frac{1}{\sqrt{\bar{n}}}$ – develop in the current and vorticity within the interior of the rhomboidal region, which was nearly vorticity-free at high-density. In Fig. 2.4, we show the current and vorticity computed at time $t \approx 16\hbar/\mu$, before reflections at $x = \pm L$ occur. We stress that the quench parameters were $V_{\text{in}} = 0$ and $V_{\text{fin}} \approx \mu/2$, i.e., a strong bias is suddenly applied to fermions prepared in their ground state with average spatial density \bar{n} all over the geometry (*expansion into fermions*).

The resulting current pattern exhibits zig-zag shaped stream-lines and thus differs markedly from the semi-classical diffraction observed at high-density. Note that here the islands of vorticity close to the orifice ($x < 4\epsilon$) seem *not* to be simply due to reflection from the boundaries at $y = \pm W/2$, but, as we will show below, should rather be interpreted as patterns induced by the (Friedel) density oscillations present in the steady state due to the lateral confinement. Interestingly the vorticity pattern remains qualitatively similar

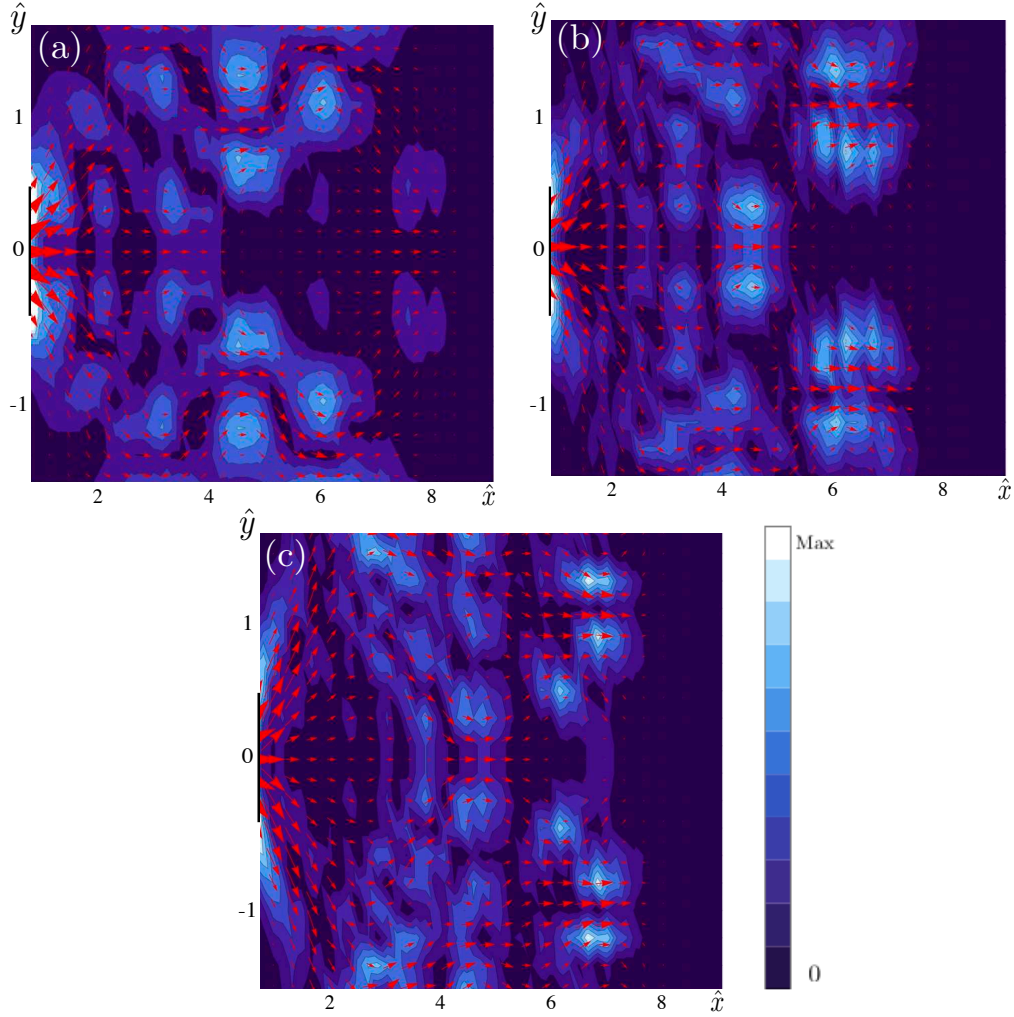


Figure 2.5: Current density \mathbf{J} and contour plot of $|\nabla \times \mathbf{J}|$ computed in the micro-canonical quasi-steady state, for increasing density. For (a) $\bar{n}\epsilon^2 \approx 1.1$, (b) $\bar{n}\epsilon^2 \approx 2.2$, and (c) $\bar{n}\epsilon^2 \approx 4.8$. Distances are measured in units of the orifice width ϵ (notice that the aspect ratio is 2:5). In all plots lighter colors correspond to larger values (linear scale)

if the boundary conditions are changed¹⁰. We stress that, once formed, these non-trivial patterns are remarkably stable in time, but for very weak oscillations in time. As it will be discussed in the Section 2.3.3, we believe that at late times, in a long enough system, these oscillations vanish.

An interpretation of this peculiar flow can be extracted from Eq. (2.14). Indeed, even though Eq. (2.14) states that the current density is simply the superposition of single-

¹⁰In Appendix E the role of boundary conditions is discussed

particle contributions, the resulting pattern is highly non-trivial, as propagating states superpose, each with their individual interference patterns. The higher the initial density the larger is the number of superposed modes, which tends to smoothen the interference patterns. Therefore, while interesting patterns survive for low-density $\bar{n}\epsilon^2 \gtrsim \pi/4$, in the limit $\bar{n}\epsilon^2 \rightarrow \infty$ we expect to recover the classical limit where all non-trivial features are smeared out. Within the protocol *expansion into fermions*, simulations confirm this trend, as we present in Fig. 2.5, where the current patterns obtained for increasing densities are shown. In the figure non-trivial structures clearly emerge at low-density and tend to vanish when $\bar{n}\epsilon^2$ is increased.

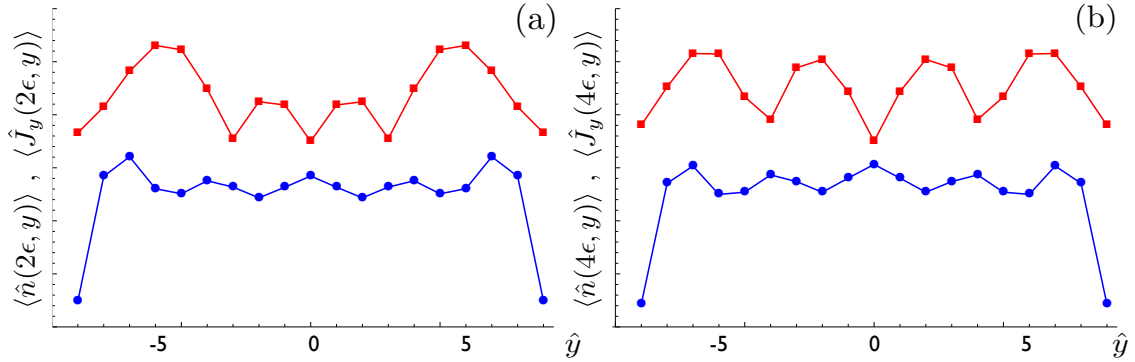


Figure 2.6: The spatial density (blue) and the y -component of the current density (red) profiles along two transverse sections of the geometry: (a) $x \approx 2\epsilon$ and (b) $x \approx 4\epsilon$. The setting is that of Fig. 2.4, the values of the curves are rescaled to simplify the comparison between the two. The y -coordinate is measured in unit of ϵ .

If the region B is non-empty, the Pauli exclusion leads to Friedel oscillations. We push the idea that these density oscillations play a crucial role in the formation of the observed vorticity patterns. Indeed, an evident anti-correlation is established between the density profile for different transverse sections of the geometry¹¹ and the absolute value of the y -component of the current¹² shown in Fig. 2.6. From a pictorial point of view, we interpret the above anti-correlation in the following way. Particles flowing from the narrow channel to the box B , are forced to find their path in the landscape of hills and valleys produced by Friedel oscillations of the non-uniform density of fermions. Since the hills of this landscape represent the regions where fermions are denser, because of the exchange interaction they oppose to the incoming flow with stronger statistical repulsion than the valleys, which are favored by incoming particles. As the density is increased, the Fermi wavelength decreases, the Friedel oscillations become weaker, and the zig-zag trajectories of particles become gradually less marked until vanish and just the semi-classical flow –

¹¹We define transverse section a section of the geometry at fixed x .

¹²The current is restricted to the same transverse section than the density.

observed in the **high-density** regime – survives.

To be more quantitative, we introduce the dimensionless parameter

$$\chi \equiv \frac{\lambda_F \nu}{\bar{J}_\epsilon}, \quad (2.15)$$

where ν is the average vorticity at $x \approx 2\epsilon$, the Fermi wavelength λ_F is the typical scale of the patterns and \bar{J}_ϵ is the average current density at the orifice. χ estimates the relevance of non-trivial patterns in a flow with given intensity. Increasing the density \bar{n} and/or the lateral size W of the box B we find that

$$\chi \sim \frac{1}{\sqrt{\bar{n}\epsilon}} \frac{1}{\sqrt{\bar{n}W}} \sim \frac{\lambda_F}{\epsilon} \frac{\lambda_F}{W}. \quad (2.16)$$

We remark that Friedel oscillations become less intense if \bar{n} and/or W are increased, so that the observed trend for χ links the intensity of Friedel oscillations with that of the observed patterns.

We thus conjecture that the formation of non-trivial patterns in the vorticity at low density ($\bar{n}\epsilon^2 \sim 1$) is caused by the non-uniform fermionic density present in the box B . To verify our hypothesis, we compare the current-density and vorticity pattern obtained in both protocols *expansion into fermions* and *expansion into free space* within the **low-density** regime (Fig. 2.7). The box B used for this comparison is characterized by $W = 14\epsilon$, in order to be sure that interference with the boundaries at $y = \pm W/2$ does not play any role.

In Fig. 2.7(a) the protocol is the *expansion into fermions* ($V_{\text{in}} = 0$, and $V_{\text{fin}} \approx \mu/2$), and the fermions pushed into the large box B are sensitive to the preexisting fermionic density and the flow manifests non-trivial vorticity patterns.

In Fig. 2.7(b) the setting is $V_{\text{in}} \rightarrow \infty$ and $V_{\text{fin}} = 0$ (*expansion into free space*). The large box B in the initial state is empty, and, after the quench, the gas expands freely out from the channel A , with a bias of the order of the chemical potential. As it can be seen, the absence of the initial fermionic density into the box B results in the absence of vortices in the current-density pattern close to the orifice. Also, the zig-zag patterns in the current density are absent and the vorticity exhibits the same semi-classical structure found at high density. This supports the conjecture that Friedel oscillations play an important role in the formation of vorticity-patterns. Again in the **high-density** regime the Fermi wavelength is small and consequently also Friedel oscillations are weak such that just the semi-classical picture emerges.

Further differences between the two protocols can be found. In Fig. 2.8(a) we show – for the *expansion into fermions* of Fig. 2.7(a) – the average vorticity along each transverse section. Similarly, we show the quasi-steady total current along transverse sections

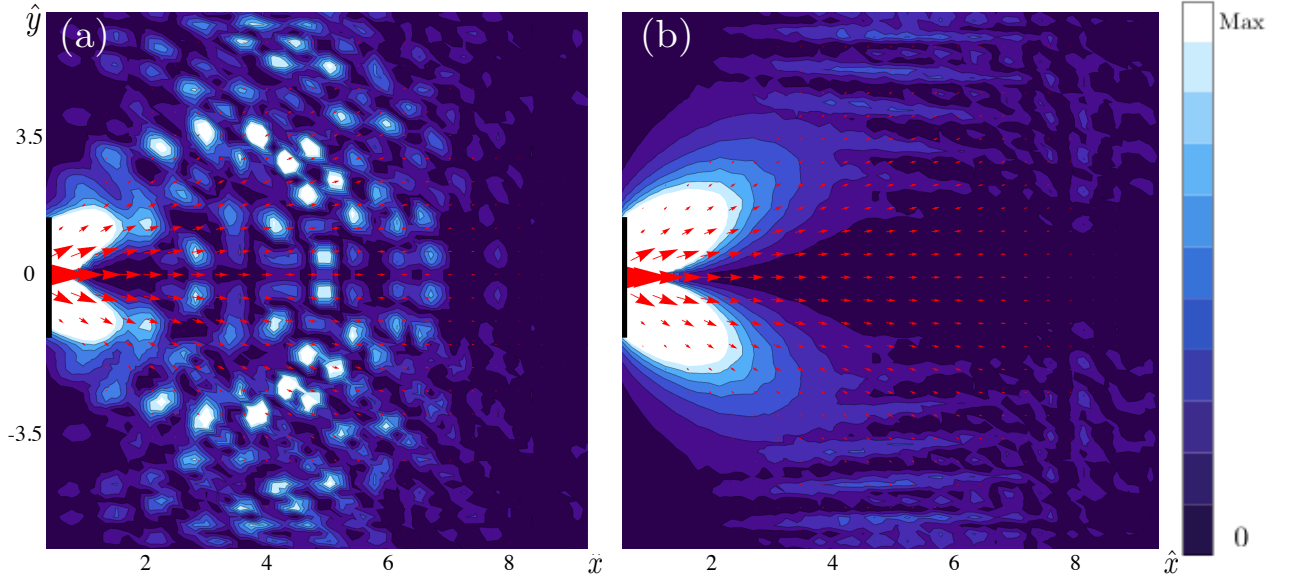


Figure 2.7: (a) The current density pattern and the intensity of the corresponding vorticities are shown for $\bar{n}\epsilon^2 \approx 1.3$ in the micro-canonical quench-protocol (snapshots are taken at time $t \approx 16\frac{\hbar}{\mu}$): (a) $V_{\text{in}} = 0$ (roughly homogeneous initial density), $V_{\text{fin}} \approx \mu/2$ applied to region A; (b) expansion into empty space, $V_{\text{in}} \gg 1$ (region B initially empty), $V_{\text{fin}} = 0$. The vorticity patterns in the two cases are evidently very different. In particular, in the case (b) of the expansion into the initially empty region B , there is no evidence of non-trivial features in the current flow and vorticity close to the orifice, in contrast to case (a). Finite density in region B and the associated steady state Friedel-like oscillations are conjectured to be important for the formation of non-trivial flow patterns. In both cases, we chose $W = 14\epsilon$ so that the boundaries at $\pm W/2$ are rather far from the orifice and the difference between the two quench protocols is evident. The color code is the same for both figures. Note the aspect ratio of 7:5 of the axis scales.

(shown in Fig. 2.8(b)). It appears that, at the time $t = 16\hbar/\mu$, the quasi-steady state is established up to $x \approx 6.5\epsilon$, except for small time oscillations¹³. In the region $2\epsilon < x < 6\epsilon$, the average vorticity is characterized by an almost non-decreasing plateau which corresponds to the region where non-trivial patterns are present.

In Fig. 2.8(c) it is shown the average vorticity along transverse sections for the *expansion into free space* – corresponding to Fig. 2.7(b) – with total current shown in Fig. 2.8(d). It is manifest that, in the absence of a substantial fermionic density in B , the average vorticity decreases smoothly with the distance from the orifice. This can also be seen from the featureless flow shown in Fig. 2.7(b).

If $W \gg \epsilon$, vortices of size λ_F form in the current density just outside the orifice, in

¹³We expect these oscillations to vanish at late time in a long enough system.

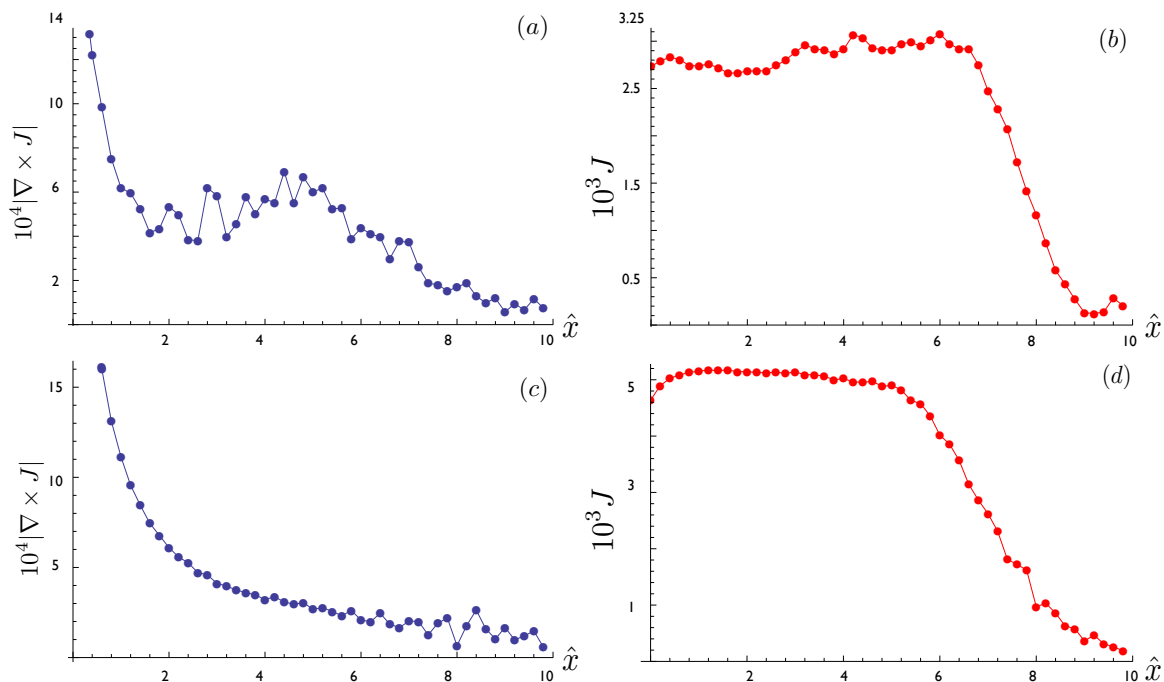


Figure 2.8: The average absolute value of the vorticity (a) and the total current (b) along a transverse section for the flow patterns in Fig. 2.7(a). The average absolute value of the vorticity (c) and the total current (d) along a transverse section of the flow patterns in Fig. 2.7(b).

the region where the flow is less intense (Fig. 2.9). This feature remains stable if periodic boundary conditions are considered.

We interpret the emergence of vortices in the current-density as a fingerprint of quantum-statistics. Indeed, in the absence of interaction, there is no mechanism able to invert the sign of the velocity. Differently, an ideal Fermi gas senses an effective “statistical pressure” due to the fermions present in the large volume B . This effective repulsive interaction seems to be at the basis of the velocity inversion. The vortices occur in the region where the flux in the x -direction is less intense and the statistical-pressure overcomes the inertia of the gas. Moreover, we verified that these features are not present in simple diffraction theory (within the Kirchhoff approximation).

If W is small, vortices have not enough space to form, and cannot develop.

Our understanding of the results obtained within the protocol *expansion into fermions* at **low-density**, $\bar{n}\epsilon^2 \sim 1$ is that, if the density profile is non-uniform, we should expect non-trivial patterns in the vorticity. Hence, non-trivial features, such as vorticity patterns, may be detectable in experiments where dilute atoms are confined in finite volumes, as an effect of the Friedel oscillations. Moreover, Friedel oscillations are present whenever

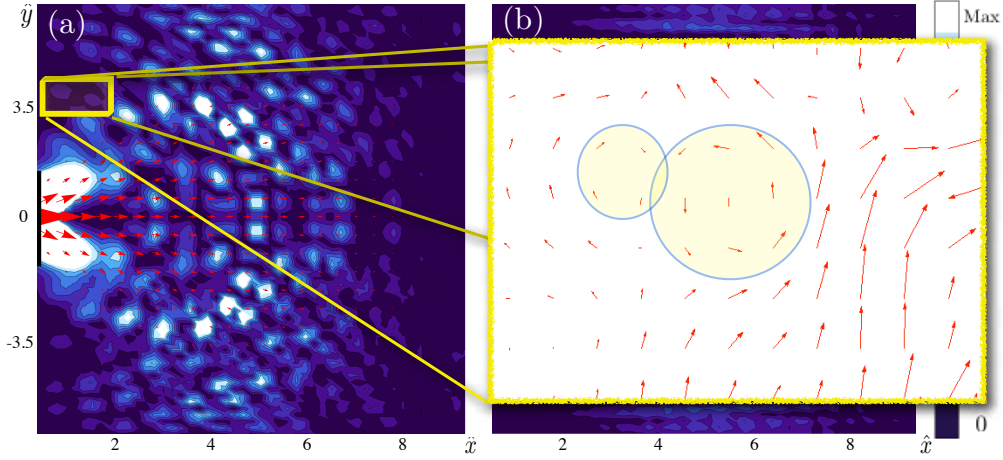


Figure 2.9: A detail of the vortices formed in the current density in the set-up of Fig. 2.7(a).

strong disorder is present. It is therefore important to ask whether such features have an experimentally detectable intensity or not.

If the fermions are charged, such as in a 2d electron gas (which may still be considered weakly interacting in the presence of a strong dielectric) a complex current pattern, for instance that of Fig. 2.5(a), generates a non-trivial magnetic field distribution.

In the considered geometry, and at strong driving ($V_{\text{fin}} \sim \mu$), typical magnetic moments associated with the circulation patterns are of the order of a tenth of a magneton $\mu = \frac{e\hbar}{2m}$, that is, in principle, an experimentally accessible intensity. Interestingly, the vorticity maxima organize in a short-range correlated antiferromagnetic pattern, which realizes an out-of-equilibrium *staggered* orbital flux state, cf. Fig. 2.10, reminiscent of equilibrium *staggered* flux phases proposed in strongly correlated 2d systems [134, 135]. Similar patterns arise from currents of magnetically (electrically) polarized neutral atoms. The electric (magnetic) fields due to such moving dipoles is proportional to a derivative of the field pattern of Fig. 2.10 (see Appendix F), but may be too weak to be detected by current detection means. It may be interesting to look for similar patterns in systems with spin-orbit coupling, e.g., in cold atoms.

Apart from the currents, the density patterns computed in this system could be measured experimentally by resonant light absorption in atomic gases in optical lattices. The limiting resolution is currently ~ 660 nm [136], which is smaller than typical Fermi wavelengths in those systems, and as anticipated, the set-up discussed here has already been realized in recent experiments [103, 104].

We conclude this Section by discussing the scaling of the intensity of local magnetic

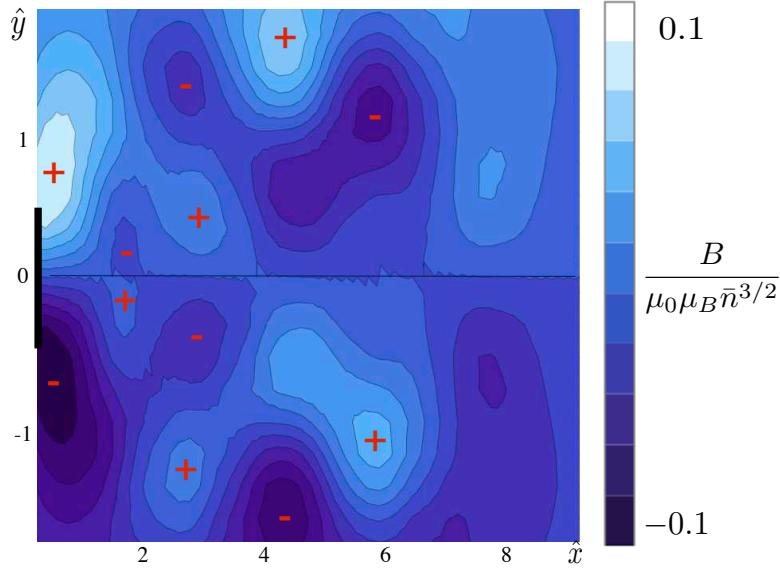


Figure 2.10: The z -component of the magnetic field generated by a charged current flow as in Fig. 2.4: The quasi-steady state exhibits a *staggered* flux close to the orifice. Distances are measured in units of the orifice width ϵ (note that the aspect ratio 2:5). In all plots lighter colors correspond to larger values (linear scale).

moments in the vorticity patterns when the lateral side of the box B (W) is enlarged. In Fig. 2.11 it is shown that the intensity decreases as W increases. This is expected and can be explained by the fact that the strength of Friedel oscillations decreases – when W increases – as $\frac{1}{W}$. However, we stress that every experiment where trapping or confinement are present is likely to exhibit the non-trivial features we found.

We realized that Friedel oscillations induce non-trivial patterns in the vorticity of ideal fermions out of equilibrium at low density. For charged electrons, the intensity of these features is in principle measurable, and the dynamics appears quasi-steady within the micro-canonical formalism. Whether a non-equilibrium steady state is expected to form at late times is discussed in the next Section.

2.3 The open system: Lindblad equation.

In order to directly probe the non-equilibrium steady-state (NESS) and confirm that the micro-canonical results indeed capture steady properties close to the orifice, we consider again the set-up of Fig. 2.1, but with the dashed boundaries representing couplings to external driving Markovian baths. In this framework the large- L system is approximated by two external baths at different chemical potentials which interact with the system by injecting and extracting particles. Such an open system is conveniently described in

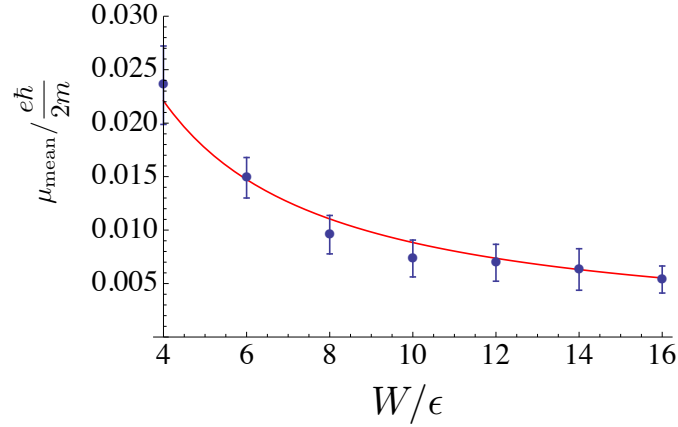


Figure 2.11: The average magnetic moment in units of the magneton $\frac{e\hbar}{2m}$ generated by non-trivial vorticity patterns close to the orifice ($x < 4\epsilon$) for $\bar{n}\epsilon^2 \approx 1.2$ within the protocol *expansion into fermions*. The red line is the fit $\mu_{\text{mean}} / \frac{2\hbar}{2m} = \frac{a}{W}$ with $a = 1.08 \pm 0.05$.

terms of the density matrix $\rho(t)$, since all the observables at time t can be computed as

$$\langle \mathcal{O} \rangle_t = \text{Tr } \mathcal{O} \rho(t). \quad (2.17)$$

The time evolution of this *open* quantum system is thus governed by the quantum master equation for the density matrix, called Lindblad equation [23, 36, 37, 38],

$$\frac{d\rho}{dt} = \hat{\mathcal{L}}\rho := -\frac{i}{\hbar}[H_0, \rho] + \sum_{b,y} (2L_y^b \rho L_y^{b\dagger} - \{L_y^{b\dagger} L_y^b, \rho\}). \quad (2.18)$$

The trace and positivity of ρ is preserved by construction of the Liouvillian, $\hat{\mathcal{L}}$, which is restricted to be quadratic. The dynamics is non unitary since it is restricted to the considered sub-system, neglecting that of the baths¹⁴. We directly formulate a discrete version of the problem on a lattice with spacing a and hopping amplitude $g = \frac{\hbar^2}{2ma^2}$. The lattice is made of n fermionic sites.

The Lindblad operators L_y^b , are chosen to be linear in the fermions, and represent the coupling at coordinate y on boundary $b \in \{A, B\}$ to independent baths. To describe driving from A to B we choose $L_y^A = \sqrt{\Gamma_A} c^\dagger$ ($x = -L, y$) and $L_y^B = \sqrt{\Gamma_B} c$ ($x = L, y$), where c^\dagger, c are creation and annihilation operators, respectively. Hence the thin channel A is coupled at $x = -L$ to an external bath which can inject particles in the system with rate Γ_A , while the large box B is coupled at $x = L$ to a bath that extracts particles with rate Γ_B . Sites coupled to the external baths are called in the following *boundary-sites*.

¹⁴The dynamics of the full system (system plus environment) is unitary.

We are interested in the NESS-density matrices $\{\rho_{NESS}\}$ which are described by the equation

$$\hat{\mathcal{L}}\rho_{NESS} = 0.$$

The problem of determining the non-equilibrium steady states (and how many there are) amounts to the computation of the kernel of the Liouvillian. The operator, however, is exponentially large in the number of sites n , and the solution of Eq. (2.3) is numerically hard.

The complexity of the problem can be significantly reduced, and eventually analytically solved, through the method of third quantization [37, 38].

The essence of this method lies in identifying the existence of a 2^{2n} dimensional linear vector space, called the Liouville-Fock operator space of which the density-matrix $\rho(t)$ is a member. This operator space has a natural fermionic structure exploited by creation (\hat{c}^\dagger) and annihilation (\hat{c}) operators satisfying the canonical anti-commutation relations, $\{\hat{c}_i, \hat{c}_j^\dagger\} = \delta_{ij}$, and being Hermitian adjoints of each other (see Appendix G). The Liouvillian $\hat{\mathcal{L}}$ can be cast as a quadratic form in these fermionic operators defined in the Liouville-Fock space, and reads as,

$$\hat{\mathcal{L}} = -2\hat{\underline{c}}^\dagger \cdot (2i\mathbf{H} + \mathbf{M} + \mathbf{M}^T)\hat{\underline{c}} + 2\hat{\underline{c}}^\dagger \cdot (\mathbf{M} - \mathbf{M}^T)\hat{\underline{c}}, \quad (2.19)$$

where \mathbf{H} is the $2n \times 2n$ Hamiltonian matrix, \mathbf{M} is a $2n \times 2n$ complex Hermitian matrix parametrizing the baths operators, and $\hat{\underline{c}}$ or $\hat{\underline{c}}^\dagger$ denotes a vector (column) of the $2n$ fermionic operators.

The above given representation of the Liouvillian admits a further simplification (reduction) through a linear transformation of the set of \hat{c} and \hat{c}^\dagger operators to new operators given by,

$$\hat{a}_{1,i} = \frac{1}{\sqrt{2}}(\hat{c}_i + \hat{c}_i^\dagger), \quad \hat{a}_{2,i} = \frac{i}{\sqrt{2}}(\hat{c}_i - \hat{c}_i^\dagger), \quad (2.20)$$

where the $\hat{a}_{1,i}$ and $\hat{a}_{2,i}$ with $i = 1, 2, \dots, 2n$ represent $2n$ Hermitian Majorana operators satisfying the canonical anti-commutation relation,

$$\{\hat{a}_{\alpha,i}, \hat{a}_{\beta,j}\} = \delta_{\alpha,\beta}\delta_{i,j}, \quad \alpha, \beta = 1, 2, \quad i, j = 1, \dots, n. \quad (2.21)$$

in terms of which the Liouvillian can be recast as,

$$\hat{\mathcal{L}} = \hat{\underline{a}} \cdot \mathbf{A}\hat{\underline{a}} - A_0\hat{\mathbb{I}}. \quad (2.22)$$

Here, \mathbf{A} is a complex anti-symmetric $4n \times 4n$ matrix, referred to as the *structure matrix*, having the following form,

$$\mathbf{A} = \begin{pmatrix} -2i\mathbf{H} + 2i\mathbf{M}_i & 2i\mathbf{M} \\ -2i\mathbf{M}^T & -2i\mathbf{H} - 2i\mathbf{M}_i \end{pmatrix} \quad (2.23)$$

where \mathbf{M}_i is the imaginary part of the bath matrix \mathbf{M} , which encodes the *driving*. The constant $A_0 = 2(\text{Tr}\mathbf{M}_r)$, with \mathbf{M}_r being the real part of the bath matrix \mathbf{M} encoding the *dissipation*.

The eigenvalues of \mathbf{A} , called *rapidities* and labeled by β 's, always come in pairs of $+\beta$ and $-\beta$. An interesting consequence, is that one set of eigenvalues, say $+\beta$'s, can be obtained as the eigenvalue spectrum of a reduced $2n \times 2n$ *real* matrix (see Appendix H), henceforth called \mathbf{X} , and given by,

$$\mathbf{X} = -2i\mathbf{H} + 2\mathbf{M}_r, \quad (2.24)$$

and the complete spectrum of \mathbf{A} is recovered as the *union* of the spectrum of \mathbf{X} and -1 times the same spectrum.

It is worth noting that the complexity of the central problem of obtaining the spectrum of the Liouvillian operator has been considerably reduced. Namely, from an exponential one, involving diagonalizing a $2^{2n} \times 2^{2n}$ matrix, to a polynomial one, which amounts to diagonalize a $4n \times 4n$ complex matrix, and finally to diagonalizing a $2n \times 2n$ real matrix. Herein lies the power of the method of third quantization in studying open quantum systems.

The eigenvalues of the structure matrix \mathbf{A} have an important physical interpretation, first and foremost, the non-equilibrium steady state of the Lindblad equation is *unique* if and only if $\text{Re } \beta > 0$ for all β 's. Whence, it follows that upon starting from an arbitrary initial state, this will evolve in time to the non-equilibrium steady state. The corresponding rate of exponential relaxation is determined by the real part of the smallest eigenvalue. Finally, and most importantly, the complete set of quadratic correlations in a unique steady state is given by¹⁵,

$$\text{Tr } w_i w_j \rho_{\text{NESS}} = \delta_{i,j} + 4iZ_{i,j} \quad (2.25)$$

where, the matrix \mathbf{Z} is obtained as a solution of the Lyapunov equation,

$$\mathbf{X}^T \mathbf{Z} + \mathbf{Z} \mathbf{X} = \mathbf{M}_i, \quad (2.26)$$

It is worth mentioning that not only quadratic but in fact any n -point function can be obtained by exploiting Wick's theorem. We therefore have constructive formulas to access the spatial density and current density in the NESS, which turns out to be unique, in our system.

¹⁵This can be proven by implementing the set of transformations from the initial Majorana-fermions $\{w\}$ to $\{c, c^\dagger\}$ and finally to $\{a, a^\dagger\}$.

2.3.1 The physics of the open system.

Using the third-quantization formalism we can compute the density and the current density easily. In the micro-canonical approach the control parameters on the system are the number of particles N and potentials $V_{\text{in/out}}$. In contrast, in the Lindblad description the control parameters are the bath rates $\Gamma_{A,B}$.

In both formalisms the two control parameters determine in the steady state an average spatial density \bar{n}_B in the box B ¹⁶, and total current J through a transverse section¹⁷. Therefore we can try to match the resulting flows close to the orifice within the two approaches by comparing these last quantities. This procedure relies on the assumption that both the quasi-steady state of the micro-canonical formalism and the non-equilibrium steady state of the driven open system are similar close to the orifice. Moreover, in both approaches, we believe that the family of steady states – obtained within the geometry of Fig. 2.1 – can be described by just two parameters, as those we are using for the matching.

In Fig. 2.12 we show the total current along an arbitrary transverse section and the average spatial density of the NESS obtained for different $\Gamma_{A,B}$. We will compare – close to the orifice – the resulting flows for different bath-rates with that obtained within the micro-canonical formalism, imposing that the average density \bar{n}_B and total current J in the box B are matched within the two descriptions. As discussed below, in specific regimes the agreement is even quantitative.

In Fig. 2.12(a) the total current is shown. It is evident that the total current is non-monotonic with the strength of the coupling. The maximum is for both Γ_A and Γ_B comparable to the strength of the hopping g , while the current goes to zero, if one of the two bath-rates becomes large. This phenomenon is known in the literature as *negative differential conductance* [125, 126, 127, 128, 132, 133].

In Fig. 2.13 we plot the section of Fig. 2.12(a) marked by the red dashed line. The maximum of the total current, as anticipated, is found for $\Gamma_{A,B} \sim g$. This can be explained by the fact that, if a new particle is injected into a boundary-site, it requires the typical time $t^* \sim \frac{\hbar}{g}$ to propagate to one of the nearest neighbor sites. Therefore, while for $\Gamma_{A,B} < g$ increasing the injection rate results in an higher total current, when $\Gamma_{A,B} \gtrsim g$ the boundary sites are occupied with high probability and new particles cannot be injected easily. A simple modification of the previous argument applies to the case of

¹⁶Within the micro-canonical formalism for the protocol *expansion into fermions* the value \bar{n}_B computed on the steady state is very similar to that computed in the initial state. This is because the fraction of fermions flowing into B is negligible with respect to that of fermions already present in the volume.

¹⁷Within the micro-canonical description the section must be taken close to the orifice, where reflections form boundaries are not important, and the measurement must be restricted to times where the flow is quasi-steady.

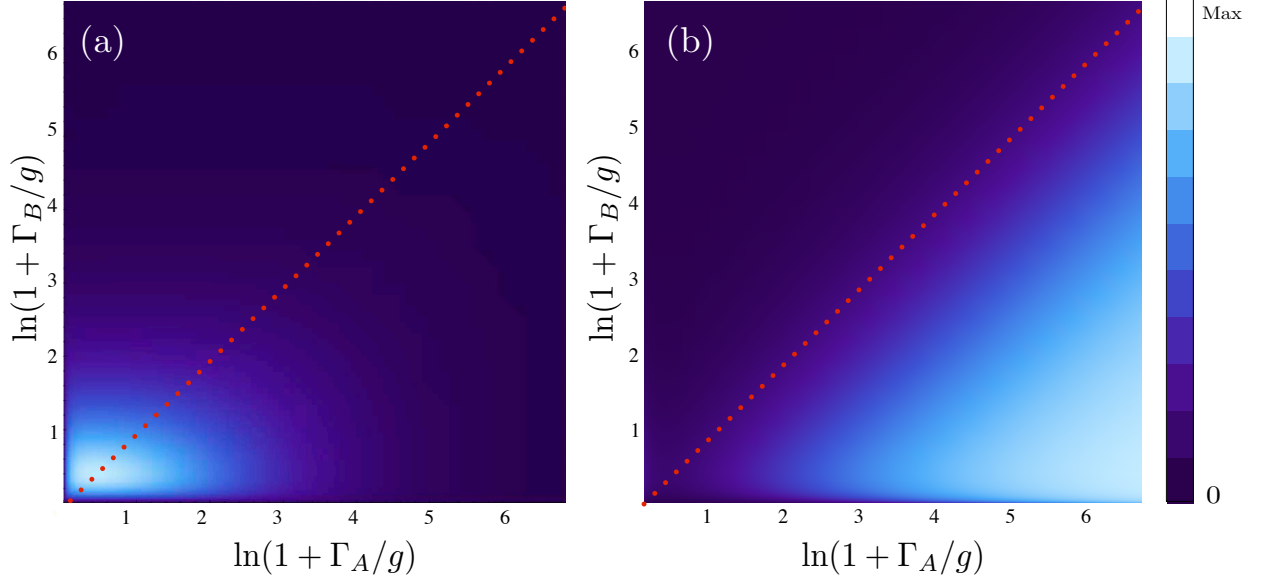


Figure 2.12: The total current (a) and the average spatial density (b) for different values of the bath-rates.

the extraction of particles from the system.

Although this observation justifies that the current is no longer increasing when the rates are bigger than the hopping, it does not explain the $1/\Gamma_{A,B}$ behavior measured at large $\Gamma_{A,B}$. In Section 2.3.2 we will understand this feature in terms of the so called quantum Zeno effect [129, 130, 131], for a simple two-site system.

In Fig. 2.12(b) we show the average spatial density in the box B computed in the NESS, \bar{n}_B , for different values of the bath-couplings. As expected, the bigger the injection rates, the higher the average density. On the other hand, the larger the extraction rate the smaller the average density. In Fig. 2.14(a) we present in blue the average density in the box B computed along the dashed diagonal of Fig. 2.12(b). The corresponding average density in the narrow channel A is shown in red. In both cases, the maximum/minimum is reached at the same point in $\ln(1 + \Gamma_{A,B}/g)$, which coincides with the maximum of the total current (Fig. 2.14(b)).

We conclude the Section by noticing an interesting consequence of the non-monotonicity of the average densities in box A and B . In Fig. 2.14(c) we plot the behavior of the total current versus the difference in chemical potential between A and B , $\sim \bar{n}_A - \bar{n}_B$. The chemical potential is not monotonous with the strength of the driving because the densities in A and B are not. This results in the curious hysteresis-like curve of Fig. 2.14(c). This curve confirms that there is a optimal value of the bath rates above

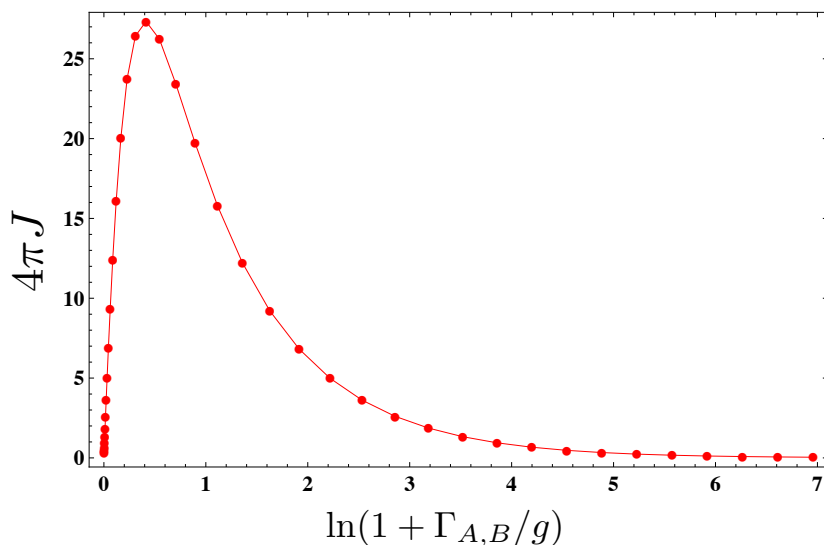


Figure 2.13: The total current along the red dashed line of Fig. 2.12(a). The maximum is for $\Gamma_{A,B} \sim g$. The tail decreases as $\frac{1}{\Gamma_{A,B}}$

which the difference between the chemical potential in regions A and B starts to decrease and the same does the total current¹⁸.

2.3.2 The two-site system and the large Γ -behavior.

In this Section, we interpret the $\frac{1}{\Gamma_{A,B}}$ behavior of the total current as a quantum Zeno effect [129, 130, 131]. The effect is at the basis of the intriguing property of a quantum system, subject to continuous measurements, to avoid the decay, even if prepared in a state which is not an eigenstate. This is a consequence of the wave function collapse. In our setup, the action of the external baths on the system can be interpreted as a set of measurements on the system, done with a rate $\Gamma_{A(B)}$, and followed by the injection (extraction) of a particle from the bath, if the site is found to be empty (full). However, as the rate of measurements becomes higher and higher the probability that the system leaves the state between two measurements decreases and eventually goes to zero at infinite $\Gamma_{A(B)}$.

To make this point more quantitative, as a case study, let us consider a one-dimensional two-site system ($i = A, B$) with a pure hopping Hamiltonian,

$$H = g \left[c_A^\dagger c_B + c_A c_B^\dagger \right], \quad (2.27)$$

¹⁸Again, the explanation of this is given with the quantum Zeno effect in the next Section.

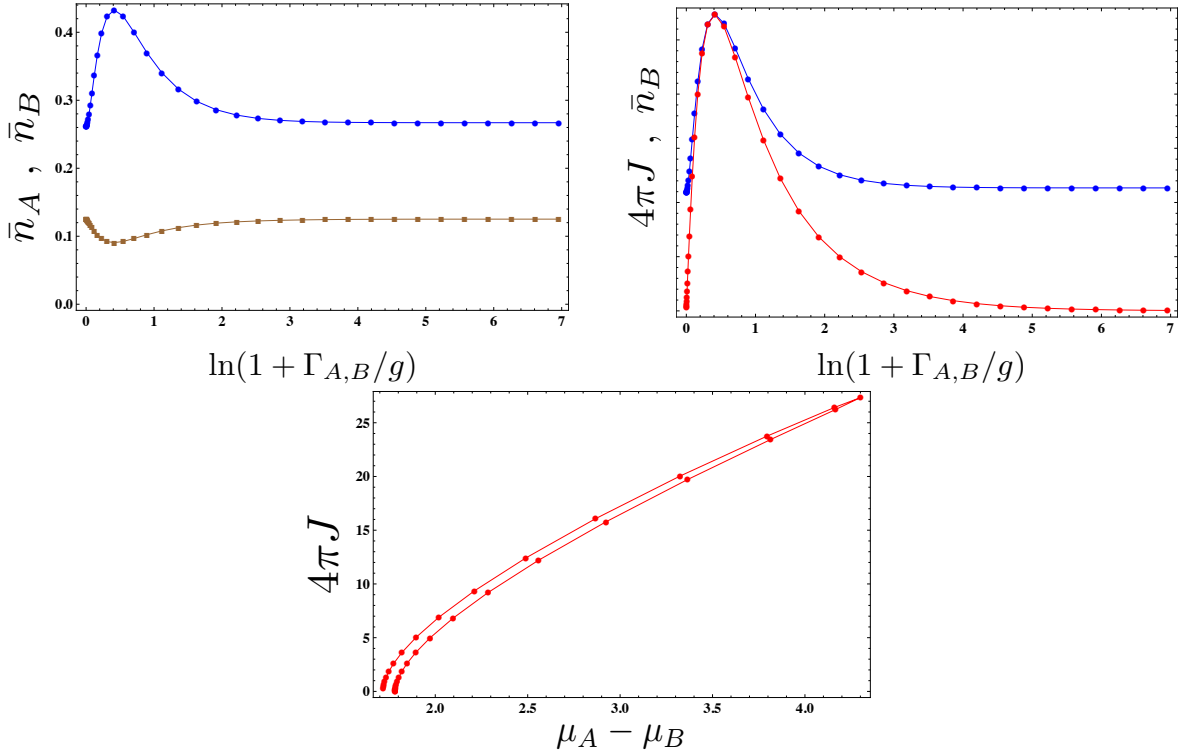


Figure 2.14: (a) We show in blue the average spatial density in the large box B , \bar{n}_B , and in brown the average spatial density in A , \bar{n}_A . In (b) we show the superposition of \bar{n}_B (blues) and the total current (red). The curves are rescaled to have the same maximum. Panel (c) shows the total current versus the difference between the chemical potential in A and B , $\mu_A - \mu_B = 4\pi \frac{\hbar^2}{2m} (\bar{n}_A - \bar{n}_B)$. Observe that the total current can be zero also if there is positive difference $|\bar{n}_A - \bar{n}_B|$. We think that this is just due the poor estimation of the chemical potentials.

with g being the hopping amplitude, and $\{c_i, c_j^\dagger\} = \delta_{ij}$. We call $|+\rangle = \frac{1}{\sqrt{2}}(c_A^\dagger + c_B^\dagger)|0\rangle$ and $|-\rangle = \frac{1}{\sqrt{2}}(c_A^\dagger - c_B^\dagger)|0\rangle$, the eigenvectors of the eigenvalues $+g$ and $-g$, respectively.

The site A can receive particles from an external bath at rate Γ , while from the site B the particles are extracted at the same rate. The \mathbf{Z} (*covariance*)-matrix for this system can be computed exactly,

$$\mathbf{Z} = \begin{pmatrix} 0 & -\frac{\Gamma^2}{g^2+4\Gamma^2} & -\frac{g\Gamma}{2(g^2+4\Gamma^2)} & 0 \\ \frac{\Gamma^2}{g^2+4\Gamma^2} & 0 & 0 & -\frac{g\Gamma}{2(g^2+4\Gamma^2)} \\ \frac{g\Gamma}{2(g^2+4\Gamma^2)} & 0 & 0 & \frac{\Gamma^2}{g^2+4\Gamma^2} \\ 0 & \frac{g\Gamma}{2(g^2+4\Gamma^2)} & -\frac{\Gamma^2}{g^2+4\Gamma^2} & 0 \end{pmatrix}.$$

The spatial density, and the current density can be computed analytically, the form for which is,

$$\begin{aligned} \langle \hat{n}(i) \rangle &= \frac{1}{2} + (1 - 2\delta_{i,B}) \frac{\Gamma^2}{g^2 + 4\Gamma^2} \xrightarrow{\Gamma \gg 1} \delta_{i,A} \\ \langle \hat{J}(A \rightarrow B) \rangle &= 4 \frac{g^2 \Gamma}{g^2 + 4\Gamma^2} \xrightarrow{\Gamma \gg 1} \frac{g^2}{\Gamma}. \end{aligned} \quad (2.28)$$

The form of the density in the $\Gamma \gg 1$ regime shows that the site A is always populated while the site B is always empty. The same behavior is predicted by implementing a perturbative expansion of the density matrix in $\frac{1}{\Gamma}$, Appendix I.

Let us recover the same $\frac{1}{\Gamma}$ behavior of the current for large Γ as a Zeno effect.

We consider an initial state $|\psi\rangle = \frac{1}{\sqrt{2}}(|+\rangle + |-\rangle) = c_A^\dagger|0\rangle$ which corresponds to one where the site- A is occupied while the site- B is empty. The probability that the state $|\psi\rangle$ has not yet decayed after M measurements by the baths at rate Γ , at time $t = \frac{M}{\Gamma}$, is given by,

$$P_M(t) \equiv P_1^M, \quad (2.29)$$

where the measurements are considered to be independent. P_1 is the probability of finding the system in the state $|\psi\rangle$ after the first measurement at time $1/\Gamma$, and it is computed to be

$$P_1 \equiv |\langle \psi | e^{-iH/\Gamma} | \psi \rangle|^2 = \cos^2(g/\Gamma).$$

Hence, the probability after M measurements in the large Γ limit is the exponential

$$P_{M=\Gamma t}(t) \approx e^{-\frac{g^2}{\Gamma} t}.$$

The bath can inject a new particle in the site A only if it is unoccupied and this occurs after a typical time $\tau = \frac{\Gamma}{g^2}$. The corresponding current thus behaves as $\langle \hat{J} \rangle \sim \frac{1}{\tau} = \frac{g^2}{\Gamma}$, for large Γ , and goes to zero asymptotically, which is consistent with Eq. (2.28).

2.3.3 Flow patterns in the open system.

We are now ready to compare the resulting flow patterns in the NESS of the open system with those shown in Section 2.2, in the context of the micro-canonical formalism, by matching the resulting average density and total current in the box B .

In analogy with the results obtained within the micro-canonical formalism, also within the Lindblad description, we can distinguish two regimes in the parameter $\bar{n}\epsilon^2$. For $\bar{n}\epsilon^2 \gg 1$, i.e. the **high density** regime, the flow corresponds to that obtained within the micro-canonical formalism and semi-classical diffraction theory rationalizes all observed features.

Within the **low density** regime, interesting patterns in the vorticity appear when the Fermi wavelength becomes of the order of the orifice – albeit less marked than the ones observed within the micro-canonical formalism.

At **high densities**, $\bar{n}\epsilon^2 \gg 1$, the Fermi wavelength is much smaller than the width of the orifice. Hence a semi-classical diffraction picture is expected to hold, marked by a relatively simple steady state pattern. For a representative set of parameters $\Gamma_A/g = \Gamma_B/g = 0.256$, the current density pattern and the absolute value of its vorticity ($|\nabla \times \mathbf{J}|$) are shown in Fig. 2.15(a), as well as the spatial density pattern in Fig. 2.15(b). The current pattern in Fig. 2.15(a), is characterized by a diffraction beam exiting from the orifice. The angle is determined by the transverse momentum of the highest propagating band in channel A (the second band). Those beams are reflected at $y = \pm W/2$ and interfere to form two islands of intense vorticity around $(4\epsilon, \pm\epsilon/2)$, which are thus just due elastic reflection from the boundaries. The beams are also visible in the density pattern in Fig. 2.15(b), and the most characteristic feature of this regime is again the rhomboidal region of very small and uniform vorticity centered at $(2\epsilon, 0)$. All this feature are present in the high density regime of the micro-canonical formalism (compare with Fig. 2.3). This strongly suggests that the quasi-steady flow captures, at late time, the steady state properties of a long system. Moreover, this correspondence opens questions about the equivalence of open and closed systems (far from the boundaries) in non-interacting theories, where equivalence is not expected a priori. Indeed, while in interacting system, randomization and thermalization in the thermodynamic limit can occur, in non interacting system there is no evident mechanism to damp time-oscillations and make the dynamics approaches a steady state.

The **low-density regime**, where the Fermi wavelength is of the order of the orifice width, is obtained, e.g., by tuning the injection rate, $\Gamma_{A,B}$, such that $\Gamma_A \ll \Gamma_B$, and $\frac{\Gamma_{A,B}}{g} \ll 1$.

For this regime, the current and vorticity patterns of the steady state are shown in

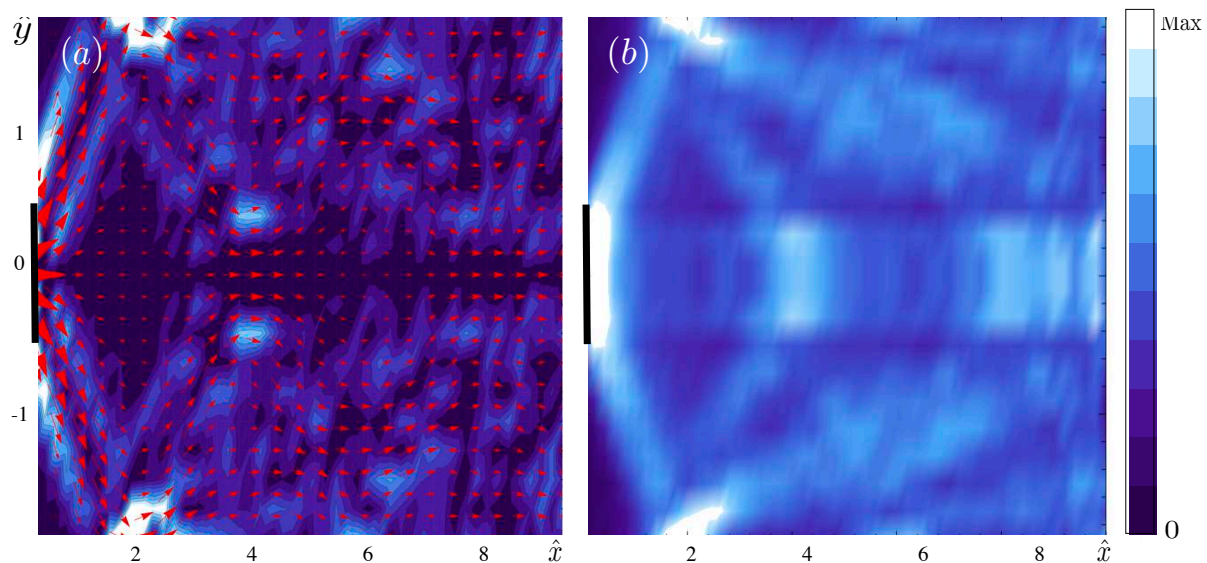


Figure 2.15: Steady state from the Lindblad equation at high average density, $\bar{n}\epsilon^2 \approx 2.5$. (a) Current density field $\mathbf{J}(x, y)$ (red arrows) superimposed on a contour plot of $|\nabla \times \mathbf{J}|$, for $\Gamma_{A,B} = 0.256g$. The orifice is marked by a solid bold line. (b) Corresponding density pattern. Distances are measured in units of the orifice width ϵ (note that the aspect ratio 2:5). In all plots lighter colors correspond to larger values (linear scale).

Fig. 2.16. The rhomboidal region of size $\sim W^2$ close to the orifice contains several intense local maxima of the vorticity, in qualitative agreement with what is found using the micro-canonical approach to closed systems. However, along with this feature a much more complicated structure of vorticity develops throughout the wide region B . We rationalize this richer vorticity structure as it follows. The coupling to the absorbing bath at $x = L = 10\epsilon$ acts only as a semi-transparent wall (it becomes fully transparent only in the limit of infinite absorption $\Gamma_B \rightarrow \infty$). Thus, there is partial reflection of the particle flux at the far ends, and reflected and incoming waves superpose to form a complicated structure of currents and vorticity due to interference. These effects, due to reflected waves, survive even close to the junction, because of the lack of dephasing and randomization in this non-interacting system. While some reflection is certainly also present in the higher density regime, its relative effect is apparently much smaller, so that the driven open system and the quasi-steady state of the closed system are very similar close to the orifice.

The correspondence between the Lindblad and the micro-canonical description of the system may be extended to the low density regime. A chance is to introduce some disorder in the box B close to the boundary in order to destroy regular patterns in the reflected waves.

In contrast to the involved structure of the steady-state of the open system, the

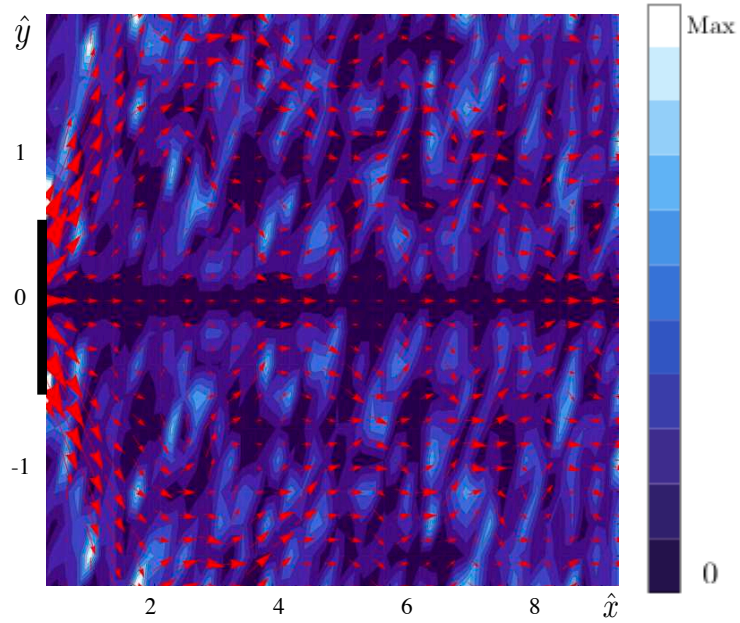


Figure 2.16: The current density superimposed on the absolute value of the vorticity, as obtained with a low average density, $\bar{n}\epsilon^2 \sim 1.1$. In this regime quantum interference effects are strong, as in closed systems, but they differ quantitatively, because of important reflections at the leads $x = \pm L$, which are absent in the quasi-steady state analyzed in closed systems. x and y coordinates are measured in units of the orifice width ϵ . Note the aspect ratio 2:5 of the axis scales.

micro-canonical approach can access the quasi-steady current pattern *before* reflections from the boundary at $\pm L$ occur (compare with Fig 2.4). It is thus more suitable to reveal the effects induced on the current pattern by quantum statistics. The most interesting effects due to Pauli exclusion are found at low densities $\bar{n}_A \epsilon^2 \approx 1$, in the rhomboidal region close to the orifice where the reflection of diffracted beams from boundaries do not play much of a role.

However, the qualitative (and quantitative in the high density regime) agreement between the micro-canonical and the Lindblad descriptions at high density strongly suggests that the quasi-steady state observed within the micro-canonical formalism captures the essence of the physics of the steady state.

2.4 Conclusion and Discussion.

Using two complementary approaches, we have analyzed both the steady-state properties and the transient dynamics of an ideal Fermi gas pushed out of an orifice into a wider region. Within both methods, the system has been studied numerically and the number of states, infinite in principle, is kept finite by the introduction of a finite lattice.

The main result is that Pauli exclusion strongly influences the current flow of fermions at finite density: it induces current patterns with staggered local moments of appreciable size, formed by itinerant fermions in an out-of-equilibrium steady state. These features can be found if the flow occurs in a non-uniform fermionic density, as if local maxima deviates incoming particles with a “statistical pressure” due to exchange interaction. In experiments where Friedel oscillations are present, for instance because of the confinement in optical traps, similar patterns in the vorticity may be expected. Combining the results obtained within the micro-canonical formalism with those within the Lindblad description, we suggest that the observed patterns in the low density regime of the micro-canonical description are steady and hence simpler to detect experimentally. Moreover, the resulting magnetic field may be used to experimentally probe the predicted patterns.

Since these effects are (after all) interference phenomena, we expect them to be robust towards weak interactions. It would be interesting to extend the present study to disordered systems and compare with the predictions of very heterogeneous current flow with substantial steady vorticity therein [137]. We expect that density inhomogeneities due to Friedel oscillations from strong impurities (taking the role of the boundaries) will lead to similar interesting vorticity patterns under a non-equilibrium steady state.

Already at equilibrium, Pauli exclusion leads to interesting interference phenomena in free fermions. We presented here one even more complex example out-of-equilibrium. Understanding deeply the role of Friedel oscillations out of equilibrium, is an attractive perspective.

Our study was originally motivated by non-trivial dynamics observed in non-interacting 1d fermionic systems [118, 119, 120, 121] and by the possibility that exchange interaction alone may induce non-trivial flows, such as turbulence, in ideal driven Fermi gases. Although our investigations reveal intriguing non-trivial patterns in the vorticity, the flow does not develop any chaotic/turbulent behavior, even at strong driving¹⁹.

We conclude the Chapter with a comment about the possibility of developing analytic effective descriptions of this system. The first point to observe is that, even though the density and current density can be obtained as summation over single particle solutions, this is not a simple task to accomplish in a non-integrable geometry as that of Fig. 2.1. On the other hand, one could think about deriving an effective description in terms of hydrodynamics, as it is possible for interacting quantum gases. Although this seems an attractive possibility, there are fundamental principles that seem to prevent this approach. Indeed, any hydrodynamical description relies on the fundamental assumption that the typical scale at which the system is observed is such that local equilibration washes any feature of particle distribution²⁰. In our system, the inter-particle distance is set by the Fermi wavelength which is the typical scale of non-trivial patterns, and thus the typical scale that we would describe. This consideration makes us rather skeptical about the possibility of formulating a predictive hydrodynamics which captures these features²¹.

¹⁹We called strong driving the regime where the driving is of the order of the chemical potential. Higher drivings could in principle reveal unexpected instabilities.

²⁰The scale of the observation should be much larger than the mean free path. In a non interacting system this quantity is strictly speaking infinite. However, if the exclusion principle is interpreted as an analogue of an interaction, the proper scale to consider for this kind of reasoning is the Fermi wavelength.

²¹An attempt in this direction was done in [121] for one-dimensional free fermions, which, however resulted in considerable overestimation of the amplitudes of the interesting features.

Chapter 3

Conclusive Remarks

In this thesis we analyzed two examples of numerical methods to tackle quantum many-body systems which are characterized by an infinite dimensional space of states. In both cases numerical methods have been useful to extract new physical informations about the studied systems.

The first method is the Truncated Conformal Spectrum Approach (TCSA) that we applied to perturbed Wess-Zumino-Witten (WZW) models as continuum limit of Heisenberg spin-chains and to Landau-Ginzburg theories. We proved that the method works in both cases and reproduces well known analytic predictions. This was not guaranteed for perturbed WZW models, since their space of states grows fast with the truncation level, nor in the case of Landau-Ginzburg theories, which are characterized by an uncountable space of states.

Within WZW models, we evidence that the TCSA can be used even in the presence of marginal perturbation, provided that UV divergences are properly treated. In the context of Landau Ginzburg theories, we instead tested a conjecture on the number of stable bound states in the spectrum.

The second approach has been used to study ideal fermionic systems, which, in our specific case, are forced to flow in a non-integrable, two dimensional geometry: a narrow channel joined to a wider volume. The infinite space of states is reduced to a finite subset by the introduction of a finite lattice with density of sites in principle much higher than the density of fermions. Two different approaches, based on the micro-canonical formalism and the Lindblad equation, have been used to study the non-equilibrium-steady-flow patterns generated when fermions are driven from the narrow channel to the larger volume.

Within both methods, we confirmed that quantum statistics affects the flow by generating non trivial patterns in the vorticity, at the scale of the Fermi wavelength. These patterns result in local magnetic moments of the order of measurable fractions of the magneton.

The resulting measurable, non-trivial features are predicted to form in every experiment where strong potential, disorder or confinement are present.

The formation of non-trivial flows is interpreted as a direct effect of Fermi statistics detectable if the flow occurs in a non-uniform (fermionic) density. Albeit particles are non-interacting, we conjecture that Pauli exclusion results in a statistical pressure on incoming fermions such that they sense the non-uniformity of "density-landscape" and avoid its maxima, generating the observed non-trivial patterns.

Acknowledgments. *I acknowledge my supervisors Giuseppe, Markus and Robert, and my friends and collaborators Pino, Luca, Andrea and Yasir, for advice and fundamental discussions on the works discussed in this thesis. I would also like to thank my companions in this adventure: Matteo, Jamir, Giancarlo, and Luca.*

Finally, a special thank is due to my family and to my girlfriend Ina for the support given during all the PhD.

Appendices

Appendix A

Basics of TBA.

In this Appendix we summarize principal concepts of Bethe-Ansatz and its thermodynamic formulation that are used in this thesis. As starting point, consider a (1+1)-dimensional integrable field theory on a circumference of length L , leading to a set of particles with mass $\{m_a\}$ which scatter with a scattering matrix $S_{ab}(\theta_{ab})$, $\theta_{ab} = \theta_a - \theta_b$ being the rapidity difference, each of these being defined to have: $E_a = m_a \cosh(\theta_a)$ and $p_a = m_a \sinh(\theta_a)$. For this simple theory we can write the wavefunction for a given state of N particle as

$$\psi(\{x_a\}) = \prod_{k=1}^N e^{ip_k x_k} \quad (\text{A.1})$$

Every time that two particles are exchanged (scatter) an S -matrix factors appear. Therefore assuming to pick a particle and bring it around the circle to put it back to the original position we have the identity (depending if we choose periodic or anti-periodic boundary conditions)

$$e^{ip_a L} \prod_{a \neq b} S(\theta_{ab}) = \pm 1 \quad (\text{A.2})$$

which is equivalent to to

$$m_a L \sinh(\theta_a) - i \sum_{b \neq a} \ln S(\theta_{ab}) = 2\pi n_a . \quad (\text{A.3})$$

These are the so called Bethe equations which put in relation the Bethe-numbers $\{n_a\}$ to the rapidities of the theory θ_a , called roots of the Bethe-equations. The energy and momentum of the multi-particle state are

$$E = \sum_a m_a \cosh(\theta_a) \quad , \text{ and } \quad p = \sum_a m_a \sinh(\theta_a). \quad (\text{A.4})$$

We can now take the thermodynamic limit (TDL) $L \rightarrow \infty$ and $N \rightarrow \infty$ keeping fixed the ratio N/L . In this limit the energy of the system can be written as

$$E[\rho^{(p)}] = \sum_a \int d\theta \rho^{(p)}(\theta) m_a \cosh(\theta), \quad (\text{A.5})$$

being $\rho^{(p)}(\theta)$ the probability density of the rapidities of the particles of species a . The Bethe equations in the TDL become

$$m_a L \sinh(\theta_a) - i \sum_b \int d\theta_b \ln S(\theta_a - \theta_b) \rho_b^{(p)}(\theta_b) = 2\pi n_a. \quad (\text{A.6})$$

The roots for the Eq. (A.6) are solution for another set of non-admissible quantum numbers, corresponding to another set of excitation called *holes*, which density is called $\rho_a^{(h)}$. The total density can be defined to be

$$\rho_a = \rho_a^{(p)} + \rho_a^{(h)}. \quad (\text{A.7})$$

At this stage, the thermodynamics of the system can be worked out by estimating the phase space within the shell $\Delta\theta$ in the rapidities,

$$\begin{aligned} \Omega_a^{\text{bosons}} &= \frac{[L\rho_a(\theta)\Delta\theta]!}{[L\rho_a^{(p)}(\theta)\Delta\theta]![L\rho_a^{(h)}(\theta)\Delta\theta]!} \\ \Omega_a^{\text{fermions}} &= \frac{[L(\rho_a(\theta) + \rho^{(p)}(\theta) - 1)\Delta\theta]!}{[L\rho_a^{(p)}(\theta)\Delta\theta]![L(\rho_a(\theta) - 1)\Delta\theta]!}, \end{aligned} \quad (\text{A.8})$$

to access the entropy ($S = \ln \prod_a \Omega_a$) and the free energy $f = E - TS$. The temperature is defined to be $T = \frac{1}{R}$. All the thermodynamic functions are usually expressed in terms of *pseudo-energies* $\epsilon_a(\theta)$ which are defined by

$$e^{-\epsilon_a(\theta)} = \frac{\rho_a^{(p)}(\theta)}{\rho_a(\theta) \pm \rho_a^{(p)}(\theta)} \quad (\text{A.9})$$

where the $+$ -sign is for boson and the minus sign for fermions. The free energy, expressed in terms of pseudo energies, looks that of a free system with “effective” spectrum $\epsilon_a(\theta)$:

$$f(R) = \mp \frac{1}{R} \sum_a \int \frac{d\theta}{2\pi} m_a \cosh(\theta) \ln(1 \pm e^{-\epsilon_a(\theta)}) \quad (\text{A.10})$$

and the ground state energy is

$$E_{gs}(R) = \mp \sum_a \int \frac{d\theta}{2\pi} m_a \cosh(\theta) \ln(1 \pm e^{-\epsilon_a(\theta)}) \quad (\text{A.11})$$

In a massive theory however there must be a part of the energy which scales linearly with R for large R , the bulk energy: $E_{gs} \sim \epsilon_{\text{bulk}} R$.

Let us now outline how the mass-coupling formula can be derived. Let us consider for simplicity a Z_2 -invariant theory where the conformal action is perturbed with an operator with dimension 2Δ (we assume $\Delta = \bar{\Delta}$):

$$\mathcal{S} = \mathcal{S}_{\text{CFT}} + \lambda \int d^2x \Psi_{\Delta}(x)$$

From dimensional arguments we have that $\lambda = \mathcal{D}m^{2-2\Delta}$. To determine \mathcal{D} we apply the conformal perturbation theory and arrive to

$$f(R) = -\frac{c_0}{12} - \frac{\epsilon_{\text{bulk}}}{2\pi} R^2 + \mathcal{F}_{2n} R^{2(2-2\Delta)} \lambda^2 + \dots \quad (\text{A.12})$$

On the other hand, the TBA leads to expansion for the the free energy:

$$f(R) = -\frac{c_0}{12} - \frac{\epsilon_{\text{bulk}}}{2\pi} R^2 + f_{2n}(mR)^{2(2-2\Delta)} + \dots \quad (\text{A.13})$$

Thus by comparing the terms proportional to $R^{2-2\Delta}$, and using $\lambda = \mathcal{D}m^{2-2\Delta}$ we get

$$\mathcal{D}^2 = \frac{f_2}{\mathcal{F}_2} \quad (\text{A.14})$$

which gives the mass-coupling formula.

Appendix B

Compactified boson and sine-Gordon model.

To test the code we first reproduced the well known spectrum of the sine-Gordon model

$$\mathcal{S} = \int d^2x \left(\frac{1}{2} \partial_\mu \phi \partial^\mu \phi + 2\lambda \cos(\beta\phi) \right) \quad (\text{B.1})$$

The perturbation is just the sum of the two primaries with $n = \pm 1$. For a specific value of the frequency $\beta = \sqrt{2\pi}$ the model has an underlying $SU(2)$ symmetry and therefore it presents some peculiar features. We correctly reproduced the spectrum and the degeneracies just fixing the parameter β of the compactified boson to $\sqrt{2\pi}$ and working in the winding sectors $w = 0, 1, -1$ to account for the topological charges of the solitons next to the neutral breathers. We also verified the mass-coupling relation

$$\lambda = \frac{\Gamma\left(\frac{\beta^2}{8\pi}\right)}{\pi\Gamma\left(1 - \frac{\beta^2}{8\pi}\right)} \left[M\sqrt{\pi} \frac{\Gamma\left(\frac{1}{2} + \frac{\xi}{2\pi}\right)}{2\Gamma\left(\frac{\xi}{2\pi}\right)} \right]^{2 - \frac{\beta^2}{4\pi}}, \quad \xi = \frac{\beta^2}{8} \frac{1}{1 - \frac{\beta^2}{8\pi}} \quad (\text{B.2})$$

computed in Ref. [?], and we finally checked the numerical data with the thermodynamic Bethe-ansatz (TBA) computation of the ground state energy.

The results (for the winding sector $w = 0$) can be found in Fig. (B.1). Here we have also set the parameter λ in order to have $M = 1$ according to (B.2). The green line is the ground state of the theory and is in quite good agreement with the TBA prediction (black, dashed line). Above that, we find the first excited level (red) to be a bound state with mass $m_1 = M = 1$ as expected, while the mass ratio between the second (blue) and the first bound state is $m_2/m_1 = \sqrt{3}$.

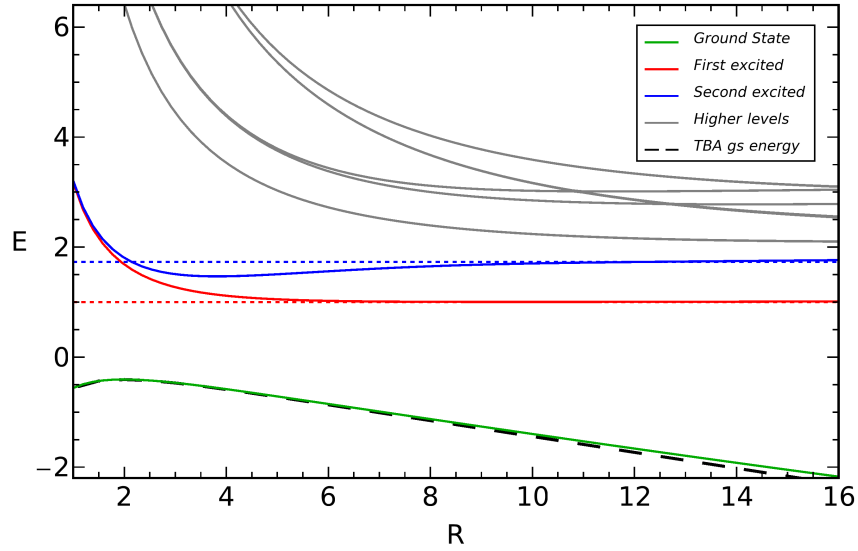


Figure B.1: In the picture it is shown the spectrum of the Sine-Gordon model with frequency $\beta = \sqrt{2\pi}$ in the $w = 0$ sector. The thermodynamic Bethe-ansatz prediction for the ground state (dashed black line) is well reproduced as well as that for the mass ratio between the first and second mass ($m_2/m_1 = \sqrt{3}$, dashed blue line). The first mass is set to one (dashed red line) by using the mass-coupling formula (B.2).

Appendix C

The Derivative-method.

In this appendix we compute the generic matrix elements of the form

$$M_{ab}^{(m)} = \langle a | \phi^m(0) | b \rangle \quad (\text{C.1})$$

within the derivative method. Here $|a\rangle = |n, a_L, a_R\rangle$ and $|b\rangle = |n', b_L, b_R\rangle$, and the matrix elements are formally written as

$$M_{ab}^{(m)} = (-i)^m \partial_\gamma^{(m)} \langle n, a_L, a_R | e^{i\gamma\phi(0)} | n', b_L, b_R \rangle |_{\gamma=0}.$$

To compute such matrix elements we can separate the left and right parts of the vertex operator

$$\langle n, a_L, a_R | e^{i\gamma\phi} | n', b_L, b_R \rangle = \langle n, a_L | e^{i\gamma\phi_L} | n', b_L \rangle \langle n, a_R | e^{i\gamma\phi_R} | n', b_R \rangle, \quad (\text{C.2})$$

and the two terms with definite chirality may be computed exploiting the commutation relations (1.163), so that the two chiral matrix elements can be rewritten as two polynomials in γ , $P_L(\gamma)$ and $P_R(\gamma)$:

$$\langle n, a_L, a_R | e^{i\gamma\phi} | n', b_L, b_R \rangle = \langle n | e^{i\gamma\phi} | n' \rangle P_L(\gamma) P_R(\gamma), \quad (\text{C.3})$$

where $P_{L(R)}(\gamma) = \alpha_{0L(R)} + \alpha_{1L(R)}\gamma + \alpha_{2L(R)}\gamma^2 + \dots$. The final prescription to compute the matrix element is

$$M_{ab}^{(m)} = (-i)^m \partial_\gamma^{(m)} \left\{ \frac{\beta}{2\pi} \int_{-\frac{\beta}{\pi}}^{\frac{\beta}{\pi}} d\phi e^{i[\beta(n-n')+\gamma]\phi} P_L(\gamma) P_R(\gamma) \right\}_{\gamma=0} \quad (\text{C.4})$$

leading to the following formula

$$M_{ab}^{(m)} = (-i)^m \frac{\beta}{2\pi} \int_{-\frac{\beta}{\pi}}^{\frac{\beta}{\pi}} d\phi e^{i\beta(n-n')\phi} \sum_{p=0}^m \binom{m}{p} (i\phi)^p \partial_\gamma^{m-p} [P_L(\gamma) P_R(\gamma)]_{\gamma=0}. \quad (\text{C.5})$$

Performing the integrals in (C.5) we obtain

$$\begin{aligned}
 M_{ab}^{(m)} = & (-1)^{\frac{m}{2}} m! \sum_{\substack{p=0 \\ p \text{ even}}}^m \left\{ \delta_{n,n'} \frac{(-1)^{\frac{p}{2}}}{(p+1)!} \left(\frac{\pi}{\beta} \right)^p + \right. \\
 & \left. (1 - \delta_{n,n'})(1 - \delta_{p,0})(-1)^{n-n'-1} \sum_{\substack{q=0 \\ p-q \text{ odd}}}^{p-1} \frac{(-1)^{\frac{p+q+1}{2}}}{(p-q)! [\pi(n-n')]^{q+1}} \right\} \sum_{k,j=0}^m \alpha_{kL} \alpha_{jR} \delta_{k+j,m-p}.
 \end{aligned} \tag{C.6}$$

This last formula expresses all matrix elements of the operator $\phi(0)^m$ in terms of the coefficients $\{\alpha_{sL(R)}\}$ that are computed numerically just exploiting the $U(1)_1$ algebra. It holds just for even m , however the extension to odd powers is straightforward.

Appendix D

The commutator $[a_p, e^{i\gamma\phi}]$.

The commutator between $U(1)_1$ modes and the operator $e^{i\gamma\phi}$ is well defined if γ is a multiple of the inverse compactification radius, $\gamma = \beta n$, and the operator is then a primary field of the theory. In this case, the commutator acts as a derivative with respect to ϕ , that is

$$[a_p, e^{i\beta n\phi}] = i\partial_\phi e^{i\beta n\phi} = (-\beta n) e^{i\beta n\phi}. \quad (\text{D.1})$$

The Fourier expansion in the compactification region of the operator $e^{i\gamma\phi}$ for generic real γ , reads

$$e^{i\gamma\phi} = \sum_n c_n^{(\gamma)} e^{i\beta n\phi}. \quad (\text{D.2})$$

Then, the natural definition of the commutator for generic γ would be

$$[a_p, e^{i\gamma\phi}] = \sum_n c_n^{(\gamma)} [a_p, e^{i\beta n\phi}] = \sum_n (-\beta n) c_n^{(\gamma)} e^{i\beta n\phi}. \quad (\text{D.3})$$

This expression, however, must be taken with care, since the series on the r.h.s. does not converge to $-\gamma e^{i\gamma\phi}$, as one could expect. This can be seen in Fig. D.1. Nonetheless, the r.h.s. of eq. (D.3) can still be made sensible in the distributional sense. Indeed, since $e^{i\gamma\phi}$ is not continuous on the circle if γ is not a multiple of the radius β , then we have to take derivatives in the distributional sense. It is now easy to see that the coefficients $(-n\beta)c_n^{(\gamma)}$ in the r.h.s. of eq. (D.3) are indeed the Fourier coefficients of the distribution $i\partial_\phi e^{i\gamma\phi}$. With these considerations in mind, we can safely write

$$[a_p, e^{i\gamma\phi}] = i\partial_\phi e^{i\gamma\phi}, \quad (\text{D.4})$$

but now the derivative must be considered in the distributional sense. If we apply such a distribution to a test function $\psi(\phi)$, we see that some boundary contributions are present if the function is not periodic in $[-\pi/\beta, \pi/\beta]$. A short computation indeed shows that

$$[a_p, e^{i\gamma\phi}] = -\gamma e^{i\gamma\phi} + 2 \sin\left(\frac{\pi}{\beta}\gamma\right) \delta(\phi - \pi/\beta). \quad (\text{D.5})$$

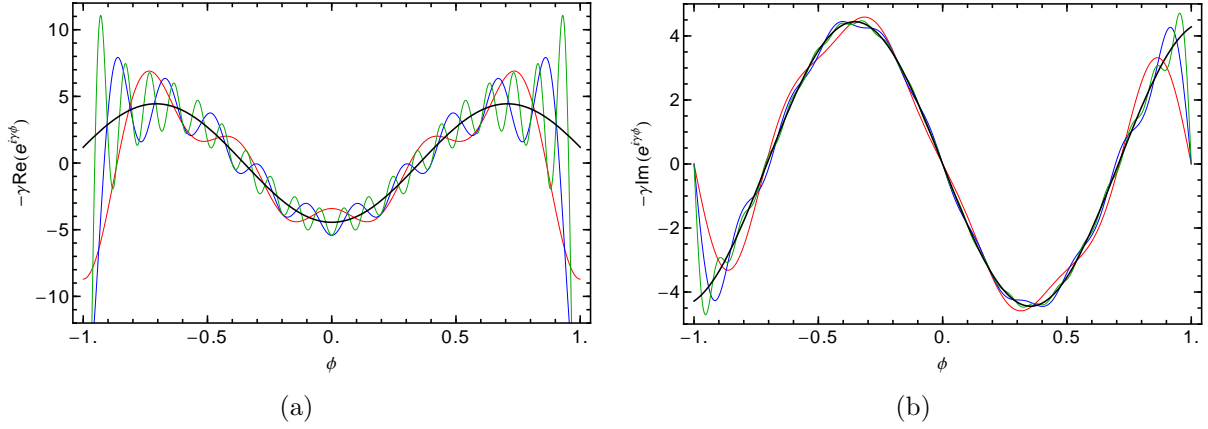


Figure D.1: (a) The black thick line is the real part of $-\gamma e^{i\gamma\phi}$ on the circle for γ not a multiple of β (here $\gamma = \sqrt{2}\beta$ and $\beta = \pi$). We also show the series of the r.h.s. of eq. (D.3), truncated keeping only N terms ($N = 5, 10, 50$ in red, blue, green respectively). It is clear that, even if the average value of the truncated series approximates the real part of the function, the series does not converge to it. The width of the oscillations is indeed constant. (b) The imaginary part of $-\gamma e^{i\gamma\phi}$ on the circle for $\gamma = \sqrt{2}\beta$. Increasing N , the truncated Fourier series ($N = 5, 10, 50$ in red, blue, green respectively) clearly converges to the function..

As it should, the boundary term vanishes if $\gamma = n\beta$ for some integer n . This we claim to be the natural definition of the commutator between $U(1)_1$ -modes and the operator $e^{i\gamma\phi}$ for generic γ . Nonetheless our target theory will be recovered just in the $\beta \rightarrow 0$ limit where the additional boundary term does not contribute. With this in mind, the derivative method consists in discarding this term and forcing the commutator (1.163) also when γ is not a multiple of β .

Appendix E

Influence of boundary conditions.

Here, we analyze the influence of boundary conditions on the formation of non-trivial current patterns in closed systems, by considering different boundary conditions. We work within the micro-canonical formalism with $V_{\text{in}} = 0$, and $V_{\text{fin}} \approx \frac{1}{2}\mu$, in the low-density regime $\bar{n} \equiv \bar{n}_B \approx \bar{n}_A \approx 1.1/\epsilon^2$, where non-trivial patterns appear. In Fig. E.1(b) we show patterns obtained with periodic boundary conditions where $y = \pm W/2$ are identified. We observe that the main *qualitative* features of the patterns close to the orifice ($x \lesssim 4\epsilon \sim W$) are still present with periodic boundary conditions; in particular, the two islands of vorticity close to $(x, y) \approx (2\epsilon, \pm\epsilon/2)$ still form. However, one should not expect quantitative agreement near the orifice.

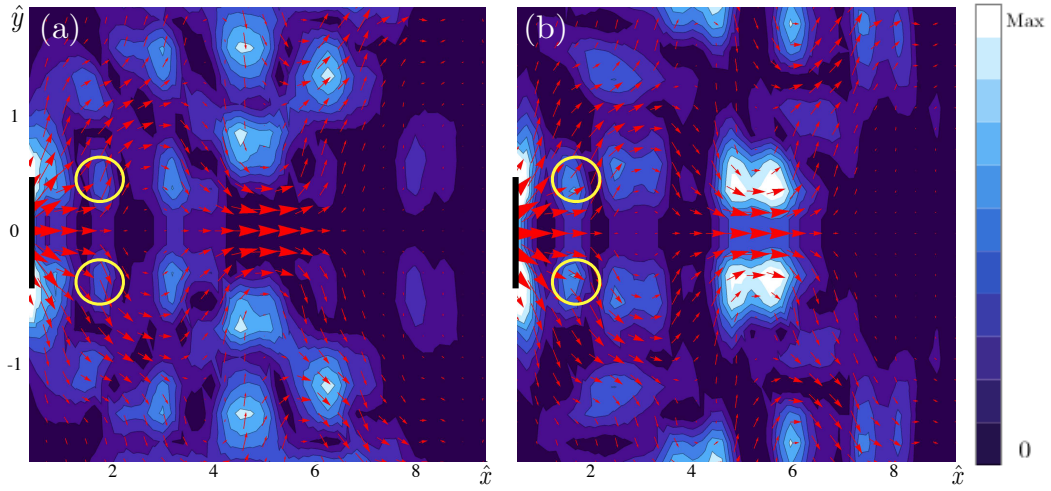


Figure E.1: Comparison between (a) closed and (b) periodic boundary conditions at $y = \pm W/2$ (here $W = 4\epsilon$) in the low-density regime ($\bar{n}\epsilon^2 \approx 1.1$). Shown is the current density, superimposed on the vorticity contour plot, as obtained within the micro-canonical approach, with $V_{\text{in}} = 0$, and $V_{\text{fin}} \approx \mu/2$. Two non-trivial patterns close to the orifice at $(x, y) \approx (2\epsilon, \pm\epsilon/2)$ are encircled in yellow. The x and y coordinates are measured in units of the orifice width ϵ . Note the aspect ratio 2:5 of the axis scales. The color code is the same for both figures.

Appendix F

Magnetic and electric fields generated by charged polarized particles.

Let \vec{j} be the $2d$ number current density of atoms in the $x - y$ plane ($z = 0$), and define

$$\vec{b}(\vec{r} = \{x, y, z\}) = \frac{\mu_0}{4\pi} \cdot \int dx' dy' \vec{j}(\vec{r}') \times \frac{\vec{r} - \vec{r}'}{|\vec{r} - \vec{r}'|^3}$$

where μ_0 is the permeability of vacuum. According to the Biot-Savart law, the magnetic field generated by moving particles of charge e , is then given by

$$\vec{B}(\vec{r}) = e\vec{b}(\vec{r}).$$

Similarly, polarized neutral particles with a static electric dipole \vec{d} produce a magnetic field

$$\vec{B}(\vec{r}) = (\vec{d} \cdot \vec{\nabla}) \vec{b}(\vec{r}).$$

Likewise, polarized particles with static magnetic moment \vec{m} generate an electric field

$$\vec{E}(\vec{r}) = -(\vec{m} \cdot \vec{\nabla}) \vec{b}(\vec{r}).$$

Appendix G

The Liouville-Fock Space.

In this Appendix we sketch the contraction of the Liouville-Fock space, \mathcal{K} , the operator space which contains the density matrix of the system and which is the starting point for the construction of the third-quantization formalism. More details can be found in Ref. [37, 38].

Let us define the states of \mathcal{K} as

$$P_{\underline{\alpha}} = 2^{-n/2} w_1^{\alpha_1} \dots w_{2n}^{\alpha_{2n}}, \quad (\text{G.1})$$

where $\{w\}$ are Majorana fermions satisfying $\{w_1, w_j\} = 2\delta_{i,j}$, and $\alpha_i \in \{0, 1\}$. A scalar product can be introduced in this space as

$$P_{\underline{\alpha}} \cdot P_{\underline{\alpha}'} = \text{Tr} P_{\underline{\alpha}}^\dagger P_{\underline{\alpha}'}.$$

The dimension of the Liouville-Fock space is $\dim \mathcal{K} = 2^{2n}$ and $\rho \in \mathcal{K}$. The idea is to introduce $2n$ creation and $2n$ annihilation operators on this space as follows:

$$\begin{aligned} c_j P_{\underline{\alpha}} &= \alpha_j w_j P_{\underline{\alpha}} \\ c_j^\dagger P_{\underline{\alpha}} &= (1 - \alpha_j) w_j P_{\underline{\alpha}}. \end{aligned} \quad (\text{G.2})$$

The crucial point is now to express the Liouvillean in terms of $\{c, c^\dagger\}$. This can be done by looking explicitly at the action of the Liouvillean expressed in Majorana fermions and reproducing the same result with the above new operators. We show, for instance how to do it for the unitary part of the Liouvillean. The first point is to consider that, having a Lie algebra structure on \mathcal{K} , the commutator $[H, \cdot]$ can be represented as

$$|[H, \cdot]\rangle = \text{ad} H |\cdot\rangle.$$

The Hamiltonian a quadratic form in the Majorana-fermions and hence the fundamental ingredient to map is

$$\text{ad}(w_i w_j) P_{\underline{\alpha}} = w_i w_j P_{\underline{\alpha}} - P_{\underline{\alpha}} w_i w_j = 2 \left(c_i^\dagger c_j - c_j^\dagger c_i \right) P_{\underline{\alpha}}.$$

With similar ideas one expresses the full Liouvillean in terms of the $4n$ adjoint fermions.

Appendix H

Normal Master Modes and Shape Matrix.

In this Appendix we sketch the procedure to diagonalize the Liouvillean in its final form in terms of Normal Master Modes (NMM). More details can be found in Ref. [37, 38]. The first point is to observe that the shape matrix \mathbf{A} can be casted in the following form

$$\mathbf{A} = \mathbf{V}^T \mathbf{\Lambda} \mathbf{V}, \text{ with } \mathbf{\Lambda} = \mathcal{D} \mathbf{J}, \mathbf{V}^T \mathbf{V} = \mathbf{J}$$

with \mathcal{D} diagonal and

$$\mathbf{J} = \begin{pmatrix} 0 & 1 \\ 1 & 0 \end{pmatrix} \otimes \mathbb{I}_{2n}. \quad (\text{H.1})$$

At this stage Eq. (2.22) is “similar”¹ to

$$\hat{\mathcal{L}} = \underline{a} \cdot \mathbf{V}^T \mathbf{\Lambda} \mathbf{V} \underline{a} = \underline{a} \cdot \mathbf{V}^T \mathcal{D} \mathbf{J} \mathbf{V} \underline{a}$$

which can be diagonalized as

$$\hat{\mathcal{L}} = \underline{b}' \cdot \mathcal{D} \underline{b} \quad (\text{H.2})$$

with

$$\underline{b} = \mathbf{J} \mathbf{V} \underline{a} \text{ and } \underline{b}' = \mathbf{V}^T \underline{a}.$$

Even if b and b' satisfy canonical anti-commutation relations they do not constitute a real fermionic base since they are not the adjoint of each other. However, these operators (the NMM) diagonalize the Liouvillean.

¹See [38] for more details.

Appendix I

The large- Γ expansion of the density matrix.

Here, we outline a recursive solution for the Lindblad equation for the two-site system case, in the large- Γ regime.

Our objective is to recover the constant large- Γ behavior of the average density and the $\frac{g^2}{\Gamma}$ trend of the total current. We assume that the density-matrix can be expanded as

$$\rho = \rho_0 + \frac{1}{\Gamma}\rho_1 + \frac{1}{\Gamma^2}\rho^2 + \dots \quad (\text{I.1})$$

and, once plugged into the Lindblad equation (2.18), we solve the resulting recursive linear system up to the required order:

$$\mathcal{L}[\rho_0] = 0, \quad (\text{I.2})$$

$$\mathcal{L}[\rho_1] = i[H, \rho_0], \quad (\text{I.3})$$

$$\mathcal{L}[\rho_2] = i[H, \rho_1],$$

$$\mathcal{L}[\rho_3] = \dots$$

The Eq. (I.2) for the two-site system with the constraint that the trace of the density-matrix is unity, gives the unique solution,

$$\rho_0 = |1, 0\rangle\langle 1, 0|, \text{ where } |1, 0\rangle \equiv c_A^\dagger |0\rangle. \quad (\text{I.4})$$

This is the state with site- A occupied and the site- B empty, so that none of the two external baths can modify it. The asymptotic average density $\delta_{i,A}$ is thus captured correctly by ρ_0 . At this point, ρ_1 can be determined using Eq. (I.3), thus obtaining,

$$\rho_1 = \frac{ig}{2} [|0, 1\rangle\langle 1, 0| - |1, 0\rangle\langle 0, 1|], \text{ where } |0, 1\rangle \equiv c_B^\dagger |0\rangle, \quad (\text{I.5})$$

from this it is simple to compute the average current density, which at large Γ , reads as $\langle \hat{J} \rangle \sim \frac{g^2}{\Gamma}$.

Bibliography

- [1] I. Affleck, J. Phys.: Condens. Matter **1** 3047, (1989)
- [2] G. Mussardo, *Statistical Field Theory, An Introduction to Exactly Solved Models in Statistical Physics*, Oxford University Press, (2010).
- [3] J. B. Kogut, Rev. Mod. Phys. **51**, 659 (1979).
- [4] W. Hamber, General Relativity and Gravitation, **41**, 817 (2009).
- [5] R. P. Feynman, Int. Journal of Theoretical Physics, **21** 467, (1982).
- [6] D. Aharonov, arXiv:quant-ph/9812037v1 (1998)
- [7] I. Bloch, J. Dalibard, and S. Nascimbène Nature Physics, **8** 267, (2012).
- [8] R. Blatt, and C. F. Roos, Nat. Phys. **8** 277, (2012)
- [9] *Extended Linear Chain Compounds*, Edited by J. S. Miller, Plenum Press, New York (1983).
- [10] H. Rothe, *Lattice Gauge Theories: An Introduction*, World Scientific (2012).
- [11] C. Gattringer and C. B. Lang, *Quantum Chromodynamics on the Lattice*, Springer (2010).
- [12] R. Bulla, T. Costi, T. Pruschke, Rev. Mod. Phys., **80** 395, (2008)
- [13] K. Wilson, Rev. Mod. Phys., **47** 773, (1975)
- [14] R. U. Schollwöck, Rev. Mod. Phys., **77**, 259 (2005)
- [15] S. R. White, Phys. Rev. Lett. **69** 2863 (1992); Phys. Rev. B **48**, 10345 (1993).
- [16] S. Östlund, and S. Rommer, Phys. Rev. Lett. **75**, 3537 (1995).
- [17] R. Orus, arXiv:1306.2164v2 (2013).

- [18] *Finite size scaling and numerical simulation of statistical systems*, Edited by V. Privman, World Scientific (1990).
- [19] G. Marchesini, Int. J. Mod. Phys. A, **22**, 5443 (2007).
P. de Forcrand, arXiv:1005.0539v2 (2010).
- [20] J. Kolorenč, and L. Mitás, Rep. Prog. Phys. **74**, 026502 (2011).
- [21] V. P. Yurov and A. B. Zamolodchikov, Int. J. Mod. Phys. A **5** 3221 (1990).
- [22] P. Di Francesco, P. Mathieu and D. Sénéchal, *Conformal field theory*, Springer (1997).
- [23] M. Di Ventra, *Electrical transport in nanoscale systems* (Cambridge University Press, Cambridge 2008).
- [24] L. D. Landau, E. M. Lifshitz, *Fluid Mechanics*, Vol. **6**, Pergamon Press (1987 2nd ed.).
- [25] F. Bloch, Zeitschrift für Physik **81**, 363 (1932).
- [26] P. C. Martin and J. Schwinger, Phys. Rev. **115**, 1342 (1959).
- [27] G. Vignale, C. A. Ullrich, and S. Conti, Phys. Rev. Lett. **79**, 4878 (1997).
- [28] I. V. Tokatly, Phys. Rev. B **71**, 165104 (2005).
- [29] R. D'Agosta and M. Di Ventra, J. Phys.: Condens. Matter **18**, 11059 (2006).
- [30] N. Bushong, J. Gamble, and M. Di Ventra, Nano Lett. **7**, 1789 (2007).
- [31] G. P. Berman and F. M. Izrailev Chaos **15**, 015104 (2005).
- [32] M. Beria, G. P. Brandino, L. Lepori, G. Sierra, R. Konik, arXiv:1301.0084, (2013)
- [33] J. Wess, B. Zumino, Phys. Lett. B, **37**, 95 (1971).
- [34] E. Witten, Nucl. Phys. B, **223** 422 (1983).
- [35] H. Kleinert, *Gauge Fields in Condensed Matter*, World Scientific (1989).
- [36] G. Lindblad, Commun. Math. Phys. **48**, 119 (1976).
- [37] T. Prosen, New J. Phys. **10**, 043026 (2008).
- [38] T. Prosen, J. Stat. Mech. (**2010**), P08016 (2010).

- [39] A. O. Gogolin, A. A. Nersesyan, and A. M. Tsvelik, *Bosonization and Strongly Correlated Systems*, Cambridge University Press, (1998); T. Giamarchi, *Quantum Physics in One Dimension*, Oxford University Press, (2004).
- [40] M. Takahashi, *Thermodynamics of One-Dimensional Solvable Models*, Cambridge University Press (1999);
B. S. Shastry, S. S. Jha, V. Singh, *Exactly Solvable Problems in Condensed Matter and Relativistic Field Theory*, Lecture Notes in Physics, Springer-Verlag (1985).
- [41] V. P. Yurov and Al. B. Zamolodchikov, Int. J. Mod. Phys. A **6** 4557 (1991).
- [42] G. Delfino, G. Mussardo and P. Simonetti, Nucl.Phys. B473 (1996) 469-508.
- [43] G. Delfino and G. Mussardo, Nucl.Phys. B516 (1998) 675-703.
- [44] R.F.Dashen, B.Hasslacher and A.Neveu, *Phys. Rev.* **D 10** (1974) 4130; R.F.Dashen, B.Hasslacher and A.Neveu, *Phys. Rev.* **D 11** (1975) 3424.
- [45] J. Goldstone and R. Jackiw, *Phys.Rev.* **D 11** (1975) 1486.
- [46] G. Mussardo, Nucl. Phys. B, **779**, 101 (2007).
- [47] M. Lässig, G. Mussardo, and J. L. Cardy, Nucl. Phys. B **348** 591 (1991).
- [48] L. Lepori, G. Mussardo, and G. Z. Toth, J. Stat. Mech. **0809** P09004 (2008).
- [49] L. Lepori, G. Z. Toth, and G. Delfino, J. Stat. Mech. **0911** P11007 (2009).
- [50] F.D.M. Haldane, Phys. Rev. Lett. **60** 635 (1988); B.S. Shastry, Phys. Rev. Lett. **60** 639 (1988).
- [51] G. Feverati, F. Ravanini and G. Takacs, Phys. Lett. B **430** 264 (1998).
- [52] G. Feverati, F. Ravanini and G. Takacs, Phys. Lett. B **444** 442 (1998).
- [53] Z. Bajnok, L. Palla, G. Takacs and F. Wagner, Nucl. Phys. B **601**, 503 (2001).
- [54] P. Dorey, I. Runkel, R. Tateo and G. M. T. Watts, Nucl. Phys. B **578** 85 (2000).
- [55] T. R. Klassen and E. Melzer, Nucl. Phys. B **370** 511 (1992).
- [56] P. Dorey and R. Tateo, Nucl. Phys. B **482** 639 (1996).
- [57] P. Dorey, A. J. Pocklington, R. Tateo and G. M. T. Watts, Nucl. Phys. B **525** 641 (1998).
- [58] T. R. Klassen and E. Melzer, Nucl. Phys. B **362**, 329 (1991).

- [59] G. Feverati, F. Ravanini and G. Takacs, Nucl. Phys. B **540** 543 (1999).
- [60] P. Fonseca and A. Zamolodchikov, J. Stat. Phys. **110** 527 (2003).
- [61] R. M. Konik and Y. Adamov, Phys. Rev. Lett. **98** 147205 (2007).
- [62] R. M. Konik and Y. Adamov, Phys. Rev. Lett. **102** 097203 (2009).
- [63] G. P. Brandino, R. M. Konik and G. Mussardo, J. Stat. Mech., P07013 (2010).
- [64] R. M. Konik, Phys. Rev. Lett. **106** 136805, (2011).
- [65] J.-S. Caux and R. M. Konik, Phys. Rev. Lett. **109** 175301 (2012).
- [66] I. Affleck and F. D. M. Haldane, Phys. Rev. B **36** 5291 (1987).
- [67] I. Affleck, D. Gepner, H. J. Schulz and T. Ziman, J. Phys. A **22** 511 (1989).
- [68] M. Kumar, S. Ramasesha, D. Sen and Z. G. Soos, Phys. Rev. B **75** 05204 (2007).
- [69] T. Barnes, J. Riera, and D. A. Tennant, Phys. Rev. B **59** 11384 (1999).
- [70] J. I. Cirac and G. Sierra, Phys. Rev. B **81** 104431 (2010).
- [71] A. E. B. Nielsen, J. I. Cirac and G. Sierra, J. Stat. Mech. P11014 (2011).
- [72] R. Thomale, S. Rachel, P. Schmitteckert, and M. Greiter, Phys. Rev. B. **85**, 195149 (2012).
- [73] M. Tinkham, *Introduction to Superconductivity*, McGrawHill (1996)
- [74] V.G. Knizhnik and A. B. Zamolodchikov, Nucl. Rev. B **247** 83 (1984).
- [75] I. Affleck, *Field Theory Methods and Quantum Critical Phenomena*, in *Fields, Strings and Critical Behavior*, Proc. Les Houches Summer School in Theoretical Physics (1988).
- [76] A. M. Tsvelik, *Quantum Field Theory in Condensed Matter Physics*, 2nd edition, Cambridge University Press (2003).
- [77] Al. B. Zamolodchikov, Int. J. Mod. Phys. A**10** 1125 (1995).
- [78] A. B. Zamolodchikov and Al. B. Zamolodchikov, Nucl. Phys. B **379** 602 (1992).
- [79] Al. B. Zamolodchikov, Nucl. Phys. B **342** 695 (1990).
- [80] A. B. Zamolodchikov and Al. B. Zamolodchikov, Ann. Phys. **120** 253 (1979);
R. J. Baxter, *Exactly Solved Models in Statistical Mechanics*, Academic Press London (1982).

- [81] A. B. Zamolodchikov and Al. B Zamolodchikov, Ann. Phys. **120** 253 (1979).
- [82] B. Berg, M. Karowski, P. Weisz and V. Kurak, Nucl. Phys. B **134** 253 (1979);
P. Wiegmann, Phys. Lett. B **142** 173 (1983).
- [83] J. L. Cardy, J. Phys. A. **19** L1093 (1986).
- [84] A. W. W. Ludwig and J. L. Cardy, Nucl. Phys. B **285** 687 (1987).
- [85] A. B. Zamolodchikov, JETP Lett. **43** 730 (1986).
- [86] G. M. T. Watts, Nucl. Phys. B **859**, 177 (2012); P. Giokas and G. M. T. Watts,
arXiv:1106.2448.
- [87] A.B. Zamolodchikov, Adv. Stud. Pure Math. **19**, 641 (1989).
- [88] G. Feverati, K. Graham, P. A. Pearce, G. Z. Toth and G. M. T. Watts, J. Stat.
Mech. **0911** 03011 (2008).
- [89] A. Klumper and D. C. Johnston Phys. Rev. Lett. **84**, 4701 (2000).
- [90] S. Lukyanov, Nucl. Phys. B **522**, 533 (1998).
- [91] M. Lüscher, Commun. Math. Phys. **104**, 177 (1986).
- [92] J. Cardy, private communication.
- [93] Vl. S. Dotsenko, Nucl. Phys. B **240** 687 (1989).
- [94] R. M. Konik and A. LeClair, Nucl. Phys. B **479** 619 (1996).
- [95] G. Mussardo, V. Riva, G. Sotkov, Nucl. Phys. B **670**, 464 (2003).
- [96] A.B. Zamolodchikov, Sov. J. Nucl. Phys. **44** (1986), 529.
- [97] R. Rajaraman, *Solitons and Instantons*, Elsevier, (1982).
- [98] G. Mussardo and G. Takacs, J.Phys. A **42** (2009) 304022.
- [99] M. Greiner, I. Bloch, O. Mandel, T. W. Hänsch, and T. Esslinger,
Phys. Rev. Lett. **87**, 160405 (2001).
- [100] M. Köhl, H. Moritz, T. Stöferle, K. Günter, and T. Esslinger, Phys. Rev. Lett. **94**,
080403 (2005).
- [101] I. Bloch, J. Dalibard, and W. Zwerger, Rev. Mod. Phys. **80**, 885 (2008).

- [102] A. Polkovnikov, K. Sengupta, A. Silva, and M. Vengalattore, *Rev. Mod. Phys.* **83**, 863 (2011).
- [103] J.-P. Brantut, J. Meineke, D. Stadler, S. Krinner, T. Esslinger, *Science* **337**, 1069 (2012)
- [104] D. Stadler, S. Krinner, J. Meineke, J.-P. Brantut, and T. Esslinger, *Nature (London)* **491**, 736 (2012)
- [105] M. A. Topinka, B. J. LeRoy, S. E. J. Shaw, E. J. Heller, R. M. Westervelt, K. D. Maranowski, A. C. Gossard, *Science* **289**, 2323 (2000).
- [106] E. Madelung, *Zeitschrift für Physik* **40**, 322 (1926).
- [107] M. Müller, J. Schmalian, and L. Fritz, *Phys. Rev. Lett.* **103**, 025301 (2009).
- [108] N. Bushong, Y. Pershin, and M. Di Ventra, *Phys. Rev. Lett.* **99**, 226802 (2007).
- [109] M. Dyakonov, and M. S. Shur, *Appl. Phys. Lett.* **87**, 111501 (2005).
- [110] M. Mendoza, H. J. Herrmann, and S. Succi, *Phys. Rev. Lett.* **106**, 156601 (2011).
- [111] T. Enss, R. Haussmann, and W. Zwerger, *Ann. Phys.* **326**, 770 (2011).
- [112] M. S. Paoletti and D. P. Lathrop, *Annu. Rev. Condens. Matter Phys.* **2**, 213 (2011).
- [113] M. Tsubota, *J. Phys.: Condens. Matter* **21**, 164207 (2009).
- [114] S. K. Nemirovskii, *Physics Reports* **524**, 85 (2013).
- [115] I. M. Khalatnikov, *An Introduction to the Theory of Superfluidity.*, New York, 1965.
- [116] L. P. Pitaevskii, *Sov. Phys. JETP* **13**, 451 (1961).
- [117] E. P. Gros, *J. Math. Phys.* **4**, 195 (1963).
- [118] V. Hunyadi, Z. Rácz, and L. Sasvári, *Phys. Rev. E* **69**, 066103 (2004).
- [119] E. Bettelheim, A. G. Abanov, and P. Wiegmann, *Phys. Rev. Lett.* **97**, 246402 (2006).
- [120] E. Bettelheim, and L. Glazman, *Phys. Rev. Lett.* **(109)**, 260602 (2012).
- [121] I. V. Protopopov, D. B. Gutman, P. Schmitteckert, and A. D. Mirlin, *Phys. Rev. B* **87**, 045112 (2013).
- [122] J. Friedel, *Philos. Mag.* **43**, 153 (1952).

- [123] M. Di Ventura, and T. N. Todorov, J. Phys. Cond. Matt. **16**, 8025 (2004).
- [124] C.-C. Chien, M. Zwolak, and M. Di Ventura, Phys. Rev. A **85**, 041601 (2012).
- [125] G. Benenti, G. Casati, T. Prosen, D. Rossini, and M. Žnidarič, Phys. Rev. B **80**, 035110 (2009).
- [126] G. Benenti, G. Casati, T. Prosen, and D. Rossini, EPL **85**, 37001 (2009).
- [127] T. Prosen and B. Žunkovič, New J. Phys. **12**, 025016 (2010).
- [128] D. Karevski and T. Platini, Phys. Rev. Lett. **102**, 207207 (2009).
- [129] B. Misra, and E. C. G. Sudarshan, J. Math. Phys. **18**, 756 (1977).
- [130] R. J. Cook, Phys. Scr. **T21**, 49 (1988).
- [131] W. M. Itano, D. J. Heinzen, J. J. Bollinger, and D. J. Wineland, Phys. Rev. A **41**, 2295 (1990).
- [132] T. Prosen, arXiv: 0704.2252 (2007).
- [133] E. Schöll, *Nonlinear Spatio-Temporal Dynamics and Chaos in Semiconductors* (Cambridge University Press, Cambridge 2011).
- [134] I. Affleck, and J. B. Marston, Phys. Rev. B **37**, 3774 (1988).
- [135] J. B. Marston, and I. Affleck, Phys. Rev. B **39**, 11538 (1989).
- [136] T. Esslinger, Private Communication.
- [137] A. G. Aronov, A. Yu. Zyuzin, and B. Z. Spivak, JETP. Lett. **43**, 555 (1986).